

# **dust formation in L dwarf atmospheres**

**diploma thesis**

**Sören Witte**

Universität Hamburg  
Departement Physik

14 February 2008



# Abstract

The topic of this thesis is the investigation of dust formation in ultra-cool stellar and brown dwarf atmospheres. The self-consistent dust model `DRIFT-PHOENIX` by Dehn (2007) was used for this purpose.

In order to improve the convergence behaviour of the models, several components of the code were modified or replaced. None of these upgrades affect the physics considered. Changes in the results are a mere numerical result. The modifications included an upgrade of the dust routine (Helling et al. (2008b)), an improvement of the effective medium calculations for the dust particles, a smoothing of the dust opacities and an improvement of the combined convergence of the hydrostatics and the dust routine.

The upgrades enhance the stability of the `DRIFT-PHOENIX` results. However, oscillations of the results remain an issue. The number density of dust particles in the resulting models is increased, compared to the models of Dehn (2007). This is due to the improved mechanism for the effective medium calculations.

With the new `DRIFT-PHOENIX` version, model sequences were computed for varied effective temperatures, surface gravities and metallicities. So far, the range between 1500 K and 2500 K and therefore the whole L spectral type is covered by `DRIFT-PHOENIX`. The models show an increase of the dust particle number density with decreasing effective temperature. The accompanying backwarming causes a decrease of the maximum mean grain size.

A fit with a spectrum of the brown dwarf DENIS J0205-1159 demonstrates that the synthetic spectra resemble the observations very well. The new models yield a slight improvement of the fit, compared to the results by Dehn (2007).

# Inhaltsangabe

Das Aufgabenstellung dieser Diplomarbeit ist die Untersuchung der Staubbildung in Atmosphären ultrakühler Sterne und brauner Zwerge. Dafür wurde das selbstkonsistente Staubmodell `DRIIFT-PHOENIX` von Dehn (2007) verwendet.

Um das Konvergenzverhalten der Modelle zu verbessern, wurden Teile des Codes modifiziert oder ersetzt. Keine dieser Verbesserungen wirkt sich auf die berücksichtigte Physik aus. Veränderungen in den Ergebnissen sind rein numerischen Ursprungs. Die Modifikationen beinhalten eine Aufrüstung der Staubroutine (Helling et al. (2008b)), eine Verbesserung der Berechnung des effektiven Mediums des Staubteilchen, eine Glättung der Staubopazitäten und eine Verbesserung der vereinten Konvergenz von Hydrostatik und der Staubroutine.

Die Aufrüstungen erhöhen die Stabilität der `DRIIFT-PHOENIX` Ergebnisse. Dennoch bleiben Oszillationen der Ergebnisse ein Problem. Die Anzahldichte der Staubteilchen ist in den resultierenden Modellen gegenüber den Modellen von Dehn (2007) erhöht. Dies liegt an dem verbesserten Mechanismus der Berechnungen des effektiven Mediums.

Mit der neuen `DRIIFT-PHOENIX` Version wurden Modellsequenzen für variierte Effektivtemperatur, Oberflächengravitation und Metallizität berechnet. Bisher wird der Bereich von 1500 K bis 2500 K und damit die gesamte Spektralklasse L durch `DRIIFT-PHOENIX` abgedeckt. Die Modelle weisen eine Erhöhung der Staubteilchenanzahldichte mit sinkender Effektivtemperatur auf. Der einhergehende Wärmestau bewirkt eine Verringerung der maximalen Staubteilchengröße.

Ein Vergleich mit dem dem Spektrum des braunen Zwerges DENIS J0205-1159 demonstriert, dass die synthetischen Spektren Beobachtungen gut reproduzieren. Die neuen Modelle bewirken eine leichte Verbesserung des Fits, verglichen mit den Ergebnissen von Dehn (2007).

# Contents

<b>Abstract</b>	<b>iii</b>
<b>1. Introduction</b>	<b>1</b>
<b>2. Theory</b>	<b>4</b>
2.1. Atmosphere model . . . . .	4
2.2. Dust model . . . . .	9
2.3. Dust opacity . . . . .	13
<b>3. Application</b>	<b>16</b>
3.1. static_weather . . . . .	16
3.2. DRIFT . . . . .	17
3.3. PHOENIX . . . . .	17
<b>4. Upgrades</b>	<b>19</b>
4.1. Dust model . . . . .	19
4.2. Refractive index calculations . . . . .	20
4.3. Dust opacity calculations . . . . .	22
4.4. Hydrostatics / DRIFT loop . . . . .	24
<b>5. Convergence behaviour</b>	<b>26</b>
<b>6. Model sequences</b>	<b>30</b>
6.1. General dust cloud structure . . . . .	32
6.2. Temperature sequence . . . . .	36
6.3. Gravity sequence . . . . .	47
6.4. Metallicity sequence . . . . .	56
6.5. Spectra . . . . .	67
6.6. Conclusions . . . . .	69
<b>7. Comparison with observations</b>	<b>71</b>
<b>8. Summary and outlook</b>	<b>73</b>
<b>A. Appendix: Kinetic model for dust formation</b>	<b>76</b>
<b>B. Appendix: Implementation</b>	<b>80</b>

*Contents*

---

<b>Index</b>	<b>88</b>
<b>Bibliography</b>	<b>89</b>

# 1. Introduction

In order to interpret observed spectra, stellar atmosphere models are required. As the variety of observed objects becomes wider, new effects need to be considered. This is the case for cool atmospheres, in which condensation has a huge influence on the spectra. In this work, the formation of dust clouds in L type objects is investigated. These objects comprise mostly brown dwarfs but also low-mass stars and hot Jovian planets. In the following, an introduction to brown dwarfs and their respective spectral types and a summary of dust models are given.

More comprehensive summaries concerning this topic are given in Allard et al. (1997), Basri (2000), Chabrier & Baraffe (2000), Chabrier et al. (2005) and Kirkpatrick (2005).

## History of brown dwarfs

Stars are formed in collapsing gas clouds. The released energy is dissipated by radiation. The contraction of the resulting protostar is stopped as soon as a stable fusion of hydrogen is initiated at the core of the gas cloud. However, this stable fusion requires a sufficient temperature and density. In order to reach them, the mass of the gas cloud must exceed a certain critical value, which is denoted as the hydrogen burning minimum mass ( $m_{\text{HBMM}} = 0.07 M_{\odot}$  (Chabrier et al. (2005))). Objects which fall short of this limit are denoted as substellar objects. Their contraction, which takes much longer due to their smaller gravity, is only stopped by degeneracy of the electron gas (e.g., Hayashi & Nakano (1963)). Thermal equilibrium is never reached for substellar objects. Up to the early 1960's the existence of substellar objects was denied by theoretical models, because the timescales for their formation which was approximated to a hundred billion years by far exceeded the assumed age of the universe. Hayashi (1962) pointed out that low-mass objects remained fully convective over most of their formation. Therefore, Kumar (1963a,b) was able to prove that objects of several percent of the solar mass could indeed form in less than a billion years. During the following decades, none of these objects could be observed, because of their extremely low luminosity. This low luminosity has led to the suspicion that substellar objects might be responsible for the large difference between the luminous mass and the gravitational mass of galaxies and galaxy clusters. However, this is likely not the case, as current world models require non-baryonic matter in order to explain the missing mass problem (e.g., Schneider (2006)).

Tarter (1975, 1976) coined the term "brown dwarf", which today is commonly used to refer to these substellar objects.

In 1988, a companion (GD 165B) of GD 165 was discovered by Becklin & Zuckerman (1988). GD 165B does not feature any methane or ammonia absorption, which is characteristic for Jovian planets like Jupiter. However, the TiO features are not nearly as strong as for a typical M dwarf, as condensation of metals and metal-oxides becomes important. Thus, GD 165B does not fit into the classical typification of stars, but its nature was not realised. In the following years, other objects of the like have been discovered.

The first definite discovery of a brown dwarf was done by Nakajima et al. (1995). Gl 229B has clear methane absorption features, which suggests an effective temperature of less than 1000 K. In

the same year the first extra-solar giant planet 51PegB was discovered by Mayor & Queloz (1995). Since the discovery of Gl 229B, several hundred objects with substellar masses have been identified, which was mostly due to surveys like, e.g., 2MASS. In order to classify the newly observed spectra, the two spectral types L and T were introduced (see, e.g., Basri (2000), Kirkpatrick (2005)). A description of these types follows in the next paragraph.

Free floating brown dwarfs of masses of only a few Jupiter masses have been observed in young stellar clusters (e.g., Béjar et al. (2001)), which suggests that these objects have been formed rather independently by the collapse of a gas cloud. This is a clear distinction from planets, which form within a protoplanetary disk around a parent star. Simulations by Whitworth & Stamatellos (2006) yielded a minimum required mass of 0.001 to  $0.004M_{\odot}$  for collapsing gas clouds. Hence, there is indeed an overlap between planetary and brown dwarf masses. An indicator for the discrimination between a Jovian planet and a brown dwarf accompanying a larger star is the abundance of heavy elements, which is enhanced in protoplanetary disk and, therefore, also in planets (Chabrier et al. (2005)).

### **Spectral types L and T**

Stellar spectra are classified by their characteristic features. Each spectral type can be identified with a certain range of the effective temperature. The spectral type which was long related to the lowest observed effective temperatures and, therefore, the lowest mass dwarf stars is denoted as M. M dwarfs feature strong absorption by metal oxides like TiO and VO. In order to include the newly discovered ultracool objects in the classification, two additional spectral types were introduced.

According to recent models, L type objects range from effective temperatures of approximately 2500 K to 1300 K, while the T type objects range from 1500 K to 750 K. The overlap is not a theoretical uncertainty but is related to the variety of objects, which is available for these effective temperatures. As was mentioned before, the contraction of brown dwarfs is only stopped by electron gas degeneracy. Until this is reached, the object is still contracting. The contraction yields an increase of the surface gravity for young brown dwarfs (Kirkpatrick (2005)). This strongly affects the atmosphere structure and the chemical equilibrium. Hence, the spectral features of methane do not become observable below a single critical value of the effective temperature, but depend on the surface gravity as well.

The upper boundary of the L type corresponds to a theoretical mass of 0.085 solar masses for old main sequence stars. This means early L types are comprised of old low mass stars and young brown dwarfs. Their spectra show strong absorption lines of neutral alkalis, metal oxides and hydrides, as well as other molecular bands like, e.g., H<sub>2</sub>O and CO. Below effective temperatures of about 2000 K the TiO, VO, FeH and CaH bands disappear (Chabrier & Baraffe (2000)), because of increasing efficiency of condensation. As was mentioned earlier, at lower effective temperatures CH<sub>4</sub> forms at the expense of CO (Allard & Hauschildt (1995)). In even cooler objects this is accompanied by NH<sub>3</sub>. Absorption by these molecules is a characteristic of T type spectra (Burgasser et al. (2002)). The theoretical lower limit of the T type of 750K simply represents the coolest brown dwarfs which have been observed so far. The T spectral type is comprised of old, high-mass brown dwarfs, brown dwarfs of low masses and young, high mass Jovian planets.

### **Dust models for brown dwarf atmospheres**

For effective temperatures below 2800 K complex O-rich compounds condense (Chabrier &

---

Baraffe (2000)). Thus, the gas phase is depleted of elements. The forming dust cloud represents a strong, mostly grey opacity, i.e. lower atmosphere layers are blanked out, and causes a backwarming.

Synthetic spectra, therefore, require a proper treatment of the dust formation, in order to reproduce the observed spectra. A host of dust simulations have been made by a number of groups. An example are the `COND` and `DUSTY` models by Allard et al. (2001). Their basic assumption is the phase equilibrium of the condensing species. Either the opacity of all the forming dust particles is considered (`DUSTY`) or it is totally neglected and the dust particles are assumed to have settled gravitationally (`COND`). However this can only be seen as extreme limiting cases.

A summary of different dust models is given in Dehn (2007). A comparison of these models will be given in Helling et al. (2008a).

Most models do not account for the dynamic formation and settling of dust particles and the convective overshoot properly. Helling et al. (2008b) developed a model (`DRIFT`) which solves the nucleation, growth and evaporation of dust particles in the non-phase equilibrium, with respect to gravitational settling and element replenishment by convective overshoot. Dehn (2007) incorporated this model in the general-purpose stellar atmosphere code `PHOENIX` (Hauschildt & Baron (2007)). This thesis is a continuation of that work. An exploration of the parameter space was done, in order to investigate the influence on the dust cloud.

## Outline

A summary of the theoretical background of this work is given in Chap. 2. This is followed by a short description of the employed code in Chap. 3. Chaps. 4 and 5 delineate identified issues, which hamper the convergence of the coupled dust and atmosphere models, and describe successful methods to avoid them in the first place. The resulting models, produced with the upgraded code, and the respective spectra are analyzed in Chap. 6. A fit of an observation with the synthetic spectra in Chap. 7 and a summary in Chap. 8 complete this work.

## 2. Theory

In this chapter the theoretical background of this work is given. The atmosphere model is introduced with emphasis on the radiative and convective energy transfer, followed by a description of the dust model and the dust opacity calculations.

### 2.1. Atmosphere model

This section is a brief introduction to the stellar atmosphere model, calculated by the general-purpose stellar atmosphere code PHOENIX. The descriptions in this section follow Rutten (2003), Mihalas (1970, 1978) and Unsöld (1955).

**Model assumptions:** If the velocity distribution of all particles, their excitation and ionization distribution and the radiation field within a volume element of the atmosphere can be identified with a single temperature, the volume element is in thermodynamic equilibrium. The single temperature is a result of the strongly coupled scattering, absorption and emission / ionization processes of all the different particles and the radiation field. Otherwise the result would be a superposition of distributions for different temperatures. Because of the structure of stellar atmospheres, thermal equilibrium is only possible for small volume elements, leading to the denotation of local thermodynamic equilibrium (LTE). For a larger temperature gradient the volume elements, in which LTE is a valid assumption, become smaller. The size of the volume elements has to be compared with the mean free path. The mean free path is defined as the mean distance between the interactions of a considered particle with other particles. If this mean free path for any given particle or photon is of the order of the diameter of the volume cells, the different cells will show coupled velocity, excitation or ionization distributions and the LTE inside the volume elements is disrupted. Low interaction probabilities and the respective large mean free path, which leads to non-LTE, are a result of locally low density of interacting particles in an appropriate state or of a saturation of these states.

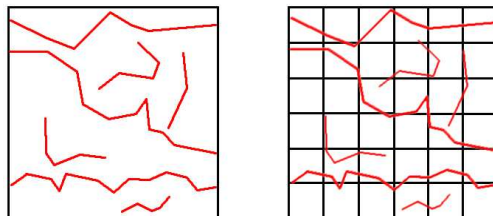


**Figure 2.1.:** LTE (left): Many interactions per particle/photon take place in every volume cell. NLTE (right): Only few interactions take place due to fragmentation into smaller cells or large free paths.

The high gravity in brown dwarf atmospheres results in a high density and pressure. In addition, the low temperature of brown dwarf atmospheres is the cause for lower excitation and ionization rates. Thus, both of these quantities lead to short mean free paths. Hence, the coupling between adjacent volume elements is negligible at the atmospheric region, where most of the observed flux originates. Therefore, LTE is a justifiable simplification for brown dwarfs.

Plane-parallel symmetry is assumed for the atmosphere model for consistency with the dust model. It is a valid assumption, because the atmosphere is very thin compared to the total radius of the brown dwarf. Furthermore it is appropriate to consider the problem as independent from the azimuthal angle of the line of sight. This is due to the fact, that the small scale structures in stellar atmospheres can neither be resolved by observations nor simulated in conjunction with radiative transfer in a satisfying quality at present. Thus, the distribution of these structures is assumed to be homogeneous. The result is a one-dimensionally structured atmosphere. The independent variable is the altitude  $z$ . In addition the polar angle between  $z$  and the line of sight has to be considered. Another important demand on the model is the steady state. This results in hydrostatic, radiative and chemical equilibrium and the conservation of energy, elements and charge on the large scale. The influence of the radiation and the convective motion on the pressure is low and thus is disregarded in Bernoulli's equation, resulting in:

$$\frac{dp}{dz} = -\rho g, \quad (2.1)$$

with the gas pressure  $p$ , the altitude  $z$ , the gas density  $\rho$  and the gravitational acceleration  $g$ . The radiative equilibrium means that the total flux of energy is conserved throughout the atmosphere. Any sources or sinks of the flux would result in a time-dependency of the local temperatures. The concentration of elements and molecules is constant, due to the chemical equilibrium.

**Important quantities:** The abundances of the elements determine the chemical composition of atmospheres and thereby their thermodynamic properties and the radiation field. In order to simplify matters, all elements within the designated model atmospheres, except for hydrogen and helium, are assumed to have a fixed abundance ratio, compared to the sun. By this means, all abundances relative to hydrogen ( $M/H$ ) are determined by the solar abundances relative to hydrogen ( $M_{\odot}/H_{\odot}$ ) and a single parameter, which is called metallicity  $[M/H]$ :

$$[M/H] = \log \frac{M/H}{M_{\odot}/H_{\odot}} \quad (2.2)$$

The radiation field is described by the intensity  $I_{\lambda}$ . It is a function of the wavelength interval  $d\lambda$  at a position  $\vec{r}$  and is defined by the amount of energy  $dE$  passing through an area  $dA$ , normal to the beam direction  $\vec{n}$ , into a solid angle  $d\omega$  and per time interval  $dt$ :

$$dE = I_{\lambda}(\vec{r}, \vec{n}, t) dA \cos \theta d\lambda d\omega dt. \quad (2.3)$$

The angle between  $\vec{n}$  and the direction of solid angle  $d\omega$  is denoted as  $\theta$ .

Since only the plane-parallel homogeneous time-independent case is of interest here,  $I_{\lambda}$  rather depends on the altitude  $z$  than on the actual location, azimuthal direction and time. For simplification the polar angle is expressed by  $\mu = \cos \theta$ . The intensity averaged over all solid angles is called the mean intensity  $J_{\lambda}(z)$ :

$$J_{\lambda}(z) = \frac{1}{2} \int_{-1}^1 I_{\lambda}(z, \mu) d\mu. \quad (2.4)$$

In order to keep track of direction and strength of energy flows, the flux vector  $F_\nu$  is defined. For the abovementioned case follows

$$F_\nu = 2\pi \int_{-1}^1 I_\lambda(z, \mu) \mu d\mu. \quad (2.5)$$

The statistical population of all atomic, ionic and molecular states is determined by the radiation field. In general the rate equations for all possible transitions would have to be satisfied. Assuming local thermodynamic equilibrium this is reduced to Saha-Boltzmann statistics (see e.g. Rutten (2003)). After a distance  $ds$  the whole spectrum, i.e. the flux as a function of the wavelength, may be redistributed by emission, absorption and scattering, depending on the population of all states. The respective coefficients are  $\eta_\lambda$  (emission),  $\kappa_\lambda$  (absorption) and  $\sigma_\lambda$  (scattering):

$$dI_\lambda = (\eta_\lambda - (\kappa_\lambda + \sigma_\lambda)I_\lambda)ds. \quad (2.6)$$

The coefficient for absorption and scattering, which describe the microphysical processes, are usually abbreviated by the macrophysical extinction coefficient  $\chi_\lambda = \kappa_\lambda + \sigma_\lambda$ , which is also called opacity.

The opacity integrated over distance is introduced as the optical depth  $\tau$ . It is used to define a depth scale of the atmosphere:

$$d\tau_\lambda = -\chi_\lambda dz. \quad (2.7)$$

The source function is defined as auxiliary quantity:

$$S_\lambda = \frac{\eta_\lambda}{\chi_\lambda}. \quad (2.8)$$

Considering thermal emission and isotropic, coherent scattering in thermodynamic equilibrium this results in

$$\begin{aligned} S_\lambda &= \frac{\kappa_\lambda}{\kappa_\lambda + \sigma_\lambda} B_\lambda(T) + \frac{\sigma_\lambda}{\kappa_\lambda + \sigma_\lambda} J_\lambda \\ &= (1 - \epsilon_\lambda) B_\lambda(T) + \epsilon_\lambda J_\lambda, \end{aligned} \quad (2.9)$$

(e.g. Mihalas (1970)), where  $B_\lambda(T)$  is the Planck function and  $\epsilon_\lambda = \frac{\sigma_\lambda}{\kappa_\lambda + \sigma_\lambda}$  the probability of the photon absorption.

**Radiative energy transfer:** Adapting Eq. 2.6 for the plane-parallel case ( $dz = \mu ds$ ), transforming it to the optical depth  $d\tau_\lambda$ , including the source function and dropping the index  $\lambda$  for clarity, results in the radiative transfer equation:

$$\mu \frac{dI}{d\tau} = I - S. \quad (2.10)$$

It has to be solved for any wavelength and location in order to produce a spectrum. Formal solution of Eq. 2.10 leads to the Schwarzschild equation:

$$J(\tau) = \frac{1}{2} \int_0^\infty S(t) E_1(|t - \tau|) dt = \Lambda S(\tau), \quad (2.11)$$

with  $E_n(x) = \int_1^\infty \frac{e^{-xt}}{t^n} dt$ . The operator  $\Lambda$  for an arbitrary function  $f$  is given by:  $\Lambda f = \frac{1}{2} \int_0^\infty f(t) E_1(|t - \tau|) dt$ . As can be seen from Eq. 2.9, the source function depends on the radiation field and the temperature, which itself depends on the radiation field. Thus, an analytical solution of Eq. 2.11 is already impossible for simple model assumptions.

Simple numerical approaches, like  $J_{n+1} = \Lambda S_n$ , do not lead to satisfying results, because the required number of iterations to reach an acceptable measure of convergence is of order  $\frac{1}{\epsilon_\lambda}$ . Cannon (1973) proposed a method that accelerates the convergence. Therefore the  $\Lambda$ -operator is split into

$$\Lambda = \Lambda^* + (\Lambda - \Lambda^*). \quad (2.12)$$

The approximate Lambda operator is denoted by  $\Lambda^*$ . It is used to define a new ansatz:

$$J_n = \Lambda^* S_n + (\Lambda - \Lambda^*) S_{n-1}. \quad (2.13)$$

The increased calculation time per iteration step, due to the approximate operator, is outweighed by the improved convergence behaviour. The determination of an appropriate  $\Lambda^*$  can be found, e.g., in Hauschildt & Baron (1999).

**Convective energy transfer:** In brown dwarfs, the convection zone reaches into the lower atmosphere. This means, a large amount of the energy is transported by large scale mass motions instead of radiation.

It is important to know under which conditions an atmospheric region will show convective motion. This can be approximated as follows. A mass element moves slightly upwards. Its movement is assumed to be adiabatic<sup>1</sup>. The element remains in hydrostatic equilibrium with its environment, which in turn leads to an increase in volume, caused by the decline of the pressure in the surrounding environment. Thus, the density of the mass element is reduced. The density of the environment does also show a decrease with altitude. If the density of the mass element is lower than the density of the environment this causes a buoyant force. In contrast, a higher density forces the mass

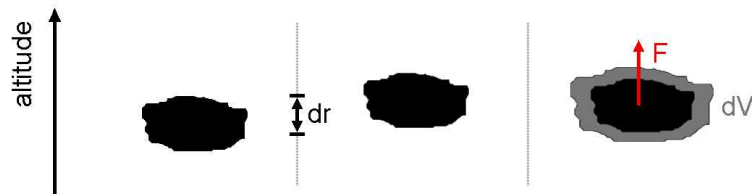


**Figure 2.2.:** The adiabatic expansion of a slightly shifted mass element results in a buoyant force.

element back to its original position. Thus, an initially fully radiative atmospheric region will start to feature convective motions as soon as the adiabatic density gradient of a mass element ( $A$ ) is smaller<sup>2</sup> than the density gradient of the radiative environment ( $R$ ):

$$\left( \frac{d\rho}{dr} \right)_R > \left( \frac{d\rho}{dr} \right)_A. \quad (2.14)$$

<sup>1</sup>The considered mass elements do not exchange any thermal energy with their environment.

<sup>2</sup>The density decreases with altitude and thus the gradients are negative.

Under the additional assumption of an ideal gas of temperature  $T$  and pressure  $p$ , Eq. 2.14 can be transformed into the Schwarzschild criterion:

$$\left(\frac{d \ln T}{d \ln p}\right)_R > \left(\frac{d \ln T}{d \ln p}\right)_A, \quad (2.15)$$

which is usually abbreviated by  $\nabla_R > \nabla_A$ .

Up to now the whole mechanism of convection is still not well understood, because the underlying hydrodynamics turn out to be extremely complex. At the moment convection can be approached by the rather phenomenological mixing length theory (Prandtl (1925), Biermann (1932)).

Hot adiabatic mass elements from lower layers rise and dissipate thermal energy by mixing with higher layers. The mass exchange between layers is compensated by cool sinking mass elements, which absorb thermal energy. The distance, after which the mass elements dissolve and dissipate or absorb their respective excess or lack of energy, is called mixing length  $l$ . The temperature gradient of the elements is denoted by  $\nabla_E$ , while the gradient of the mean surroundings is  $\nabla$ .

The kinetic energy of a mean mass element can be estimated from the the buoyant force. If half the energy gained from buoyancy is lost to friction, the mean velocity  $v_{\text{conv}}$  is given by

$$v_{\text{conv}} = \frac{1}{2} \sqrt{\frac{g H_p Q}{2}} (\nabla - \nabla_E)^{1/2} \frac{l}{H_p}, \quad (2.16)$$

where  $g$  is the local gravitational acceleration. The pressure scale height  $H_p$  and the parameter  $Q$  are defined by

$$\frac{1}{H_p} = -\frac{d \ln p}{dr} = \frac{g \rho}{p} \quad \text{and} \quad Q = 1 - \left(\frac{\partial \ln \mu}{\partial \ln T}\right)_p.$$

For a distance  $dr$  which has been crossed by a mass element, the temperature difference  $dT$  between the surroundings can be estimated from the temperature gradients. Hence, a mean flux of energy, carried by the mass elements of the mean convective velocity  $v_{\text{conv}}$ , can be calculated:

$$F_{\text{conv}} = \frac{1}{4} \sqrt{\frac{g H_p Q}{2}} (\rho c_p T) (\nabla - \nabla_E)^{3/2} \left(\frac{l}{H_p}\right)^2. \quad (2.17)$$

## 2.2. Dust model

This section is an introduction of the applied dust model, called `static_weather`. The detailed development of the model can be found in Woitke & Helling (2003, 2004), Helling & Woitke (2006) and Helling et al. (2008b). It is based on the idea of using dust moments (Gail et al. (1984), Gail & Sedlmayr (1988)). The following descriptions are primarily based on these sources, as well as Dehn (2007). A more detailed description of the solution of the dust formation problem is given in Appendix A.

**Subsonic free molecular flow:** The characteristics of a flow around a dust particle depends on size and shape of the particle, its relative velocity  $v_{\text{rel}}$  to the surrounding gas as well as the gas pressure and the gas viscosity. Accordingly, it is crucial to choose the appropriate description. For scale independent comparisons of flows a set of dimensionless numbers is applied. The Reynolds number depends on particle shape, relative velocity and viscosity and is a characteristic for the damping of turbulent flows, while the Knudsen number  $K$  represents the mean free path in particle radii.

Most dust particles remain small compared to the mean free path ( $K \gg 1$ ) (Woitke & Helling (2003)). Only at deeper layers, where the gas density is high and the grain radii are large, this assumption may not be valid (Woitke & Helling (2004)). If the backwarming<sup>3</sup> by the dust cloud is considered, the resulting dust grains are much smaller. Thus,  $K \gg 1$  is valid for most of the dust cloud layers.

The relative velocity between particle and gas remains below sonic speed<sup>4</sup> ( $v_{\text{rel}} \ll v_s$ ). This is assumed to be valid for the whole atmosphere. Thus, all equations following in this section and Appendix A are valid for this case, the so-called subsonic free molecular flow.

A more detailed examination of flows around dust particles can be found in Woitke & Helling (2003).

**Dust composition:** The formation of carbon monoxide (CO) binds two of the most important reactants for other elements<sup>5</sup>. The ratio of the abundances of both atomic species decides whether carbon- or oxygen-rich molecules dominate the atmosphere of brown dwarfs. The applied dust model describes dust formation in an oxygen-rich atmospheres as the here considered 32 dust growth reactions mostly include molecules that contain oxygen. These molecules consist of 5 elements and lead to dirty dust grains of 7 different species. In this context dirty means a mixed composition of the particles. A full list of the considered dust growth reactions can be found in Dehn (2007).

**Growth mechanism:** A large fraction of materials condensing within the considered temperature range do not feature stable monomers in the gas phase (e.g.,  $\text{Mg}_2\text{SiO}_4$ ). In general, a simple chemical absorption of a dust species from the surrounding gas is not possible. Another possibility

<sup>3</sup>The dust particles absorb photons from the radiation field. This is balanced by the isotropic emission in the infrared. Thus, a fraction of the outwards directed flux is suppressed, until the surrounding gas has reached a temperature at which the flux is conserved again. (Helling (2007))

<sup>4</sup>The sonic speed for an ideal gas of the mean molecular mass  $\bar{\mu}$  in thermodynamic equilibrium is given by  $v_s = \sqrt{\kappa k T / \bar{\mu}}$ , with the adiabatic exponent  $\kappa$ , the Boltzmann constant  $k$  and the local temperature  $T$ .

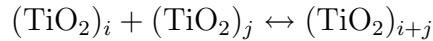
<sup>5</sup>In high-density environments, methane ( $\text{CH}_4$ ) may replace CO as the key molecule (Helling (2007)).

for condensation is a multi-body reaction. Since that requires several molecules at the same location at the same time, this is very unlikely for reactants in the gas phase. However these molecules can be absorbed physically by an existing surface. Thermal excitation enables the reactants to leap randomly from one lattice points at the surface to the next. This is stopped by the chemical reaction leading to the actual dust species. Either the related educts merge as soon as they occupy adjacent lattice points, forming a new island<sup>6</sup> of the related species themselves, or they stick to an already existing island.

This kind of reaction is called a surface reaction (Helling & Woitke (2006)). The resulting reaction rate is increased strongly, compared to the ordinary multiple body gas phase reaction.

For every surface reaction the molecule of the lowest physical absorption rate can be identified. It is referred to as key species. The timescales of physical absorption are considered to be much larger than the timescales for transport of reactants to an appropriate island and the resulting chemical reaction. Thus the physical absorption rate of the key educts for the associated growth reactions is a good approximation for the growth rate of a certain dust species.

**Formation of seed particles:** For an efficient growth of the dust particles, a condensation seed is required because it provides a surface on which other materials are able to condense. The process of seed formation is referred to as nucleation. In the model applied here,  $\text{TiO}_2$  was chosen as seed material, due to its high thermodynamic stability and high concentration within the gas phase. Because  $\text{TiO}_2$  is already present in the gas phase, condensation seeds form through simple polymerization without the need for a preexisting surface or multi-body reactions:



The indices  $i$  and  $j$  represent the respective numbers of monomers of which the reacting polymers consists. In addition the various possible isomers of the molecule  $(\text{TiO}_2)_{i+j}$  must be considered. Each of these reactions takes place in both directions at different timescales. As a result from the timescales of all possible reactions, a favoured reaction path can be determined. Along this path instabilities of reactants or low reaction rates cause delays in the growth of the polymer. The 'narrowest' point along the reaction path is called the bottleneck reaction. The related reacting particle is called the critical cluster.

For further considerations it is important to specify the nucleation ratio  $J^*$ , which describes the number of seed particles forming per time interval. In this model the final seed particles have an arbitrary size of 1000 monomers (Woitke & Helling (2004)).

As simplification, it is assumed that all reactions which lead to the bottleneck reaction are in chemical equilibrium. The bottleneck reaction and subsequent reactions have a higher growth reaction rate compared to the evaporation rate. Hence, the growth towards the dust seed is favoured. The critical cluster is thus the molecule with the lowest concentration. Its evaporation rate is considered to be negligible. This way the seed formation ratio  $J$  is approximated by the concentration of the critical cluster  $n^*$  divided by the timescale of its growth  $\tau_{N^*}^{\text{growth}}$ :

$$J^* = \frac{n^*}{\tau_{N^*}^{\text{growth}}} \quad (2.18)$$

For a detailed description of  $n^*$  and  $\tau_{N^*}^{\text{growth}}$  see Gail et al. (1984).

---

<sup>6</sup>Each solid species has an individual lattice. Therefore, the species prefer to cluster homogenously. These clusters are denoted as islands.

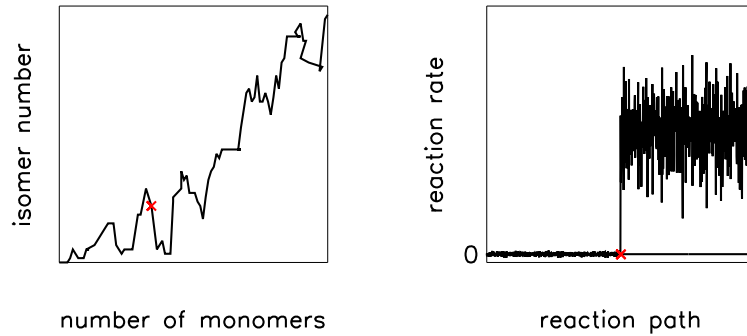


**Figure 2.3.:** The left panel shows an example of a favoured reaction path, with the red  $\times$  representing the critical cluster. The right panel shows a sketch of the effective growth reaction rate along the reaction path, with  $\times$  representing the bottleneck reaction.

If in contrast the local conditions lead to evaporation of the dust, the reversed nucleation process depends on the size distribution of the seeds, which is not well known. A simple approximation regarding the critical cluster underestimates the influence of this distribution. As stated in Woitke & Helling (2004), the evaporation of dust takes place in a very thin layer of the atmosphere. Thus resulting errors, caused by the lack of a known size distribution, are considered to be small.

**Growth of the dust grains:** After seeds have formed via nucleation, other materials may grow on top of the so far pure  $\text{TiO}_2$ -clusters.

Depending on the circumstances the composition of the layers of the dust grains can vary. Fortunately, this needs not to be considered for evaporation processes, which only take place at the grain surface. As it was stated in Helling & Woitke (2006), it can be assumed that all solid island are equally distributed. This is due to diffusion processes caused by heating of the grains. The total fraction of the grain surface of the dust species is comparable to their total volume fraction.

The growth of materials on dust seeds and their respective evaporation leads to changes in the volume of the dust grain. The temporal evolution of the grain volume is described by (Woitke & Helling (2003)):

$$\frac{dV}{dt} = 4\pi a^2 \sum_r \Delta V_r n_r v_r^{\text{rel}} \alpha_r \left(1 - \frac{1}{S_r}\right). \quad (2.19)$$

These temporal changes in volume are proportional to the surface area of spherical particles of radius  $a$ . The summation considers the already mentioned 32 surface reactions  $r$  of the dust model. In Eq. (2.19) the particle volume difference per surface reaction<sup>7</sup>  $\Delta V_r$ , the concentration of the reactants  $n_r$ , the Maxwell-distributed relative velocity  $v_r^{\text{rel}}$  for the dust particles and the gas, the sticking coefficient  $\alpha_r$  and the supersaturation ratio  $S_r$  are included. The sticking coefficient denotes the probability that a collision of the grain and a gas molecule leads to a surface reaction. The supersaturation ratio is the ratio of the local vapour pressure to the saturation vapour pressure of the considered reactants. In Eq. (2.19),  $S_r$  regulates the number of surface reactions and serves as switch between growth and evaporation, depending on its sign. Accordingly, growth and evaporation of all considered species is already included. Differences in temperature between dust

<sup>7</sup>The quantity  $\Delta V_r$  represents the volume, which is added to or removed from the total dust grain volume by a single surface reaction  $r$ .

and gas do not need to be taken into account, because for typical pressure and temperature ranges the difference  $\Delta T_{\text{max}} \approx 3.5\text{K}$  (Woitke & Helling (2003)) is small. Another possibility for grain growth would be the coagulation of grains. It is not included into the model because it takes place at much larger timescales (Cooper et al. (2003)).

**Gravitational settling:** Dust particles are influenced by gravity, radiation and collisions with the surrounding gas particles. Compared to the influence of gravity the influence of radiation is negligible in the brown dwarfs. Thus, only friction is counteracting the gravity. The friction force strongly depends on the flow characteristics of the dust particles. For a subsonic free molecular flow it is

$$F_{\text{fric}}(a, \rho, T, v_{\text{drift}}) = \frac{8\sqrt{\pi}}{3} a^2 \rho c_T v_{\text{drift}}, \quad (2.20)$$

with  $a$  representing the grain radius,  $v_s$  the sonic speed and  $v_{\text{drift}}$  the fall velocity of the grain.  $c_T = \sqrt{2kT/\bar{\mu}}$  is the mean thermal velocity for a gas of mean molecular mass  $\bar{\mu}$ . The drift velocity is derived from the resulting equation of motion:

$$v_{\text{drift}} = \frac{\sqrt{\pi}}{2} \frac{\rho_d g}{\rho c_T} a, \quad (2.21)$$

where  $\rho$  is the gas density,  $\rho_d$  the dust grain density, i.e., the density of the dust species weighted by their volume fraction and the gravitational acceleration  $g$ .

Note that the drift velocity has a narrowing influence on the grain size distribution. Large grains have a high drift velocity and thus cross a certain layer of the atmosphere very fast, resulting in a smaller growth. In contrast, small grains settle much slower and thus can pick up much more material for growth within the same layer.

**Convective overshoot:** The abundances of the elements in the gas phase, which contribute to the dust formation, decrease with every nucleation and growth process. To some extent this depletion is balanced by replenishment through convective overshooting, resulting in a quasi-static abundance distribution throughout the atmosphere.

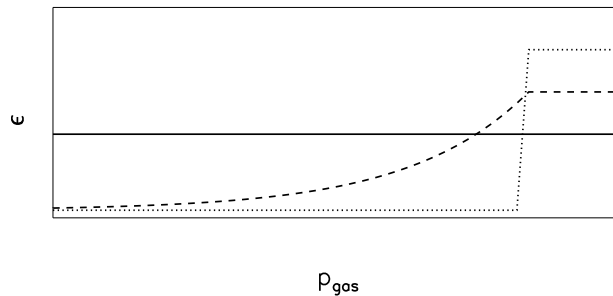


**Figure 2.4.:** The element abundance throughout a stellar atmosphere without dust is assumed to be constant (solid line). Dust formation depletes the higher atmosphere, while the dust settling enriches the lower atmosphere (dotted). The overshoot replenishes the higher layers (dashed).

Convective motions do not cease instantly at the edge between convective and radiative zone. Rather the momentum of the upward moving mass elements is dispersed in higher layers. As

convection is still not fully understood, the influence of the overshoot needs to be approximated. Following the suggestion by Ludwig et al. (2002), Woitke & Helling (2004) adopted an exponential increase of the mixing time scale  $\tau_{mix}(z)$  with the height above the convection zone edge:

$$\log \tau_{mix} = \log \tau_{mix}^{\min} + \beta \cdot \max \left( 0, \log \frac{p_0}{p(z)} \right). \quad (2.22)$$

The gradient of the time scale  $\beta$  is the ratio of the mass exchange frequency increment and the pressure increment and has the approximate value  $\beta = 2.2$ . In Eq. 2.22,  $\tau_{mix}^{\min}$  is the minimum mixing time scale and  $p_0$  the pressure at the edge of the convection zone. The minimum mixing time scale is approximated by  $\tau_{mix}^{\min} = \frac{l}{H_P v_{conv}}$ , with the mixing length parameter  $l = 2$ .

## 2.3. Dust opacity

Dust also has a direct influence on the radiative transfer, aside from element consumption and redistribution. The opacities of dust particles are determined by their composition and size distribution.

**Effective medium theory:** In order to calculate the opacities of dust grains, their refractory indices must be known. The considered particles consist of up to seven different materials. Hence, an effective refractive index has to be determined.

Maxwell's equations for uncharged conductive media can formally be brought to the form of a homogenous wave equation, by the introduction of a complex dielectric function  $\epsilon = \epsilon_r + i\epsilon_i = \epsilon_r + i \frac{\sigma \lambda}{2\pi \epsilon_r c}$ , with  $c$  being the speed of light,  $\sigma$  the electric charge per area perpendicular to the electromagnetic field and  $\epsilon_r$  the ordinary dielectric coefficient (see e.g. Nolting (2004)). As the refractive index  $n$  is defined by  $n = \sqrt{\epsilon_r \mu}$ , with the magnetic permeability  $\mu$ , this leads to a complex refractive index  $m = n + ik = \sqrt{\epsilon \mu}$ . The imaginary part  $k$  describes the dampening of electromagnetic waves in conductive media. The conversion for a non-magnetic medium ( $\mu = 1$ ) is given by

$$\epsilon_r = n^2 - k^2 \quad \epsilon_i = 2nk \quad (2.23)$$

and

$$n = \sqrt{\frac{1}{2} \left( \epsilon_r + \sqrt{\epsilon_r^2 + \epsilon_i^2} \right)} \quad k = \sqrt{\frac{1}{2} \left( -\epsilon_r + \sqrt{\epsilon_r^2 + \epsilon_i^2} \right)}. \quad (2.24)$$

The dielectric function of the effective medium  $\bar{\epsilon}$ , consisting of  $j$  different species, satisfies the following equation (e.g. Aspnes et al. (1979)):

$$\frac{\bar{\epsilon} - \epsilon_h}{\bar{\epsilon} + \gamma \epsilon_h} = \sum_s \frac{V_s}{V_{tot}} \frac{\epsilon_s - \epsilon_h}{\epsilon_s + \gamma \epsilon_h}. \quad (2.25)$$

The dielectric function of the host medium is denoted by  $\epsilon_h$ . The volume fraction within an average grain  $\frac{V_s}{V_{tot}}$  and the dielectric function  $\epsilon_s$  are known properties of the considered constituents of the dust grain. Finally, the screening parameter  $\gamma$  describes the influence of the particle shape on the depolarization<sup>8</sup>. In the case of spherical particles, it has a value of  $\gamma = 2$ .

<sup>8</sup>Electromagnetic fields lead to reallocation of electrons within conductive media. This reallocation results in a counteracting field. A larger value of  $\gamma$  yields a stronger counteracting field and thus a larger value for  $\bar{\epsilon}$ .

The dust grains are assumed to be well-mixed, which means a homogeneous distribution of solid islands. This results in a single refractive index for the whole grain. Additionally, no single species can be assumed to dominate the compound. Otherwise the effective medium for a mixture of dust species of equal volume fractions would be biased. Thus, the only reasonable solution is to adopt the effective medium as host medium itself (Bruggeman (1935)):

$$\sum_s \frac{V_s}{V_{\text{tot}}} \frac{\epsilon_s - \bar{\epsilon}}{\epsilon_s + 2\bar{\epsilon}} = 0. \quad (2.26)$$

The effective dielectric function is determined by the root of Eq. 2.26.

In the following an algorithm for finding  $\bar{\epsilon}$ , developed by Bosch et al. (2000), is summarized. Instead of using  $\epsilon$ , the problem is expressed in form of the refractive index by substituting  $\epsilon = m^2$ . Thus the use of Eqs. 2.23 and 2.24 can be avoided. This is of advantage because these transformations can lead to two distinct solutions. Furthermore, it is only required to find the root for the absolute value of Eq. 2.26, which leads to:

$$\left| \sum_s \frac{V_s}{V_{\text{tot}}} \frac{m_s^2 - \bar{m}^2}{m_s^2 + 2\bar{m}^2} \right| = 0, \quad (2.27)$$

with the effective refractive index  $\bar{m}$ . Demands on the solution are  $n, k, \epsilon_i > 0$ . This is already sufficient for identification of the physically correct root, as long as the initial guess for the solving algorithm is good enough (Bosch et al. (2000)).

**Mie theory:** Now that the effective refractory indices of the dust grains are known, it is possible to calculate the dust opacities. To do so Maxwell's equations must be solved for the scattering of radiation by dust grains of arbitrary size. Again, the grains are assumed to be spherical. The solution of this problem is called Mie theory. Discussion of its derivation and application can be found in Mie (1908), Wiscombe (1980, 1996) and Wolf & Voshchinnikov (2004).

For a given grain size  $a$  and a wavelength  $\lambda$ , a size parameter  $x = 2\pi a/\lambda$  is defined. The scattered electromagnetic field components are calculated from amplitude functions, which are infinite sums of angular functions multiplied by the Mie coefficients  $a_n$  and  $b_n$ :

$$a_n = \frac{\psi'_n(mx)\psi_n(x) - m\psi_n(mx)\psi'_n(x)}{\psi'_n(mx)\zeta_n(x) - m\psi_n(mx)\zeta'_n(x)} \quad (2.28)$$

$$b_n = \frac{m\psi'_n(mx)\psi_n(x) - \psi_n(mx)\psi'_n(x)}{m\psi'_n(mx)\zeta_n(x) - \psi_n(mx)\zeta'_n(x)}. \quad (2.29)$$

The complex refractive index  $m$  has been obtained by the effective medium theory. The  $\psi_n$  and  $\zeta_n$  are called Riccati-Bessel functions and are defined by

$$\psi_n(x) = xJ_n(x) \quad \text{and} \quad \zeta_n(x) = \psi_n(x)ixY_n(x), \quad (2.30)$$

where  $J_n(x)$  and  $Y_n(x)$  are the spherical Bessel functions of the first and second kind, respectively. From the amplitude functions, the efficiencies for extinction  $Q_{\text{ext}}$ , scattering  $Q_{\text{sca}}$  and absorption

$Q_{\text{abs}}$  can be determined (van de Hulst (1957), Debye (1909)):

$$Q_{\text{ext}} = \frac{2}{x^2} \sum_{n=1}^{\infty} (2n+1) \text{Re}(a_n + b_n) \quad (2.31)$$

$$Q_{\text{sca}} = \frac{2}{x^2} \sum_{n=1}^{\infty} (2n+1) (|a_n|^2 + |b_n|^2) \quad (2.32)$$

$$Q_{\text{abs}} = Q_{\text{ext}} - Q_{\text{sca}}. \quad (2.33)$$

These efficiencies can easily be transformed into effective cross sections  $C_{\text{sca}}$  for scattering processes and  $C_{\text{abs}}$  for absorption processes, by multiplying with the geometrical cross section of the particle:  $C_{\text{sca}} = \pi a^2 Q_{\text{sca}}$  and  $C_{\text{abs}} = \pi a^2 Q_{\text{abs}}$ . Finally, the dust opacity can be determined for a number density of dust particles  $n_d$ :

$$\chi = \kappa + \sigma = n_d (C_{\text{abs}} + C_{\text{sca}}). \quad (2.34)$$

### 3. Application

The simulation of brown dwarf and giant planet atmospheres is done by the stellar atmosphere code PHOENIX. It is supplemented by the DRIFT module by Dehn (2007), which includes the dust simulation routine `static_weather`. Hereafter the combined codes are addressed by DRIFT-PHOENIX. The applied PHOENIX configuration follows the model descriptions of Sec. 2.1, while `static_weather` and DRIFT follow Secs. 2.2 and 2.3, respectively. A short illustration of a single run for each of the three component is given in the following.

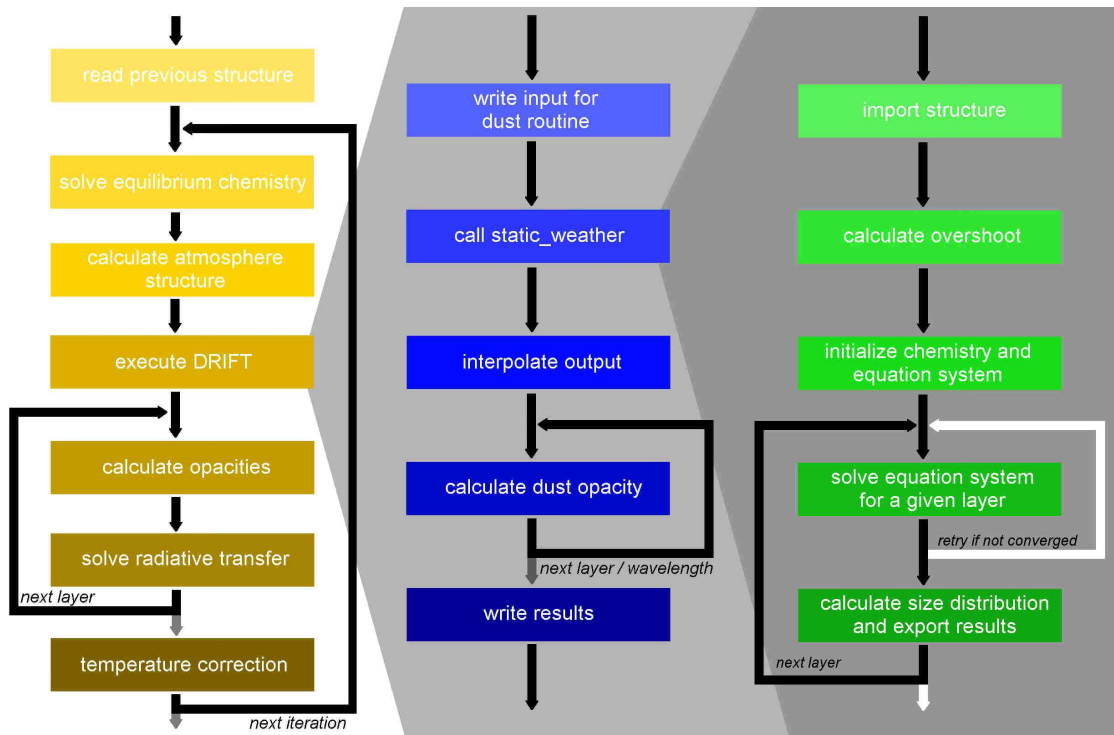


Figure 3.1.: flow charts: left: PHOENIX; center: DRIFT; right: `static_weather`

#### 3.1. `static_weather`

`static_weather` is a code for calculation of quasi-static dust layers in cool stars and giant planets. Its development can be found in Woitke & Helling (2003, 2004), Helling & Woitke (2006) and Helling et al. (2008b).

After reading the atmosphere structure, provided by PHOENIX, `static_weather` calculates the mixing time scale  $\tau_{\text{mix}}(z)$  for every layer. Then the equilibrium chemistry is initialized, which

input parameters	most important output parameters
gas temperature $T(z)$	reshuffled element abundance $\epsilon_i(z)$
gas pressure $p(z)$	grain size distribution $a_1(z), N_1(z), a_2(z), N_2(z)$
gas density $\rho(z)$	volume fractions $\frac{V_s}{V_{\text{tot}}}$ of solid $s$
convection velocity $v_{\text{conv}}(z)$	nucleation rate $J^*(z)$
gravitational acceleration $g(z)$	growth rate $\chi_{\text{net}}(z)$
absolute element abundance $\epsilon_i^0$	supersaturation ratio $S_r(z)$ for reaction $r$
mean molecular mass $\mu(z)$	
overshoot parameter $\beta$	

**Table 3.1.:** `static_weather` input and output parameters

means the abundance of molecules, which contribute to the dust growth, is calculated by a Newton-Raphson algorithm. After all necessary data has been gathered the solver determines a solution for the system of dust moment and element conservation equations for the outermost layer. This solution is taken as starting value for the solution of the next lower layer, for which the local conditions are interpolated from the PHOENIX-input. If the solver is unable to find a solution, `static_weather` returns to the last layer, reduces the stepsize between layers and retries a solution. The loop is terminated as soon as the dust vanishes in a low layer.

A more detailed chart and description of this routine follows in the next section.

## 3.2. DRIFT

The data exchange between PHOENIX and `static_weather` is done via the DRIFT module by Dehn (2007).

In fact, two subroutines of the module need to be executed before the actual run of DRIFT. This is because of the element depletion by the dust formation. Therefore, the atmosphere structure can not simply be calculated from the prescribed element abundances, but the layer-dependent abundances resulting from a previous `static_weather`-run must be employed.

When the atmosphere structure has been calculated DRIFT is run. First it prepares an input file for `static_weather` and then executes the dust routine. After this was done, DRIFT reads the output and interpolates it for the PHOENIX depth grid. From the volume fraction and refractive index lists for pure condensates an effective refractive index is calculated per layer. From these and the respective grain size distribution, the effective opacity is calculated for all wavelengths and layers. This is written as output and included in the radiative transfer calculations in PHOENIX.

## 3.3. PHOENIX

PHOENIX is an ever-growing code for simulation of stellar and planetary atmospheres. It is capable of calculating self-consistent atmosphere models for objects throughout the Hertzsprung-Russelldiagram. Applications range from extrasolar giant planets to supernovae. Therefore, a host of effects and approaches is interlaced in the code. However, most effects do not have to be considered in general, but are only included for special cases. Thus for every kind of model a certain configuration is applied. In the following a brief description of the PHOENIX configuration for the designated models of dwarfs and giant planets with dust is given.

### 3. Application

---

Typically, a PHOENIX run starts with importing of a previous model at similar stellar parameters. In addition the layer-dependent abundances, as mentioned in Sec. 3.2, are required. From this input the equilibrium chemistry is calculated with respect to element and charge conservation. For the resulting atmosphere composition a new atmosphere structure is computed by the solution of the hydrostatic equation and inclusion of energy transport by convection. In the next step, the DRIFT module is run in order to obtain the dust properties and the element depletion and to calculate the dust opacities. Afterwards all other opacities are calculated and the radiative transfer problem is solved with operator splitting (Sec. 2.1). In order to fulfill energy conservation a temperature correction is done. The applied Unsöld-Lucy method can be found in, e.g., Hauschildt et al. (2003). The resulting model is then iterated until a specified number of loops is passed or the temperature corrections for all layers fall below a specified value.

A more general introduction to the PHOENIX code can be found in Hauschildt & Baron (2007). Applications and details about individual aspects can be found in various publications. Allard & Hauschildt (1995), Allard et al. (2001), Baron et al. (2003), Ferguson et al. (2005), Hauschildt (1992), Hauschildt et al. (1997) and Hauschildt & Baron (1999, 2006) are mentioned to name just a few.

## 4. Upgrades

The incorporation of the dust model into the atmosphere model was done by Dehn (2007). Independently, both models converge very well. Coupled to each other, the convergence of the models proved to be difficult, most of which is due to the highly sensitive coupling of their physical and chemical processes. For example, large temperature corrections due to flux errors and uncertainties in the determination of the convection zone edge result in a strong feedback on the dust complex, which in turn has a big influence on the radiative transfer.

A too strong correction of any quantity yields strong corrections of other quantities in the next iteration. Those quantities feed back on the first one. Thus, the original correction is compensated for, besides a margin which corresponds to the convergence of the model. If the original correction and its compensation are much larger than the margin, a stable revolving pattern over the iterations establishes. This is denoted as oscillation. In order to break oscillations, the feedback by any of the involved quantities on the others must be dampened. One such example is the dampening of the temperature correction, which was the usual method used by Dehn (2007), for models which did not converge to a stable solution.

This section is about upgrades of the code, which were done in order to improve its stability and convergence behaviour. The details of the implementation are summarized in Appendix B.

### 4.1. Dust model

The original dust routine (version 4), included into the stellar atmosphere code, frequently suffered from convergence problems in the element conservation. To address this problem the dust routine was upgraded to version 6.

**Comparison:** The abundances of the considered elements are determined by the element consumption equations for the stationary case. The root of this equation system is approximated by a modified Newton-Raphson iteration method. The method was improved and streamlined between the versions. For details see Appendix B.

In the new version, after a Newton-Raphson step has been determined, it is checked, whether this step improves the quality<sup>1</sup> of the approximation. If this is the case, the step is accepted and a new step is determined. If the step does not improve the quality, the stepsize is reduced until an improvement emerges, before a new step is determined.

The new `static_weather` version has an increased tolerance for the differential equation solver, speeding up the calculations, however, by sacrificing quality.

**Results:** Even for atmosphere models, which have converged, the original code, in combination with a low dampening of the temperature correction, was prone to convergence problems after

---

<sup>1</sup>The error caused by the inaccurately determined abundances is denoted as quality.

several iterations. The improved mechanism of the element conservation is able to determine the element abundances, where the old method did not. Only under rare conditions the new version fails, but even this can usually be circumvented by reducing the model parameter stepsize from the initial model, in order to avoid too extreme corrections of the atmosphere structure in the first iterations. Thus, the cause for program aborts in the element conservation of the dust routine has been effectively cleared. In addition, the total average computing time for a single run of `static_weather` has been reduced to almost 1/6, which reduces the `DRIIFT-PHOENIX` computing time for a model, considering 50000 wavelength points, by 5%.

The implemented physics have neither been changed nor expanded. Thus, the results of both versions resemble each other. The differences in the results, caused by the altered numerics and the increased solver tolerances, are negligible.

### 4.2. Refractive index calculations

A potential source of error in the calculation of the refractive index of the dust particles by the effective medium theory is that Eq. 2.26 has multiple solutions. The physically valid one has to be found. Not every initial guess for a numerical solution method yields the correct solution. Thus, in case that a determined solution turns out to be unphysical, another initial guess must be tried. In order to approach this, an improved algorithm was included.

**Comparison:** The effective medium algorithm by Dehn (2007) calculates the effective refractive index from the dielectric function. The root of Eq. 2.26 is determined by Müller's method. The three needed initial values are the volume fraction-weighted mean of the refractive indices of all considered dust species and the refractive indices of the species of the two largest volume fractions. The routine does not check for validity of the determined root and does not try other initial values. The new method follows the algorithm recommended by Bosch et al. (2000). It refrains from conversions to the dielectric function. The root is determined by a Newton-Raphson iteration. Similar to the method from the previous section, the size of the Newton-Raphson steps is reduced until the quality of the approximated refractive index improves. In addition the physical validity of the determined root is verified. The initial value for the iteration is the volume fraction-weighted mean of the refractive indices of all considered species. If no physical solution is found, the refractive index for the volume fraction-weighted mean dielectric functions of all considered dust species and the different refractive indices for the pure dust species are tried as initial values.

**Results:** An example for solutions determined by the two different solution methods is shown in Figs. 4.1 and 4.2. Both results were calculated for an arbitrarily chosen mixture<sup>2</sup> of dust species. In order to prove that the results of both methods differ from the volume fraction-weighted mean of the refractive indices of the pure species, the weighted mean is also shown in the figure.

Both methods produce identical results up to  $4.8\mu\text{m}$ . At  $4.8\mu\text{m}$  the refractive index, determined with the old algorithm, features a discontinuity. This is especially severe for the imaginary component, which increases by almost two orders of magnitude. After the discontinuity, the solutions by the different methods are completely different. The reason for the discontinuous results of the old method are likely the different solutions of Eq. 2.26. Beyond  $4.8\mu\text{m}$  the results for the old method

---

<sup>2</sup>2.5% TiO<sub>2</sub>, 41.5% Mg<sub>2</sub>SiO<sub>4</sub>, 10.9% MgFeSiO<sub>4</sub>, 42.5% Al<sub>2</sub>O<sub>3</sub>, 0.1% SiO<sub>2</sub> and 2.5% Fe

converge to a different solution, which is not the physically correct one. The peaks at  $52.7\mu\text{m}$  are likely another unphysical solution, which appears only once.

While the refractive index, determined by the new method, increases only slightly beyond  $35\mu\text{m}$ , the results for the old method show a strong increase with wavelength. The curve of the older routine is much closer to the simple volume fraction-weighted mean. Though the stellar flux at higher wavelengths is relatively small, the influence of the difference between both algorithms on the spectral appearance can not be neglected.

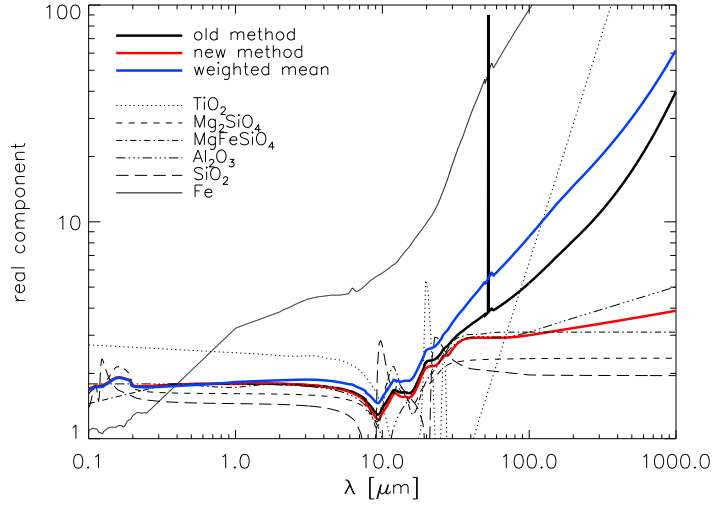


**Figure 4.1.:** Real component of the refractory indices for the differently determined effective media. The volume fraction-weighted mean and the pure media are shown for comparison.

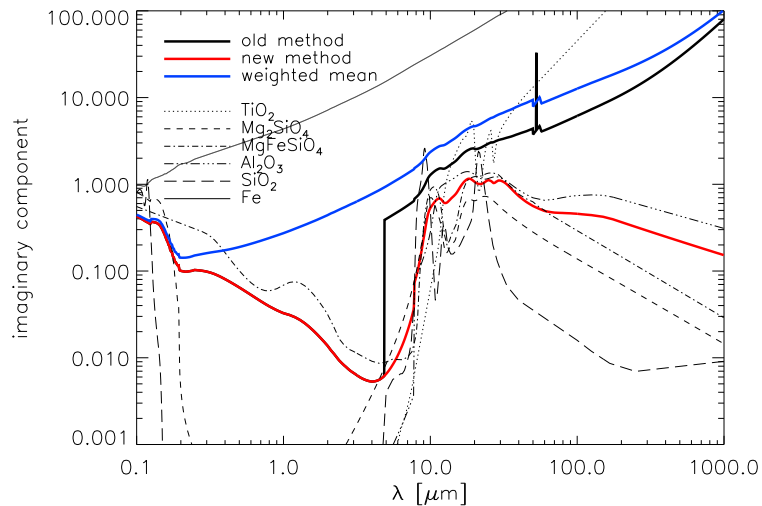


**Figure 4.2.:** Imaginary component of the refractory indices for the differently determined effective media.

As this example proves, it is essential to verify the validity of a found solution for the effective medium.

Though the Newton-Raphson method of the new routine requires fewer iterations to reach an acceptable degree of convergence, each of these iteration takes much longer. Due to this, the new method slightly increases the runtime of `DRIIFT-PHOENIX`, e.g. 2 – 3% for a model with 50000 wavelength points. An example for the deviation<sup>3</sup> between the spectra, resulting from the two different methods, is shown in Fig.4.3. The maximum change of the flux is about several percent for the given model parameters. Note that a variation of these parameters is able produce models with a stronger difference between the effective media, which will also cause higher flux deviations.

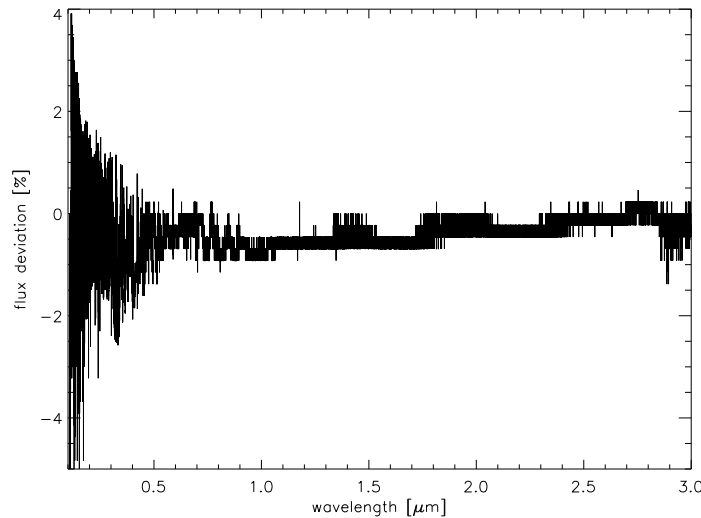


**Figure 4.3.:** Example for the deviation between two converged models ( $T_{\text{eff}} = 2000K$ ,  $\log(g) = 5.0$ ,  $[M/H] = 0.0$ ) for the new and old algorithm.

### 4.3. Dust opacity calculations

The results of the Mie calculation feature peak-like variations in the dust opacities with the grain size and the wavelength, which is shown in Fig.4.4. For a continuous grain size distribution the influence of these peaks would be insignificant, due to the integration over opacities of the whole distribution. The grain size distribution is not a direct result of the dust moment equations, but has to be approximated. The approximated distribution contains only two sample grain sizes per atmosphere layer. Those sizes shift slightly, even for a converged atmosphere model. Due to the opacity peaks, a slight shift of these sample sizes can already result in a strongly altered dust opacity. Observed differences between peaks and the local mean opacity are about 30%. This destabilizes the model by inducing disproportionate temperature corrections at the end of the iteration, which in turn changes the atmosphere structure and by this the size distribution of the

<sup>3</sup>Throughout this work, the relative change of flux between models is calculated by  $\Delta F = 2 \cdot 100\% \frac{F_{i-1} - F_i}{F_{i-1} + F_i}$ , where  $F_i$  is the flux array of iteration  $i$ .

dust<sup>4</sup>. In the worst case, this results in strong oscillations. Thus, the model could be unable to converge.

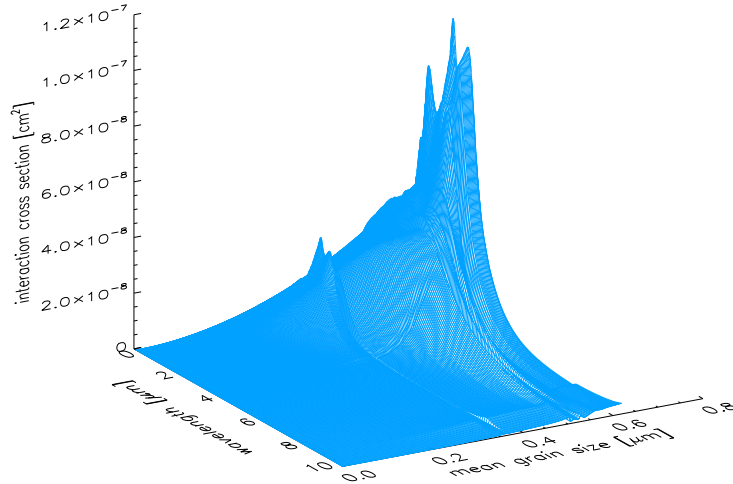


**Figure 4.4.:** The interaction cross section of each particle as a function of the wavelength and the dust grain size is shown for an example atmosphere model ( $T_{\text{eff}} = 2000K$ ,  $\log(g) = 5.0$ ,  $[M/H] = 0.0$ ) without smoothing of the Mie results.

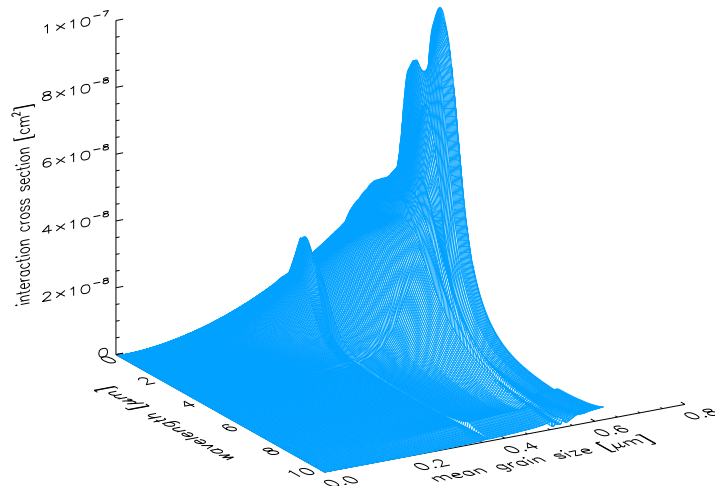


**Figure 4.5.:** Interaction cross section for similar model parameters as in Fig.4.4 but with smoothed Mie results.

<sup>4</sup>The use of a continuous grain size distribution function could avoid this problem, because the opacity peaks would balance each other.

Close to the edge of evaporation, the sample dust grain sizes and the respective dust particle number densities are highest. Coupled with the highest interaction cross section, i.e. the absorption and the scattering cross sections, for large dust grains, this region dominates the total dust opacity. A large temperature correction at the evaporation edge, due to peaks in the dust opacity, is able to cause a shift of the edge itself, which destabilizes the model even further, with local temperature corrections of the order of 100K as a consequence.

**Upgrade:** In order to stabilize the Mie results, they need to be smoothed. Instead of carrying out the Mie calculations only once for a given grain size, this is done for a set of 11 logarithmically equidistant adjacent grain sizes per input size. The resulting opacities are averaged. By this, the opacity changes between iterations, caused by variations of the grain size, are smoothed, which reduces subsequent changes of other quantities and improves the convergence behaviour (see Fig. 4.5).

**Results:** The DRIFT-PHOENIX runtime is slightly increased by the smoothing of Mie results. For a model with 50000 wavelength points the average increase is 1%. An example for the deviation between spectra of models with and without the smoothing is shown in Fig. 4.6.

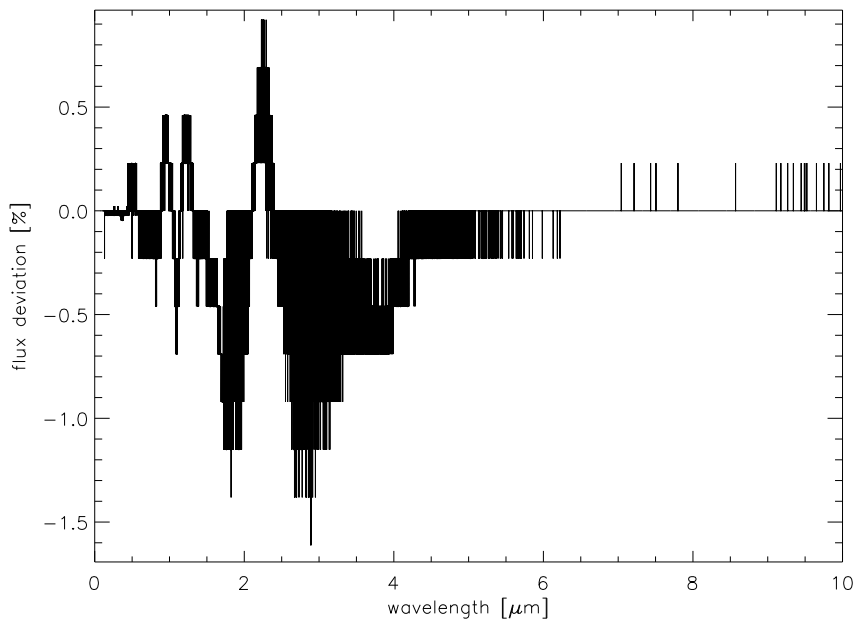


**Figure 4.6.:** Comparison of the flux of models ( $T_{\text{eff}} = 2000K$ ,  $\log(g) = 5.0$ ,  $[M/H] = 0.0$ ) with and without MieApprox.

#### 4.4. Hydrostatics / DRIFT loop

In the original DRIFT-PHOENIX version, the radiative transfer is calculated after DRIFT, which itself is executed after the solving the hydrostatic equilibrium. As already mentioned in Sec. 3.2,

the layer-dependent element abundances of a previous `static_weather` run are needed to calculate the atmosphere structure. This way, the radiative transfer of any iteration considers the dust opacities of the same iteration, but is calculated for an atmosphere structure that considers abundances, which have been altered by `static_weather` in the previous iteration. Thus, the atmosphere structure is 'outdated' and should actually be recalculated. The following temperature correction is biased.

Any shift in the temperature changes the dust properties and the corresponding opacities. A possible result is an oscillation of the atmosphere and dust properties over the iterations. Thus, the variation of any of these quantities is too large, the model is unable to converge.

**Upgrade:** In order to circumvent this problem, an additional loop was included into the code. The idea behind it is to reach a convergence between the hydrostatics and the dust formation, before solving the radiative transfer equation. By this means, the radiative transfer is provided with an atmosphere structure and a dust cloud structure, which originate from the same iteration. The possible bias of the subsequent temperature correction is eliminated.

Though a model might converge without the loop as well, the loop guides the model towards a stable solution.

**Results:** Each additional passage of the loop costs 2 – 3% additional calculation time. As it can be seen from Fig. 4.7, the use of two loop passes per iteration has a perceptible influence on the spectrum. The difference between the spectra for two and five passes per iteration is almost negligible. Thus, the default number of loop passes per iteration was set to two, as a compromise between calculation time and quality.

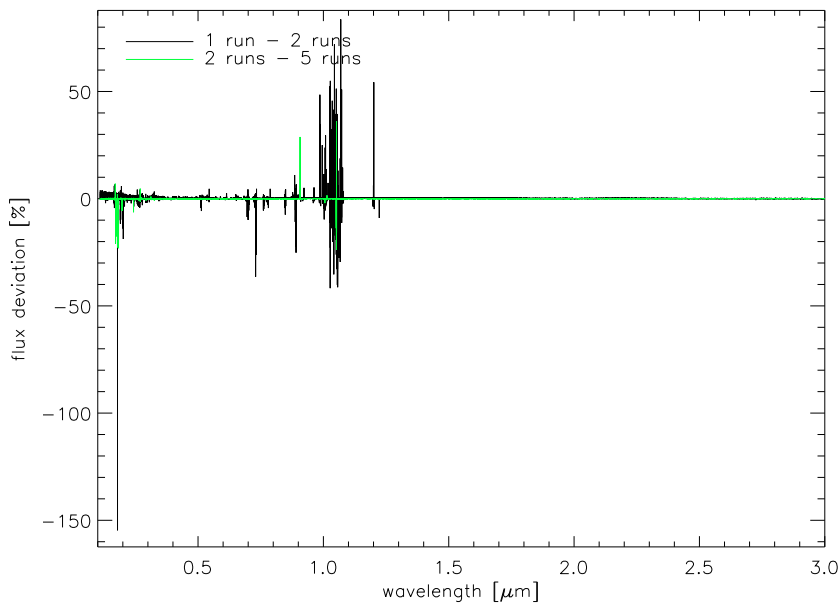


**Figure 4.7.:** Comparison of the flux of models ( $T_{\text{eff}} = 1900K$ ,  $\log(g) = 5.0$ ,  $[M/H] = 0.0$ ) for multiple loop passes.

## 5. Convergence behaviour

Even though the upgrades, described in the previous chapter, improve the convergence behaviour, most models without a dampened temperature correction still feature oscillating properties. In Fig. 5.1 a simple example for oscillations is given. Depicted are relative flux changes between consecutive iterations of a model run. In order to show a very simple oscillation pattern, the dust opacity has been neglected for this model. Thus, the only feedback on the atmosphere by the dust formation is the element depletion. Otherwise the result would be a superposition of oscillations, which is much harder to distinguish from a model, which does not show any evidence for convergence. From Fig. 5.1 it can be seen, that there is a pattern over three iterations. In the first one, the flux in the optical is increased. This is followed by an almost similar decrease in the next iteration. In the third iteration the flux increases only slightly. Two cycles are depicted.

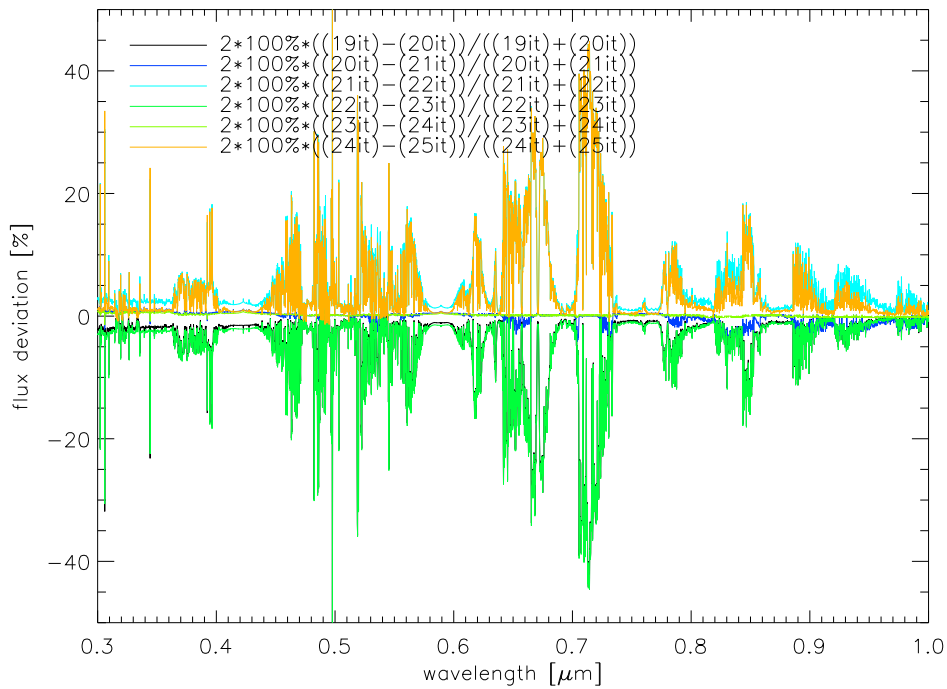


**Figure 5.1.:** Comparison of the flux of consecutive iterations of an example model ( $T_{\text{eff}} = 2000\text{K}$ ,  $\log(g) = 5.0$ ,  $[M/H] = 0.0$ ) without any dampening of the temperature correction.

**Convergence criterion and results:** Due to the improvements in the stability and convergence of DRIFT-PHOENIX, the criterion for convergence, set by Dehn (2007), can be handled more stringently. Only those models, which show a stable atmosphere structure, with temperature corrections below 1.0K and flux errors below 2.5%, and a stable dust grain size distribution, are fully

converged (Figs. 5.2 and 5.3). If this criterion is not met, the model is either not yet converged or the convergence is stalled by oscillations (Figs. 5.4 and 5.5). These two possibilities can be distinguished by the presence or absence of a periodic pattern of the atmosphere and dust quantities over the iterations. Stable amplitudes of an oscillation pattern can already be regarded as an indicator for convergence of the model. In addition to fully converged models, oscillating atmosphere models can reach a first degree of convergence, though they do not reach a steady state.

The commonly observed maximum temperature corrections<sup>1</sup> of 'converged' oscillating models are about 5 to 40K and approximately revolve every 6 to 10 iterations. The maximum temperature correction is usually related to the layers with the maximum grain size and dust number density. Though all other layers are also influenced by the oscillations, the usual temperature shift is below 2 to 10K.

With regard to the fact that `static_weather4` was much more susceptible to convergence failure, due to extreme atmosphere structures, oscillations in DRIFT-PHOENIX could be identified as the predominant cause for those failures.

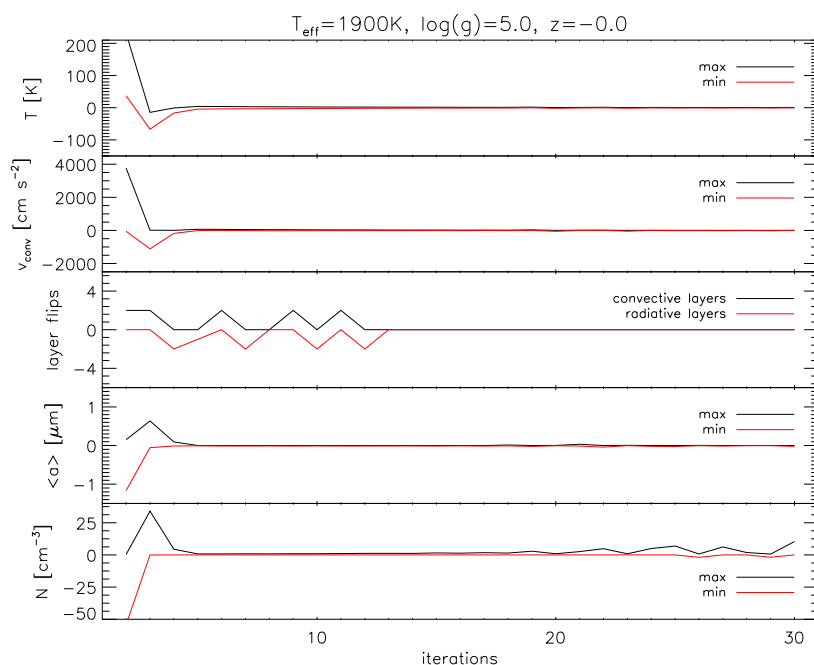


**Figure 5.2.:** Example for the convergence behaviour of a fully converging model ( $T_{\text{eff}} = 1900\text{K}$ ,  $\log(g) = 5.0$ ,  $[M/H] = 0.0$ ). Depicted are the maximum / minimum corrections of the temperature, convection velocity, mean dust grain size and dust number density between consecutive iterations. In addition, the number of layers, flipping from convective to fully radiative energy transfer and vice versa are shown.

`static_weather6` provides a much better stability, which enables the calculation of converged models or at least converged oscillating models, even though extreme atmosphere structures appeared in a previous iteration. For most model parameter combinations the dampening of the temperature correction works fine, in order to break oscillations.

<sup>1</sup>The temperature correction was dampened by a factor of 4 or 8

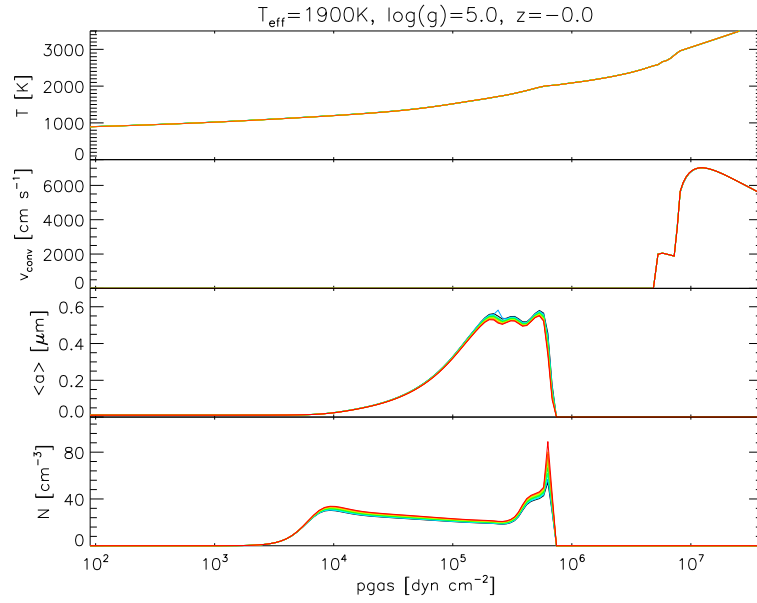


**Figure 5.3.:** Atmosphere structure and dust properties for the last 10 iterations of the model depicted in Fig. 5.2. All quantities are almost steady.

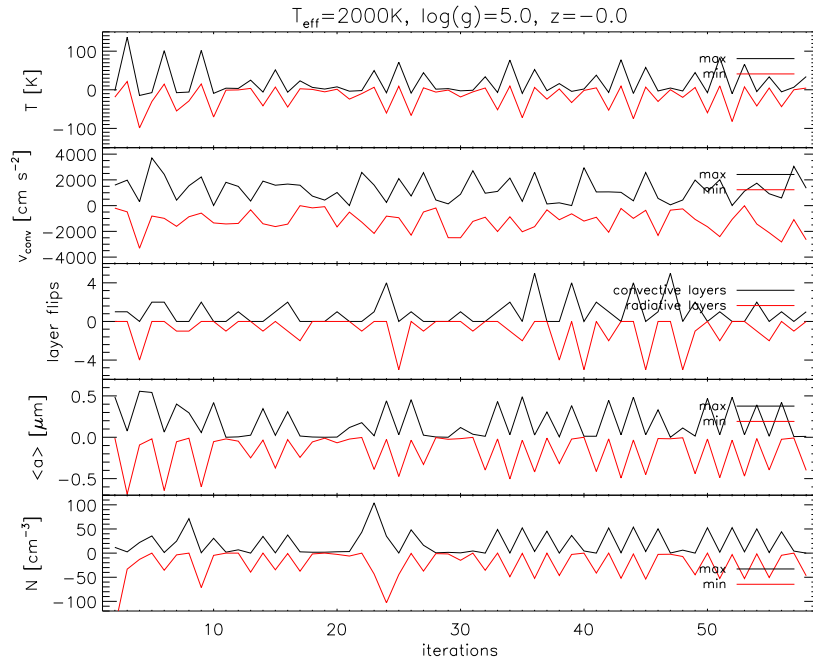


**Figure 5.4.:** Comparison of the flux of consecutive iterations of an example model ( $T_{\text{eff}} = 2000\text{K}$ ,  $\log(g) = 5.0$ ,  $[M/H] = 0.0$ ) without any dampening of the temperature correction.

**Influence of convection:** The convection velocity was identified as an important origin of oscillations. The convection zone has no sharp upper boundary in the model atmospheres. In fact, several layers are at the edge of fulfilling the Schwarzschild criterion (Eq. 2.15). A slight shift of the hy-

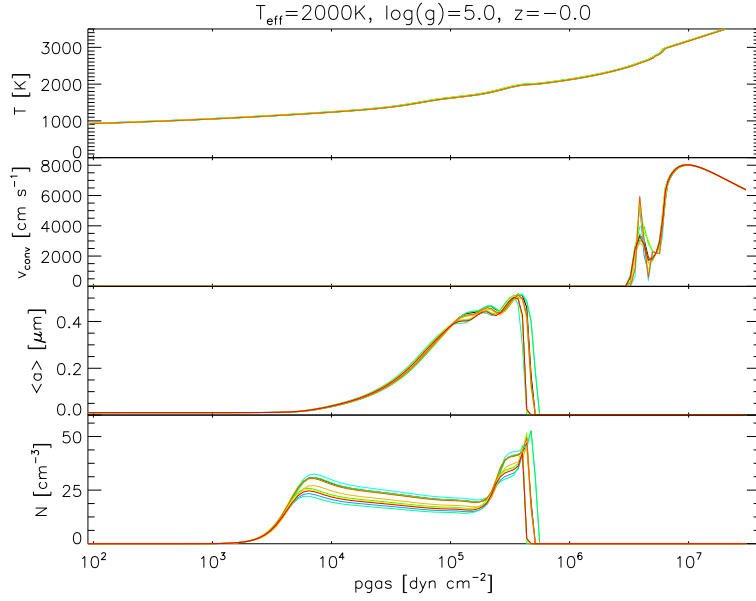


**Figure 5.5.:** Atmosphere structure and dust properties for the last 10 iterations of the model depicted in Fig. 5.4.

drostatic properties of a layer can thus enable or disable the convective energy transport (hereafter layer flip). Due to the conservation of the total flux, this leads to a temperature correction. The convection velocity of the outer convective layers is used to calculate the element replenishment of all higher layers. Hence, a layer flip above the original convection zone edge or a large increase of the convection velocity of a previously convective layer results in an accelerated replenishment, which has a huge influence on the number density and size of the dust particles. Especially an increased number density affects the radiative transfer and leads to large temperature correction. Again, this correction feeds back on the convection and the dust grain size distribution. Occurrence of a layer flips in those models, which are almost converged, is especially severe, because they cause large changes of the atmosphere and dust quantities. It usually takes several iterations to compensate for this. Before convergence is finally reached, another layer flips will likely appear.

## 6. Model sequences

The upgraded DRIFT-PHOENIX version was used to calculate one model sequence each for varied effective temperatures, varied surface gravities and varied metallicities. In this chapter the influence of these stellar parameters on the dust formation and its feedback on the atmosphere structure is investigated. It is recommended to review Sec. 2.2 and Appendix A in order to follow the descriptions of this chapter.

Whenever is spoken about supersaturation ratios of the dust species in this chapter, this relates to their effective supersaturation ratios  $S_{\text{eff}}$  (Helling et al. (2008b)). Most dust species do not possess stable monomers in the gas phase and would, thus, not be supersaturated. The effective supersaturation ratios represent the total effective values for the supersaturation ratios of the key reactant of each of the considered surface reactions  $S_r$  for each dust species.

Because there are so many dust and atmosphere properties which have to be considered at the same time, it is hardly possible to describe each independently. Therefore, their description is split into subsections, which address characteristic ranges of the growth of the dust particles. The atmosphere is divided into following parts (top to bottom, see Fig. 6.1):

1. Seed dominated region: weak formation of dust seeds, no perceptible dust growth, *upper boundary criterion*:  $\min(p_{\text{gas}}(J^* \neq 0))$
2. First growth region: increasing nucleation, perceptible grain growth, *upper boundary criterion*:  $\min\left(p_{\text{gas}}\left(\frac{d\log\langle a \rangle}{d\log p_{\text{gas}}} > 0.05 \log\langle a \rangle\right)\right)$
3. Fine particle region: increasing dust particle number density constant mean dust grain radius, *upper boundary criterion*:  $\min\left(p_{\text{gas}}\left(\frac{d\log\langle a \rangle}{d\log p_{\text{gas}}} < 0.05 \log\langle a \rangle\right)\right)$  and below region 2
4. Cloud deck: linear decreasing dust particle number density, exponential grain growth, *upper boundary criterion*:  $\min(p_{\text{gas}}(J_{\text{max}}^*))$ .
5. Rain edge: decreasing grain size, *upper boundary criterion*:  $\min(p_{\text{gas}}(\chi_{\text{net}} < 0))$ .
6. Cloud base: dust has vanished, *upper boundary criterion*:  $\min(p_{\text{gas}}(n_d = 0))$  and below region 1

This resembles the cloud structure found in Dehn (2007)<sup>1</sup>, except for two points. The dust free atmosphere region is here denoted as seed dominated region. Furthermore, an additional region between the seed dominated region and the fine particles region was added, because the mean grain radius shows a totally different behavior here.

The rain edge is a part of the cloud deck and the cloud base is merely the lower boundary of the cloud deck. Thus, items 4 to 6 of this structure are not separated, but are addressed in a single subsection.

<sup>1</sup>The cloud structure differs from the one in Woitke & Helling (2004). Reasons for this are discussed in Dehn (2007).

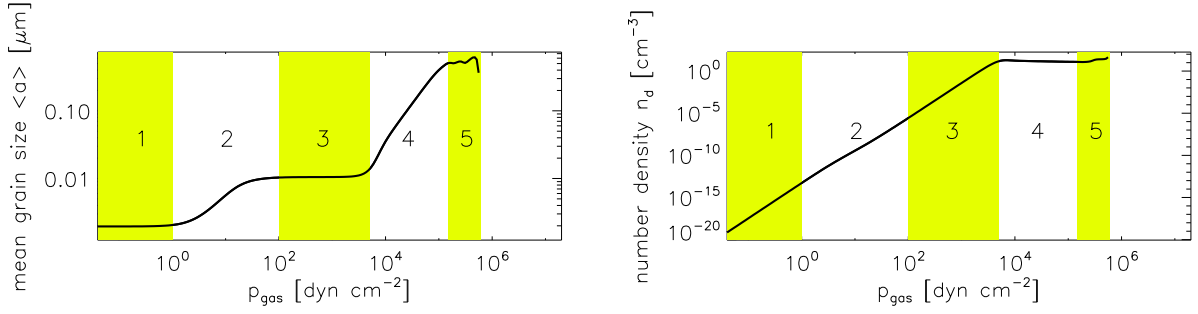


**Figure 6.1.:** Illustration of the cloud structure for  $T_{\text{eff}} = 2000$  K,  $\log(g) = 5.0$  and  $[M/H] = 0.0$  by means of the grain size and particle number density: 1 seed dominated region, 2 first growth region, 3 fine particle region, 4 cloud deck, 5 rain edge.

In the following section the general structure of the dust cloud will be described in detail, because it applies to all models of the three sequences studied here. Afterwards, each model sequence is treated in an individual section, in which the influence of the varied model parameter on the atmosphere and dust cloud structure is shown. The descriptions are followed by the required plots. All plots in each section, excepting the one concerning the convection velocity, will use the same gas pressure range, for easier comparison.

The quantities which are required in the following sections are summarized in Tab. 6.1.

quantity	variable	unit	description
gas pressure	$p_{\text{gas}}$	$\text{dyn cm}^{-2}$	local gas pressure, reference quantity
temperature	$T$	K	local temperature pressure
gas density	$\rho$	$\text{g cm}^{-3}$	local gas density
optical depth	$\tau$	-	optical depth at $1.2\mu\text{m}$ (Eq. 2.7)
convection velocity	$v_{\text{conv}}$	$\text{cm s}^{-1}$	local mean velocity of upwards moving gas cells (Eq. 2.16)
drift velocity	$v_{\text{drift}}$	$\text{cm s}^{-1}$	local fall velocity of mean size dust particles (Eq. 2.21)
sonic velocity	$v_s$	$\text{cm s}^{-1}$	local speed of noise (the model assumption: $v_{\text{drift}} < v_s$ is valid in the cloud (e.g., Fig. 6.7))
nucleation rate	$J^*$	$\text{cm}^{-3} \text{s}^{-1}$	local formation ratio of new dust seed (Eq. 2.18)
dust particle number density	$n_d$	$\text{cm}^{-3}$	local number of dust particles per cubic centimeter (Eq. A.8)
growth velocity	$\chi_{\text{net}}$	$\text{cm s}^{-1}$	temporal change of the local mean grain radius (Eq. A.12)
mean grain radius	$\langle a \rangle$	$\mu\text{m}$	local mean radius of the dust grains (Eq. A.9)
supersaturation ratio	$S_{\text{eff}}^s$	-	effective local supersaturation of species $s$
gas phase abundance	$\epsilon_i$	-	absolute gas phase abundance of element $i$ based on the local, total number of elements
volume fraction	$V_s/V_{\text{tot}}$	-	ratio of the volume $V_s$ of species $s$ within an average grain to the total mean grain volume

**Table 6.1.:** List of quantities of the dust model.

## 6.1. General dust cloud structure

In order to give an overview of the usually observed cloud structure, this section contains a general description. It applies to all models with the exception of extremely low metallicities. An example of a model with the corresponding regions of the cloud is shown in 6.2.

**1. Seed dominated region:** In the outermost layers, the atmosphere is dust free. As soon as the supersaturation ratio of  $\text{TiO}_2$  is larger than unity, nucleation is initiated, which is the criterion for the upper boundary of the seed dominated region. The nucleation rate, i.e., the formation rate of dust seeds, strongly depends on the gas density. With the increase of the gas density via the pressure, the nucleation rate increases as well. Still, the number density of dust particles remains below  $10^{-10} \text{ cm}^{-3}$  at these low pressures.

The supersaturation ratio grows to huge values at low pressures for all dust compounds taken into account. But the gas density is low and, therefore, the growth velocity remains small. Also because of the low gas density, the drift velocity is high for all dust particles. Combined with the extremely small surface of the mean particle, this leads to a negligible absorption rate of reactants. The mean dust grain radius remains below  $2 \cdot 10^{-3} \mu\text{m}$ , which is the size of the seed particles, which have been formed by nucleation processes.

**2. First growth region:** At this range, the high supersaturation, combined with the increasing gas density, results in a rise of the mean grain radius (Eq. A.12). As the mean dust particle surface increases, the growth velocity rises even more. The growth becomes much more efficient, leading to larger grain sizes with increasing pressure.

The supersaturation ratios reach their maxima at this range. The local temperature is still almost unaffected by the dust and rises only slowly with the gas pressure. Therefore, it is not the reason for these maxima. The peak is much more due to the fact that the nucleation rate and, by this, the dust particle number density increase the element consumption by the grain growth to a degree that more elements are consumed than the overshoot mechanism is able to mix up. A strong depletion of the considered elements is initiated. In the following deeper layers, the rise of the gas density with depth is no longer able to compensate for the depletion. From this point on, the growth velocity starts to decrease.

As a result of the rising gas density with depth, the drift velocity decreases at this range. This growth phase delays the decrease, because the drift velocity is proportional to the grain radius.

The increasing number density of the dust particles with the gas pressure is hardly affected by this growth phase. As only a small number of monomers<sup>2</sup> is needed in order to form a seed particle, the highly supersaturated gas is still sufficient to guarantee a continuation of the strong increase of the dust particle number density. Only a small bend can be seen in the curves, after the saturation has crossed its maximum.

The onset of efficient dust growth increases the opacity, which heats the local gas<sup>3</sup>. As a result the temperature gradient is increased (compare, e.g., Figs. 6.3 and 6.13).

**3. Fine particle region:** After the growth phase, the mean grain radius remains almost constant, because the nucleation rate  $J^*$  grows exponentially and, therefore, also the number density of dust

---

<sup>2</sup>Dust seeds consist of 1000  $\text{TiO}_2$  monomers.

<sup>3</sup>The dust is in thermal equilibrium with the surrounding gas (see Sec. 2.2).

particles. This is due to the increasing concentration of  $\text{TiO}_2$ , which is a result of the rising gas density.

The reason for the small growth velocity  $\chi_{\text{net}}$  is the low concentration of reactants because the strong depletion more than compensates for the increasing gas density. The depletion becomes stronger with rising pressure because the increasing nucleation rate causes rising numbers of dust particles. The previously undepleted region is dominated by strong growth. This yields a depletion, which causes a drop of the growth velocity, until the replenishment by the convective overshoot is able to balance the consumption by the dust growth. The strong depletion is the reason for the strong decrease of the supersaturation ratios.

In fact, the rising number of dust particles, combined with the low growth velocity could even cause a drop of the mean particle size, but this is not observed in the presented models. The mean grain radius remains constant over this pressure range, even though the growth velocity is low and the number of particles is rising. This can be explained as follows: Two consecutive atmosphere layers are considered. In the outer layer  $i$  the mean grain size is  $\langle a \rangle_i$  and the total number of dust particles is  $n_i$ . The second layer is defined by the condition that the number of new seed particles, which have formed between the two layers, equals the number of previously existing dust grains  $n_{\text{seeds},i} \approx n_i$ . Between the two layers the grains of the first layer show a strong growth of the order  $\Delta a \approx \langle a \rangle_i$ . For the mean grain size  $\langle a \rangle_{i+1}$  in the second layer follows:

$$\langle a \rangle_{i+1} = \frac{n_{\text{seeds},i} \cdot a_{\text{min}} + n_i \cdot (\langle a \rangle_i + \Delta a)}{n_{\text{seeds},i} + n_i} \quad (6.1)$$

$$= \frac{a_{\text{min}} + 2\langle a \rangle_i}{2}, \quad (6.2)$$

where  $a_{\text{min}}$  is the radius of the newly formed dust seeds. The approximation  $\frac{a_{\text{min}}}{\langle a \rangle_i} \approx 0$  yields:

$$\frac{\langle a \rangle_{i+1}}{\langle a \rangle_i} = 1. \quad (6.3)$$

Thus, the mean grain size remains almost constant over this range of pressure, even though the particles show a strong growth of the order of their own size.

The exponential rise of the dust particle number density with the gas pressure leads to an increase of the total dust opacities, which increases the temperature gradient (compare, e.g., Figs. 6.3 and 6.13).

The supersaturation drops very fast with pressure and rising depletion. This is combined with an increase in the local temperature. Thus, at a certain depth the conditions are met where the exponential growth of the nucleation rate ends and is replaced by a fast drop. The maximum nucleation rate marks the end of the fine particle region and the upper boundary of the so-called cloud deck.

The dust particle number density is at a first maximum at this point, which is a result of the maximum nucleation ratio and accumulation due to the minimum in the drift velocity.

With the end of the exponential growth of the dust particle number density, after the nucleation rate maximum is reached, the element consumption is no longer at an exponential rise. Thus, the depletion has reached its minimum at the upper edge of the cloud deck and the local element abundances in the gas phase re-increase.

**4-6. Cloud deck, rain edge and cloud base:** As soon as the nucleation rate has passed its maximum, it drops rapidly. Because of this, an increase of the dust particle number density is no

longer perceptible. The mean grain size is no longer affected by the formation of new seeds. Thus, the mean grain size starts to increase once again. The growth velocity increases, while the resulting larger grain sizes stall the drop of the drift velocity.

The gas at the onset of the cloud deck is still supersaturated and the concentration of the reactants is rising with depth. Though the growth velocity is lower than in the first growth region, the mean grain size reaches much larger values, due to the much lower drift velocity, which is a result of the increasing density with the gas pressure.

The high number density and the strong growth of dust grains below the cloud deck are the cause for rising opacities, which bring about a higher local temperature. Thus, the supersaturation ratios are dropping fast towards higher pressure. Thus, the grain growth becomes more dependent on the local temperature with increasing pressure.

At certain gas temperatures the supersaturation ratios of the individual dust species will fall below unity. From this point on, the considered species do no longer contribute to the growth of the dust particles, but start to evaporate from the grain surfaces. In addition, a supersaturation of  $\text{TiO}_2$  below unity means the nucleation rate, which is already negligibly small at this range, finally reaches zero. As the elements, contained in the considered species, are no longer consumed by growth, their gas phase abundances remain in agreement with the given metallicity of the atmosphere model at the following layers. The evaporation of the dust species even increases these values. Depending on the width of the pressure range at which the evaporation takes place and the dust particle number density, this enrichment has a varied impact on the model. It has a strong influence on the opacities, but only a weak influence on the local temperature, compared to the influence of the dust cloud.

The different dust species become thermally unstable at different depths. Thus, at certain depth some species might still contribute to the growth of the dust particles, while other species are evaporating at the same depth. As a result, the mean grain radius is no longer increasing monotonously, but shows local minima. The distinct evaporation zones (rain edges) lead to local enrichment of the element abundances, accompanied by modified opacities.

At the maximum of the mean grain size, the dust particle number density has dropped to 50 – 60% of its maximum at the upper boundary of the cloud deck. As it was already mentioned by [Woitke & Helling \(2004\)](#) and [Dehn \(2007\)](#), this reduction in number density is not due to evaporation of particles, but is simply a result of the drift velocity. The velocity of the dust particles increases with their size. Thus, the accumulation of dust particles at the onset of the cloud deck is softened by higher velocities at the deeper layers. Due to the evaporation of the dust particles at the bottom of the cloud, the drift velocity converges to zero, which results in a very strong accumulation of extremely small dust particles and thus the peak in the dust particle number density at the cloud base.

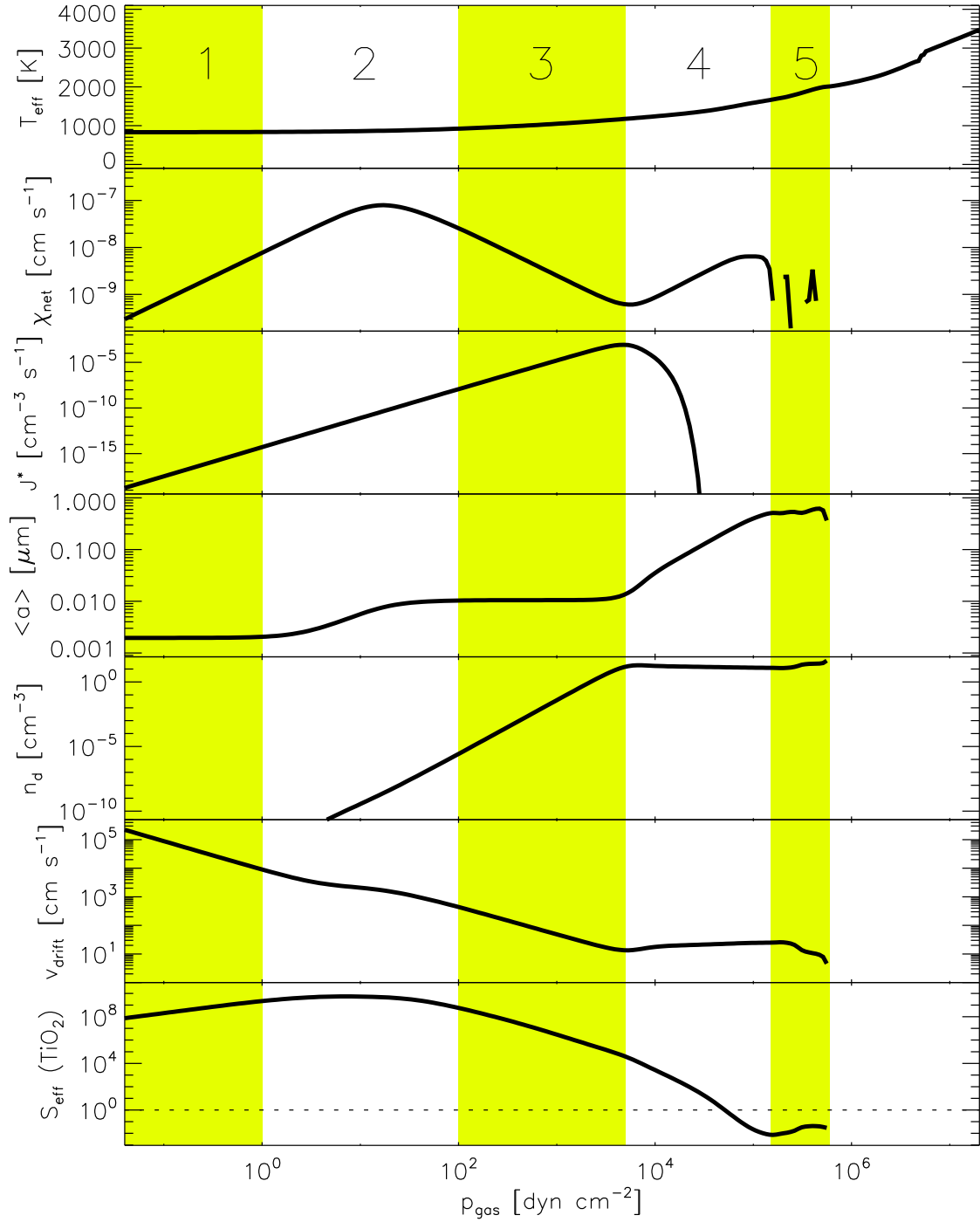


**Figure 6.2.:** Model quantities for  $T_{\text{eff}} = 2000\text{K}$ ,  $\log(g) = 5.0$  and  $[\text{M}/\text{H}] = 0.0$ : *top to bottom*: temperature  $T$ , growth velocity  $\chi_{\text{net}}$ , nucleation rate  $J^*$ , mean grain radius  $\langle a \rangle$ , dust particle number density  $n_d$ , drift velocity  $v_{\text{drift}}$ , effective supersaturation ratio  $S_{\text{eff}}$  of  $\text{TiO}_2$

## 6.2. Temperature sequence

This section treats the sequence of models, which have been calculated with effective temperatures between  $T_{\text{eff}} = 1500$  K and  $T_{\text{eff}} = 2500$  K. The surface gravity of all models is  $\log(g) = 5.0$ . Their metallicity is  $[M/H] = 0.0$ . The following is a description of the results, shown in Figs. 6.3 - 6.16. In general for these models, a 100 K decrease of the effective temperature, the convection zone is shifted inwards to a pressure which is 1.1 to 1.5 times higher and the maximum convection velocity drops by a factor of 1.15. This leads to a reduction in the efficiency of the element replenishment with decreasing effective temperature. For the lowest considered effective temperatures ( $T_{\text{eff}} \leq 1600$ K), the backwarming, caused by the dust, sparks a strong renewed convection above the cloud base (Fig. 6.4).

Between  $p_{\text{gas}} = 5 \cdot 10^6 \dots 6 \cdot 10^7$  dyn cm<sup>-2</sup>, there are discontinuities in the temperature curves, which can be identified as numerical insufficiencies at the convection zone edge.

Compared to the models by Dehn (2007) the dust particle number densities are higher, especially at lower effective temperatures. This is due to the fact, that the dust opacity calculations were modified, as was shown in the previous chapter. The new opacity calculations yield lower opacities and thus cause a less strong backwarming. The nucleation persists slightly longer, which results in an increased maximum particle number densities.

**1. Seed dominated region:** Due to the insignificant growth, the resulting element consumption is too low to cause a perceptible depletion up to pressures of  $10^1$  dyn cm<sup>-2</sup> (Fig. 6.15).

The gas density is only weakly affected by the effective temperature of the model, dropping by less than 0.25 orders over the whole temperature sequence (Fig. 6.5). Because the gas is highly supersaturated (Fig. 6.14), the grain size is almost unaffected by the effective temperature<sup>4</sup>. In contrast to this, the nucleation rate depends strongly on the supersaturation. At lower temperatures, the chemical equilibrium balances towards higher molecule concentrations. Thus, at lower effective temperatures, the concentration of TiO<sub>2</sub> is much higher, which causes a higher supersaturation ratio. For an undepleted atmosphere, this would lead to a much stronger nucleation rate at lower effective temperatures. The element replenishment by the overshoot mechanism is very weak at this distance from the convection zone and becomes decreasingly efficient for lower effective temperatures. Because of this, the overshoot is unable to replenish the elements which have been consumed by nucleation processes. The originally higher nucleation rates and weaker replenishment for lower effective temperatures are the reason for the stronger Ti depletion (Fig. 6.15). This depletion inverts the behaviour of the nucleation rate over the effective temperature. In the steady state, the nucleation rate does no longer drop with the increasing effective temperature, but rises by 2.5 orders of magnitude, over the whole model sequence (Fig. 6.8). Likewise, this can be seen in the dust particle number density (Fig. 6.10).

The increase of the nucleation rate is dominated by the rise of the gas density with gas pressure, because of the negligible temperature gradient in the low pressure range (Figs. 6.5 and 6.3). The increase of the gas density is almost linear on the double logarithmic scale of the plots. Thus, the nucleation rate, as well as the dust particle number density and the grain growth velocity show similar linear increase on a double logarithmic scale (Figs. 6.8 and 6.11), while the drift velocity shows a linear decrease (Fig. 6.7).

<sup>4</sup>See the term  $\left(1 - \frac{1}{S_r(T)}\right)$  in Eq. (A.12).

The drift velocity is high at this pressure range, because of the low gas densities. It is only indirectly influenced by the effective temperature, because of the weak dependence of the grain growth velocity on the local temperature. The growth velocity decreases marginally with the effective temperature (Fig. 6.11). The result is a slight increase the drift velocity (Fig. 6.7). Thus, the drift of the particles balances the variation in the growth velocity. This leads to a grain size at the low pressure range, which is unaffected by the effective temperature (Fig. 6.13).

The growth of the dust particles is weak, compared to the nucleation. Thus, all dust particles are almost fully made of  $\text{TiO}_2[s]^5$  at this zone of the atmosphere (Fig. 6.16). Neglecting Ti, which is much less abundant than O and thus is already strongly depleted by the nucleation at very low pressures, the gas phase abundances of the considered elements show no perceptible depletion (Fig. 6.15). The minimum of the Ti abundance in the gas phase shifts from approximately  $10^{-5} \text{ dyn cm}^{-2}$  at  $T_{\text{eff}} = 1500 \text{ K}$  to  $10^0 \text{ dyn cm}^{-2}$  at  $T_{\text{eff}} = 2500 \text{ K}$  and decreases by 6 orders of magnitude.

**2. First growth region:** At about  $1 \text{ dyn cm}^{-2}$  the previously observed behaviour of the grain size starts to change. The growth of the dust particles becomes strong enough to be perceptible (Fig. 6.13).

Between 1 and  $10 \text{ dyn cm}^{-2}$  the effective supersaturation ratios peak in all models of the sequence (Fig. 6.14). Beyond  $20 \text{ dyn cm}^{-2}$  the growth velocity is strongly decreasing (Fig. 6.11). At  $10^2 \text{ dyn cm}^{-2}$  the growth of the mean grain size has effectively ceased, at a mean radius of approximately  $0.01 \mu\text{m}$  (Fig. 6.13). Due to the still large supersaturation, the growth has been almost independent from the effective temperature of the model. Thus, all models show similar grain sizes at this atmospheric region. The outward shift of the effective growth phase for decreasing effective temperature, due to the higher supersaturation, is hardly perceptible.

At lower effective temperatures, the chemical equilibrium favours  $\text{MgSiO}_3[s]$  and by a smaller degree  $\text{Mg}_2\text{SiO}_4[s]$  over  $\text{MgO}[s]$  and  $\text{SiO}_2[s]$ . Thus, the composition of the dust grains is slightly varied over the effective temperature sequence (Fig. 6.16). The variations are about 5-10% of the total grain volume per solid species.

So far, the difference to the models by Dehn (2007) is negligible.

**3. Fine particle region:** The cooler model atmospheres have a higher supersaturation, because their local temperatures are lower at similar pressures (Fig. 6.14). Hence, the maximum of the nucleation rate is shifted inwards for decreasing effective temperatures (Fig. 6.8). At  $T_{\text{eff}} = 2500 \text{ K}$  this boundary can be found at a pressure of  $4 \cdot 10^2 \text{ dyn cm}^{-2}$ , rising to  $10^4 \text{ dyn cm}^{-2}$  for  $T_{\text{eff}} = 1500 \text{ K}$ . The gas density and thus the concentration of reactants increases with the pressure. Therefore, the maximum nucleation rate is higher for lower effective temperatures. At  $T_{\text{eff}} = 2500 \text{ K}$  the maximum nucleation rate reaches almost  $3 \cdot 10^{-4} \text{ cm}^{-3} \text{ s}^{-1}$ , while the maximum at  $T_{\text{eff}} = 1500 \text{ K}$  is at  $7 \cdot 10^{-3} \text{ cm}^{-3} \text{ s}^{-1}$ , thus increasing by 1.4 orders of magnitude.

At the edge to the cloud deck, the dust particle number density reaches a first maximum (Fig. 6.9). This maximum ranges from  $5 \text{ cm}^{-3}$  for  $T_{\text{eff}} = 2500 \text{ K}$  to  $550 \text{ cm}^{-3}$  for  $T_{\text{eff}} = 1500 \text{ K}$ . A decrease of the effective temperature by  $\Delta T = 100 \text{ K}$  results in an approximate factor of 1.9 in the number density. Dehn (2007) observed smaller maximum number densities. This is due to the opacity calculations, which have been modified in this work. As a result, the backwarming is less strong in the new models, which enables the nucleation to persist slightly longer. Thus, in all new models

---

<sup>5</sup>[s] indicates species in the solid phase.

the lower boundary of this range is slightly shifted to higher pressure, accompanied by higher dust particle number densities.

As all compounds are still strongly supersaturated and their depletion grows almost equally strong, their share in the growth is constant (Eq. A.12). Thus the composition of the particles remains unaltered in the fine particle region (Fig. 6.16).

**4-6. Cloud deck, rain edge and cloud base:** Considering the drift velocity, the increase of the dust grain radius balances the increasing gas density for rising gas pressure (Figs. 6.7 and 6.12). Thus the drift velocity does not drop any further, but is stabilized with only a marginal increase at higher gas pressures. As it was already mentioned, the less efficient replenishment for lower effective temperatures causes the cloud deck to move inwards to higher pressures for lower effective temperatures. The drift velocity is lower at the resulting higher gas density. Between 2500K and 1500K it drops by two orders of magnitude. Lower drift velocities result in a stronger accumulation of dust particles at a particular height in the atmosphere (Fig. 6.9). This is combined with a higher dust particle number density at the upper edge of the cloud deck, due to the higher maximum nucleation rate for lower effective temperatures (Fig. 6.8). Thus, the dust particle number density at the cloud deck is much larger for lower effective temperatures.

As was mentioned before, the evaporation of the dust species causes a local enrichment of the elements (Fig. 6.15). At the higher effective temperatures of this sequence, these enriched layers show roughly a 10 – 25% increase of the local gas phase abundances, compared to the undepleted abundances of the models. Lower effective temperatures, accompanied by the higher number densities of these models, show a rise to some 100% larger local abundances at the evaporation layers.

As it was already mentioned, the different dust species evaporate at different depths, which results in local minima of the mean grain radius (Fig. 6.12). One example for this is the minimum of the mean grain radius for  $T_{\text{eff}} = 2500 \text{ K}$  at  $10^4 \text{ dyn cm}^{-2}$ . At this point  $\text{Mg}_2\text{SiO}_4[s]$ ,  $\text{SiO}_2[s]$ ,  $\text{MgSiO}_3[s]$  and  $\text{MgO}[s]$  are almost fully evaporated, while  $\text{Fe}[s]$  is strongly evaporating, shortly after its maximum growth, and  $\text{TiO}_2[s]$  does neither grow nor evaporate (Fig. 6.15).  $\text{Al}_2\text{O}_3[s]$  is the remaining growing species, which dominates the dust grains in the deeper layers, until the grain size peaks at  $7 \cdot 10^4 \text{ dyn cm}^{-2}$  and the particles eventually evaporate.

The dust opacities rise with the dust grain size and the dust particle number density. Especially the strongly growing grain size results in a strong rise of the temperature gradient (Fig. 6.3). Only at local minima of the growth, due to the onset of evaporation of one dust species, the temperature gradient becomes weaker again. These minima can be seen as bumps in the temperature curves between  $10^4$  and  $10^6 \text{ dyn cm}^{-2}$ . Though there should be one bump for every dust species, only two bumps are observed per curve. The evaporation edges of  $\text{Mg}_2\text{SiO}_4[s]$ ,  $\text{SiO}_2[s]$ ,  $\text{MgSiO}_3[s]$  and  $\text{MgO}[s]$  are too close to each other to be resolved.  $\text{TiO}_2[s]$  and  $\text{Al}_2\text{O}_3[s]$  also evaporate at very similar temperatures, while the evaporation edge of  $\text{Fe}[s]$  blends into the two bumps and can not be seen.

For lower effective temperatures, the growth phase is initiated at higher pressures (Fig. 6.12). Due to the lower local temperatures in these models, the evaporation of the dust species is shifted to higher pressures as well. Hence, the bumps in the temperature curves are moved inwards (Fig. 6.3). Because of the higher number densities of models with lower effective temperature, their local temperature increases stronger, due to the increasing dust opacities. Higher temperatures are reached after shorter pressure intervals. Thus, the critical conditions for the evaporation of the dust species are reached earlier after the onset of efficient growth (Fig. 6.14). Successive evaporation edges are

much closer to each other at lower effective temperatures. Below  $T_{\text{eff}} = 2000$  K the first bump in the temperature curves is barely influenced by the effective temperature and remains at around  $3 \cdot 10^5$  dyn cm<sup>-2</sup>. The second bump is even more stable at  $1 \cdot 10^6$  dyn cm<sup>-2</sup>. Below it, all dust has vanished. This edge is called the cloud base.

At around  $10^6$  dyn cm<sup>-2</sup> and below, an almost stable feature in the temperature structure is observed (Fig. 6.3). The gas below is heated by the dust cloud via backwarming, which has already been observed by Dehn (2007). However, the dust particle number densities are much higher in the new models, which amplifies this feature (Fig. 6.9). Hence, the dust cloud becomes more opaque. This intensifies the backwarming, which compensates for the lower effective temperature. The stable temperature of roughly 2000 K at the feature is simply the critical temperature at this pressure, at which the last dust species evaporates.

The dust cloud is located at higher pressures for lower effective temperatures, but is unable to sink any deeper than  $10^6$  dyn cm<sup>-2</sup>, because it is pushed outwards by the backwarming (Figs. 6.3 and 6.12).

At  $T_{\text{eff}} = 2500$  K the maximum mean grain radius is about  $0.85 \mu\text{m}$  at  $6 \cdot 10^4$  dyn cm<sup>-2</sup>. Due to the higher supersaturation at the outer cloud deck for lower effective temperatures, the mean grain size becomes steeper. Combined with the high number densities, this causes a larger temperature gradient (Fig. 6.9). Thus the following evaporation is much faster, while the growth of  $\text{Al}_2\text{O}_3$  becomes less efficient. As a result, both maxima of the mean grain size have an equal value around  $0.60 \mu\text{m}$  at  $2 \cdot 10^5$  dyn cm<sup>-2</sup> at  $T_{\text{eff}} = 2000$  K (Fig. 6.12). Below  $T_{\text{eff}} = 2000$  K the second maximum is lower than the first. The maximum mean grain radius for  $T_{\text{eff}} = 1500$  K drops to  $0.5 \mu\text{m}$ . For even lower effective temperatures the second maximum is likely going to vanish and the first maximum will decrease, because the rising dust particle number density will cause a strong backwarming, which will result in earlier evaporation of larger grains.

At the cloud deck, the total alteration of the composition of the dust grains over the temperature sequence is about 20% of the total grain volume (Fig. 6.16). Because of the steeper temperature gradient for models of lower effective temperature,  $\text{MgSiO}_3[s]$  and  $\text{Mg}_2\text{SiO}_4[s]$  evaporate slightly faster at the first maximum of the grain size radius. Thus, the volume fraction of  $\text{MgO}[s]$  and  $\text{SiO}_2[s]$  are slightly increased at this maximum for lower effective temperatures. The large temperature gradients result in a fast evaporation of these four species, while the growth of  $\text{Al}_2\text{O}_3[s]$  is not yet efficient (Figs. 6.3 and 6.12). Thus, the volume fraction of  $\text{Fe}[s]$  increases by a factor of 4 at  $T_{\text{eff}} = 2500$  K. Due to the faster evaporation of the Mg-bearing molecules and the slower growth of  $\text{Al}_2\text{O}_3[s]$ , caused by the steeper temperature gradient, this factor increases to 5 at  $T_{\text{eff}} = 1500$  K. The steeper temperature gradient also influences the second maximum of the mean grain radius. At higher effective temperatures, the dust grains at this maximum are made up of 95%  $\text{Al}_2\text{O}_3$  and 5%  $\text{TiO}_2$ , because all the iron is already evaporated (Fig. 6.16). At lower effective temperatures this shifts to 85%  $\text{Al}_2\text{O}_3$ , 10%  $\text{Fe}$  and 5%  $\text{TiO}_2$ , because iron is not yet fully evaporated. Thus, at lower effective temperatures, iron gains more weight in the effective medium, which affects the dust opacities.

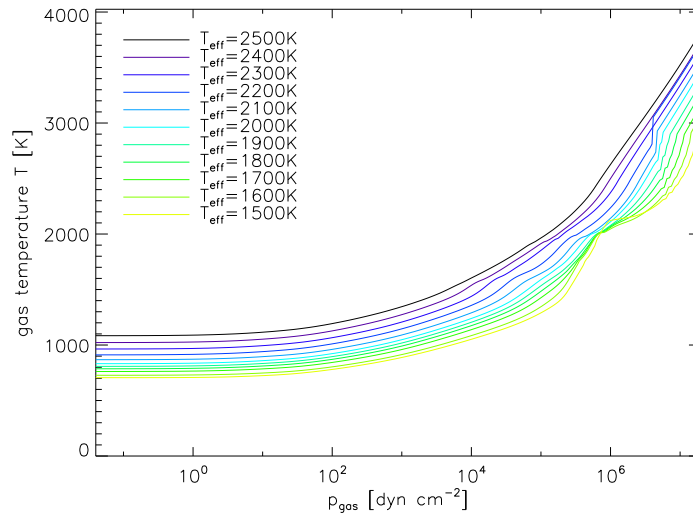


Figure 6.3.: Temperature  $T$

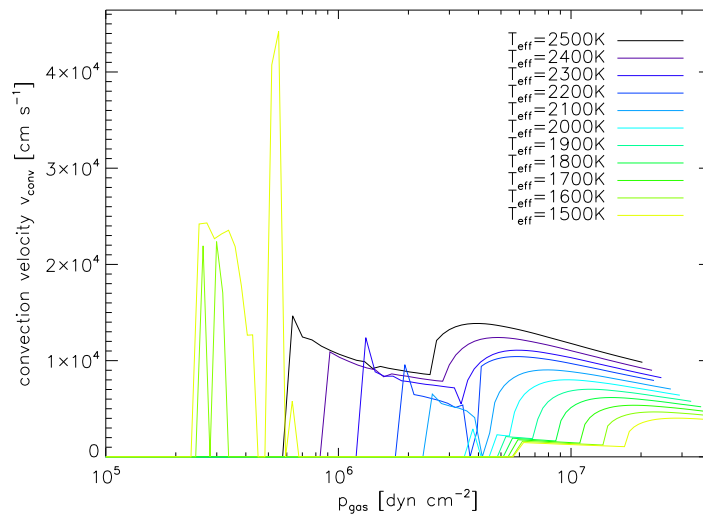
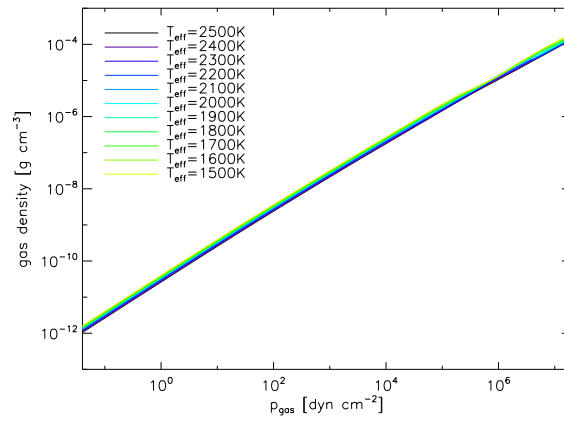
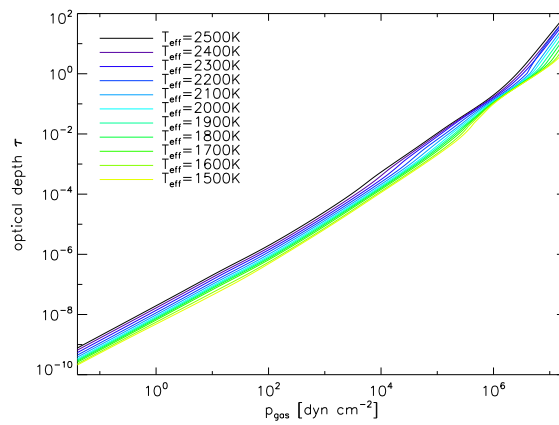
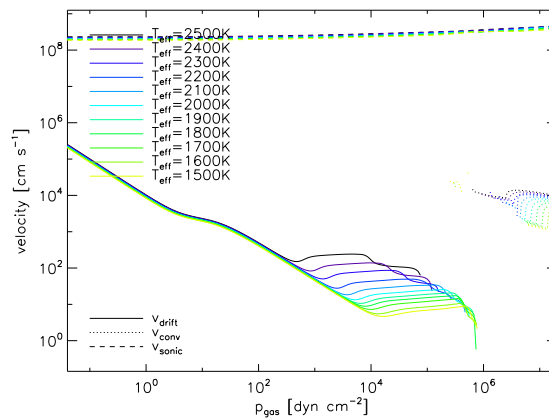
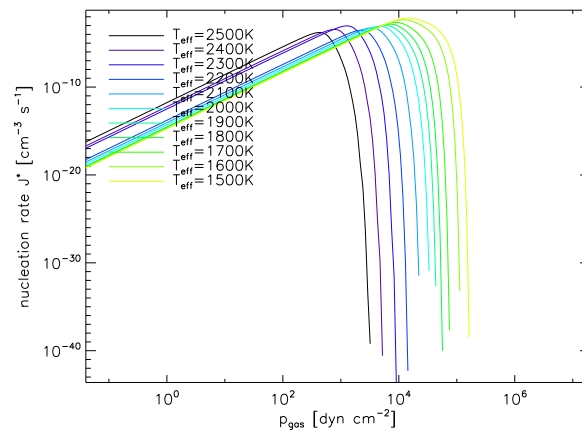


Figure 6.4.: Convection velocity  $v_{\text{conv}}$

Figure 6.5.: Gas density  $\rho$ Figure 6.6.: Optical depth  $\tau$  at  $1.2 \mu\text{m}$ 

**Figure 6.7.:** As assumed, the drift velocity  $v_{\text{drift}}$  (*solid*) remains below the sonic velocity  $v_s$  (*dashed*) for the pressure range of interest. The convection velocity  $v_{\text{conv}}$  (*dotted*) is shown for comparison.

## 6. Model sequences



**Figure 6.8.:** Nucleation rate  $J^*$

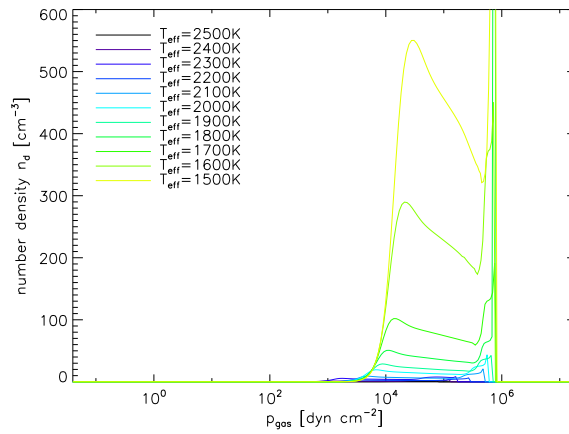


**Figure 6.9.:** Number density of dust particles  $n_d$  (linear scale)

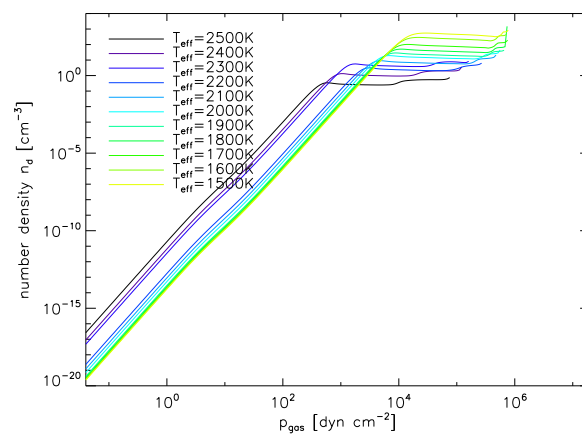


**Figure 6.10.:** Number density of dust particles  $n_d$  (logarithmic scale)

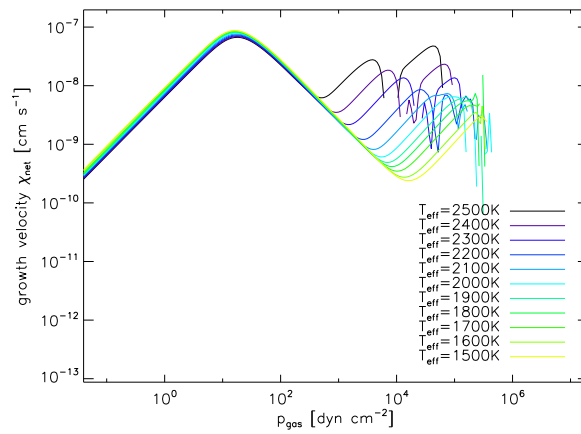


**Figure 6.11.:** Growth velocity  $\chi_{\text{net}}$

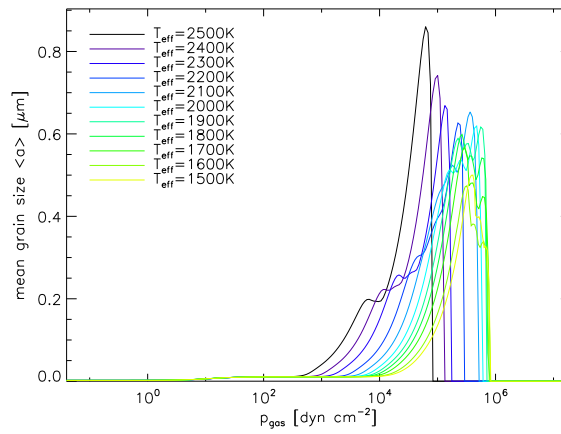


**Figure 6.12.:** Mean particle radius  $\langle a \rangle$  (linear scale)

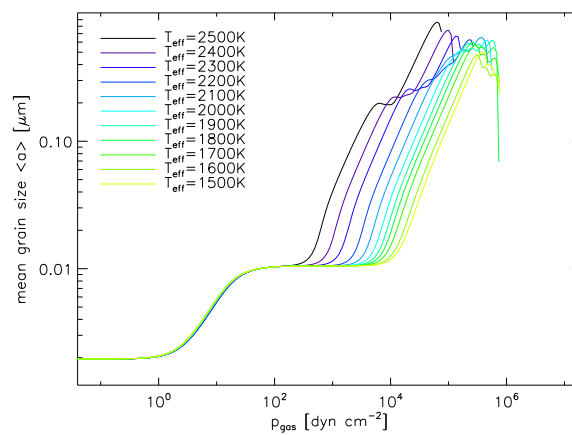


**Figure 6.13.:** Mean particle radius  $\langle a \rangle$  (logarithmic scale)

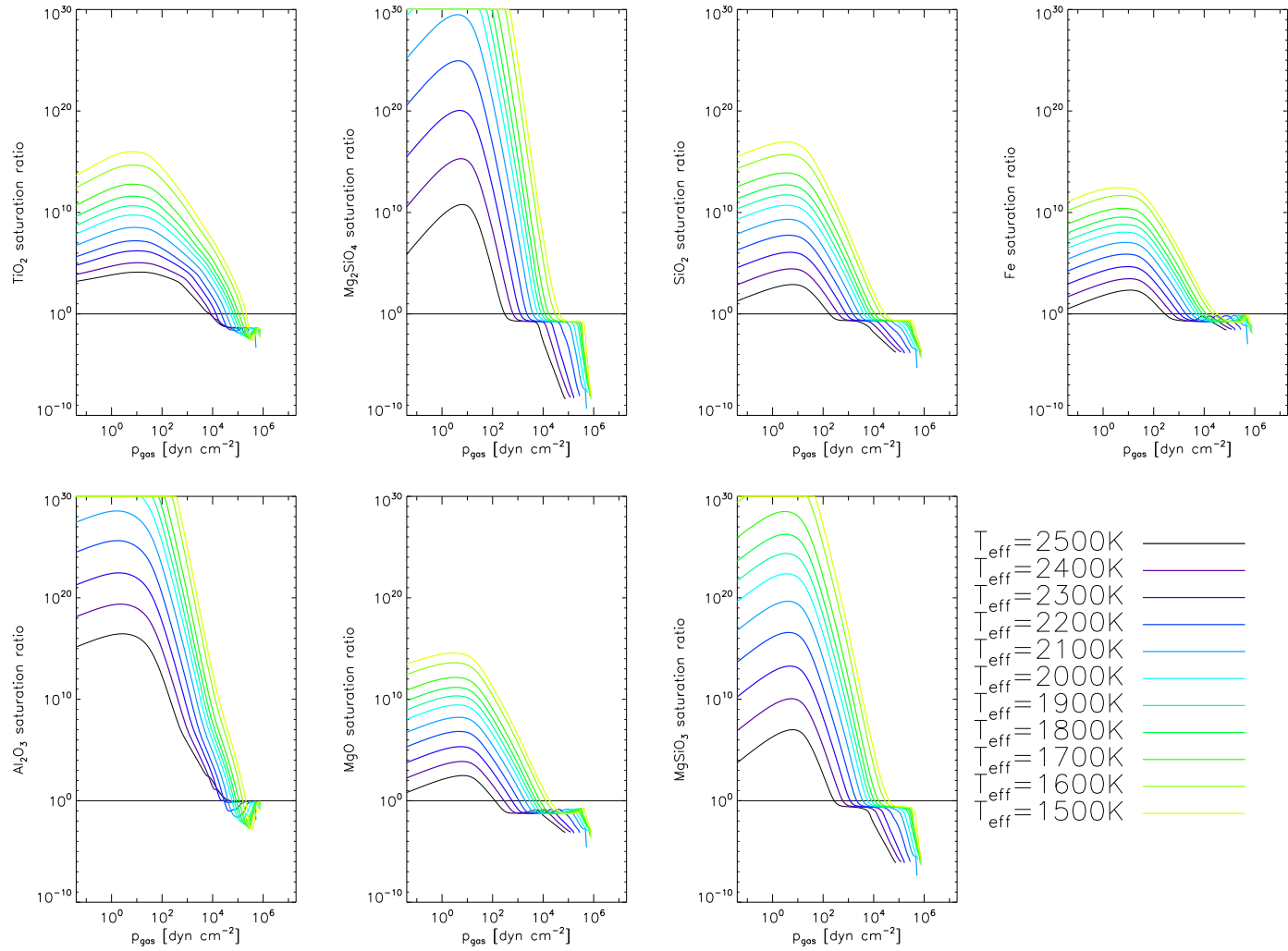
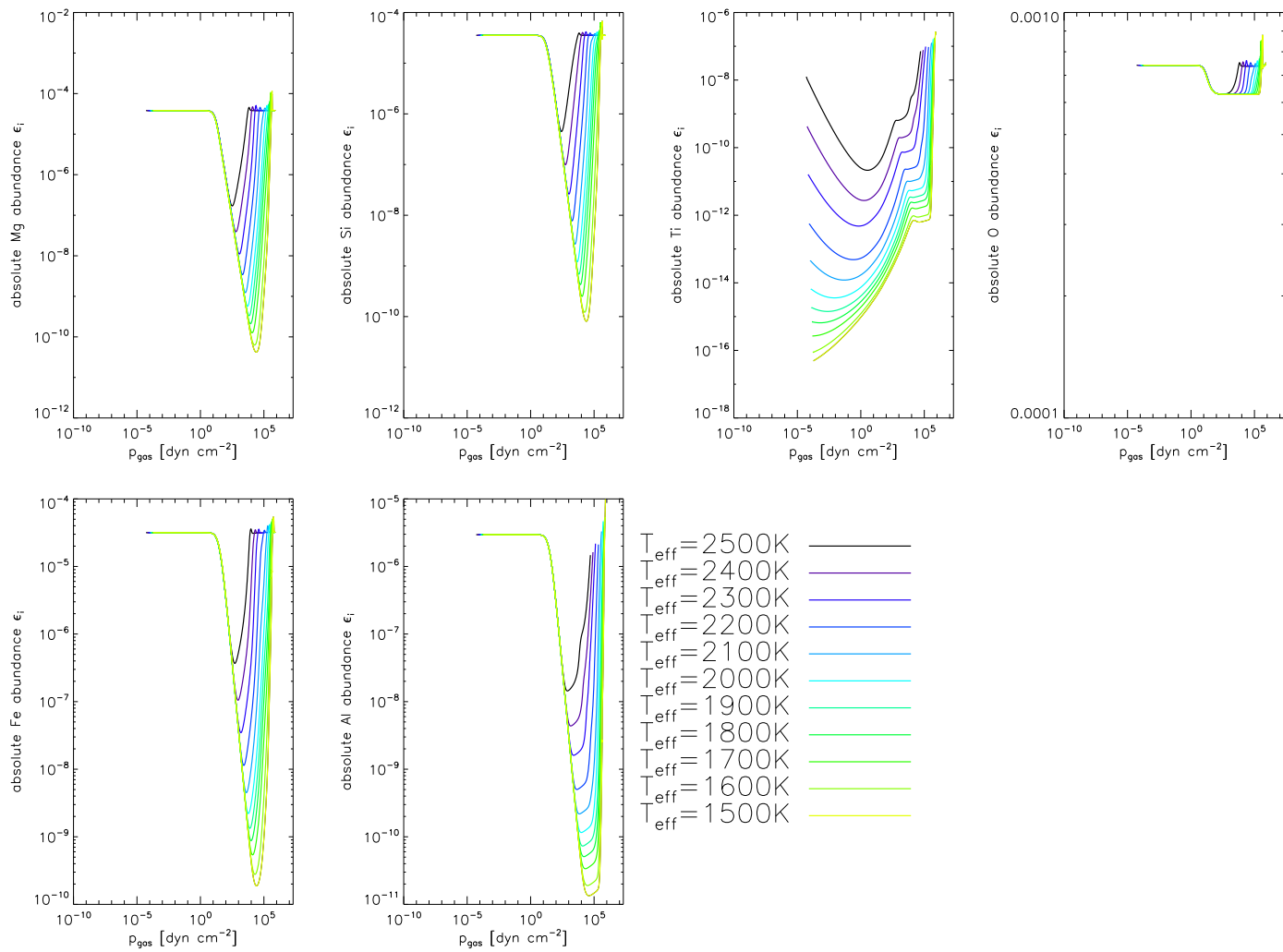
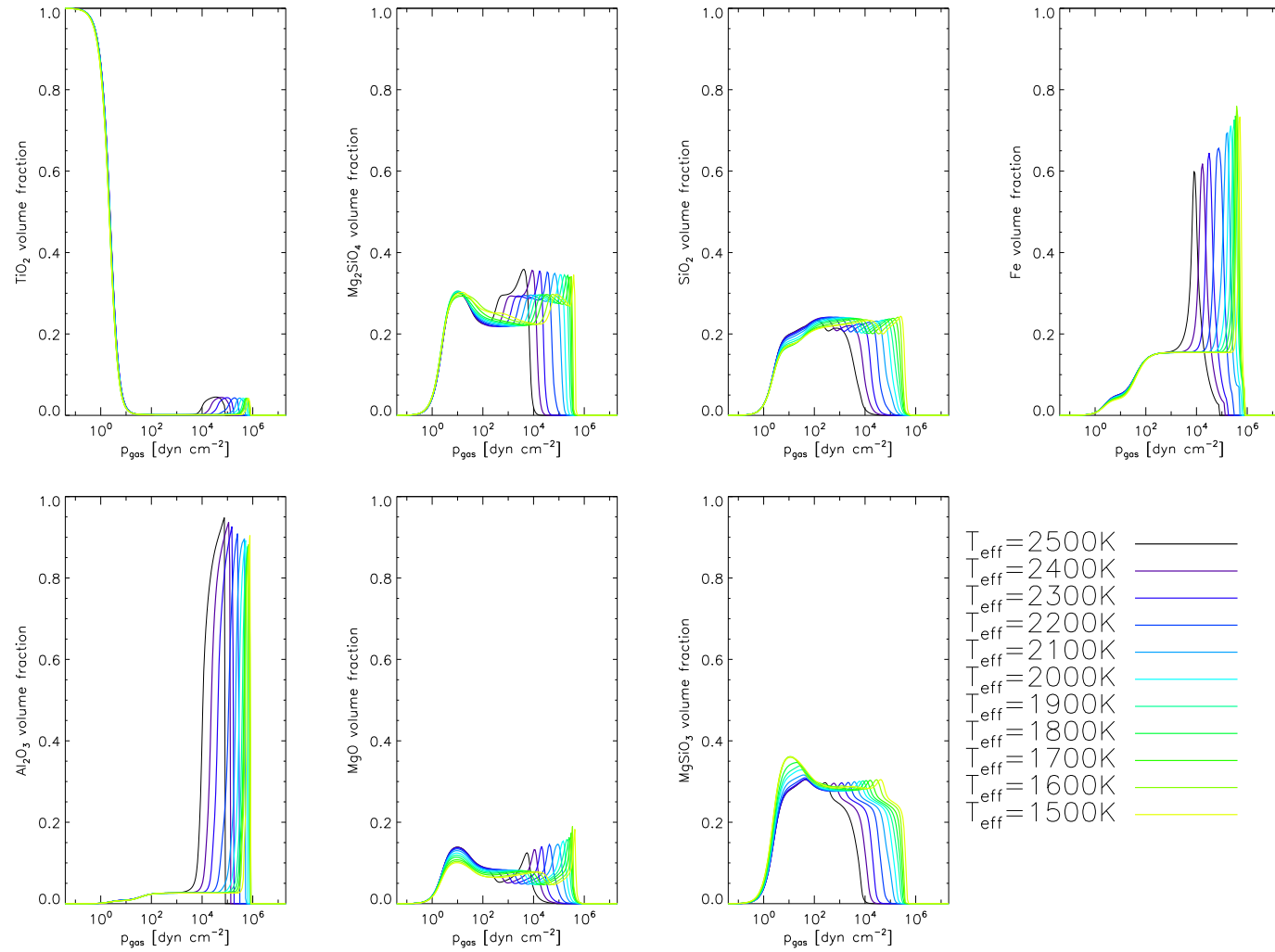


Figure 6.14.: Effective supersaturation rates  $S_{\text{eff}}^s$  of the seven dust species  $s$



**Figure 6.15.:** Absolute gas phase abundances  $\epsilon_i$  of the six considered elements



**Figure 6.16.:** Mean grain volume fractions  $V_s/V_{\text{tot}}$  of the seven considered dust species  $s$

### 6.3. Gravity sequence

For this model sequence, the gravitational acceleration was varied between  $\log(g) = 3.0$  and  $\log(g) = 6.0$ . All models have an effective temperature of  $T_{\text{eff}} = 2000$  K and a metallicity  $[M/H] = 0.0$ . This section describes Fig. 6.17 - 6.30.

The general structure of the dust cloud is hardly affected by the  $\log(g)$  of the model. Individual components of the cloud show varying characteristics, but none of the components is strongly altered or vanishes. Thus, this section will be restricted to comparison of the model sequence. For a more detailed description of the cloud structure see the previous section.

The pressure gradient is weaker for lower gravity (Eq. 2.1). Thus, the local temperature of models with lower gravity will drop slower with decreasing pressure (Fig. 6.17). The result is a shift of the dust cloud base to lower pressure ranges for lower gravity (Fig. 6.26). The gravity of the model has a strong influence on the convection (Fig. 6.18). The edge of the convection zone is located at  $1 \cdot 10^4$  dyn cm<sup>-2</sup> for  $\log(g) = 3.0$  and is shifted to  $3 \cdot 10^7$  dyn cm<sup>-2</sup> for  $\log(g) = 6.0$ . The maximum convective velocity drops from  $2.8 \cdot 10^4$  cm s<sup>-1</sup> at the lowest  $\log(g)$  to  $4.5 \cdot 10^3$  cm s<sup>-1</sup> at the highest  $\log(g)$ . Thus, models with a lower gravity have a more efficient replenishment of the higher atmosphere layers, which causes a shift of the upper cloud deck edge to lower pressure.

Again, the upgraded opacity calculations yield higher maximum dust particle number densities, compared to the results of Dehn (2007). The grain sizes remain comparable.

**1. Seed dominated region:** Over the sequence, the local temperature increases by roughly 100 K towards higher gravity at this region (Fig. 6.17). The gas density is larger for lower gravity in this pressure range (Fig. 6.19). The result is a shift of the supersaturation curves to lower pressures for lower gravity (Fig. 6.28).

Ti is strongly depleted in the outer layers, especially for higher gravity, because of the less efficient replenishment (Fig. 6.29). Thus, the nucleation rate at  $\log(g) = 3.0$  is six orders of magnitude higher than at  $\log(g) = 6.0$  (Fig. 6.22). Similarly, the number density is almost 12 orders of magnitude higher (Fig. 6.24). The drift velocity is proportional to the gravity and thus ranges over 3 orders of magnitude (Fig. 6.21). In contrast, the growth velocity is not affected by the gravity, at this pressure range, because the alterations of the reactant concentration, due to variations in the local gas density, is fully compensated by the drift velocity (Fig. 6.25). Due to the low growth velocity, high drift velocities and the exponentially growing dust particle number density, the mean grain size remains close to the size of the dust seeds  $a_{\text{min}}$  (Fig. 6.27).

**2. First growth Region:** In contrast to the effective temperature the surface gravity has a strong influence on the pressure range of the first growth phase of the mean grain size (Fig. 6.27). This is due to the fact that the supersaturation curves are shifted to lower pressures, for a lower gravity (Fig. 6.28). The maximum of the supersaturation is reached at lower pressures, as well. At this point, the overshoot mechanism is no longer capable to replenish the elements, which have been consumed by the growth. For  $\log(g) = 3.0$  the supersaturation maximum is located at  $2 \cdot 10^{-1}$  dyn cm<sup>-2</sup>. Each increase of the gravity by  $\Delta \log(g) = 0.5$  increases the pressure at the supersaturation maximum by a half order. Similar to the temperature sequence, the growth is perceptible over a pressure range of two orders of magnitude, with the supersaturation maximum at the middle.

The number density continues its exponential growth with the rising pressure and shows only a very weak bend in this range (Fig. 6.24).

Because the supersaturation maximum is located at higher pressures for higher gravities, the increase of the growth velocity with the gas density persists at greater depths (Fig. 6.25). Thus, the maximum growth velocity rises by three orders of magnitude over the model sequence. This is compensated by the drift velocity, which drops by a similar degree (Fig. 6.21). Due to the low temperature gradient at this range, the local temperature at the supersaturation maximum depends only weakly on the surface gravity (Fig. 6.17). Thus, the contribution of the dust species to the growth remains a constant fraction over the sequence and the composition of the dust grains is barely affected by the gravity in this region (Fig. 6.30).

**3. Fine particle region:** The region of steady mean grain size ranges over approximately 2.5 orders of the pressure, for all models (Fig. 6.27). The mean grain size remains constant, while the particle number density rises exponentially, which causes a strong depletion, even though the rising gas density with the gas pressure increases the concentration of reactants. The temperature gradient starts to grow perceptibly at this range, because of the rising dust particle number density (Figs. 6.17 and 6.24).

The variation of the local temperature over the sequence (Fig. 6.17) has a negligible influence on the growth at this range, because all species are still strongly supersaturated. Thus, the mean composition of the dust grains remains unaltered over the model sequence in this range (Fig. 6.30). At  $\log(g) = 6.0$  this range ends at  $5 \cdot 10^4 \text{ dyn cm}^{-2}$ . The replenishment is more efficient at lower  $\log(g)$ . Thus, a reduction by  $\Delta \log(g) = 0.5$  shifts the upper boundary of the cloud deck outwards by 0.5 orders of pressure (Fig. 6.27).

**4-6. Cloud deck, rain edge and cloud base:** The density gradient is smaller for lower gravity (Fig. 6.19). Hence, in these layers at similar pressure, the density is lower for a lower gravity. This is combined with a higher dust particle number density (Fig. 6.23), which results in a stronger depletion and higher local temperature (Fig. 6.29 and 6.17). Thus, the supersaturation rates drop below unity at lower pressure (Fig. 6.28). The nucleation rate reaches its maximum at lower pressures, as well (Fig. 6.22). At this point, the dust particle number density is also at a maximum (Fig. 6.23). Because of the much lower density, the maximum number density is also lower for a low  $\log(g)$ . This is slightly compensated by the stronger nucleation rate at lower gravity (Fig. 6.22). At  $\log(g) = 3.0$  the maximum dust particle number density is  $n_d \approx 5.0 \text{ cm}^{-3}$  (Fig. 6.23). This drops to  $0.7 \text{ cm}^{-3}$  at  $\log(g) = 4.0$ . After this minimum, the number density rises fast, with  $n_d \approx 250 \text{ cm}^{-3}$  at  $\log(g) = 6.0$ .

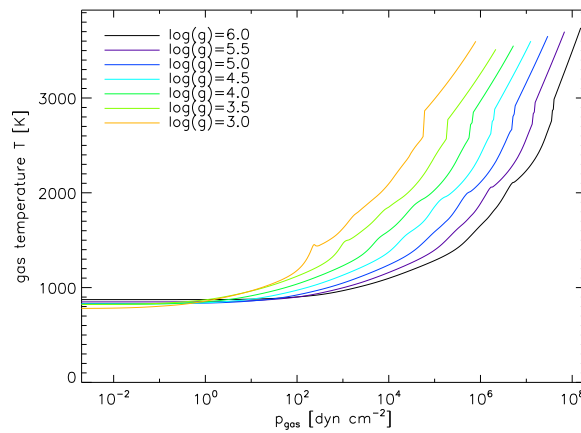
Because the number density has a dominant influence on the element depletion, its minimum at  $\log(g) = 4.0$  is also visible in the depth of the minima of the gas phase abundances (Fig. 6.29).

The supersaturation ratios drop fast in this range, because the concentration of molecular reactants decreases with the rising local temperature (Fig. 6.28). With the decreasing supersaturation rates, the temperature gains a growing influence on the growth reactions. The temperature gradient is already higher for higher gravity without considering dust (Fig. 6.17). This becomes even more stringent, because the dust particle number density is higher for a higher  $\log(g)$  (Fig. 6.23). Thus, the maxima of the mean grain size are less separated<sup>6</sup> for a higher gravity (Fig. 6.26). The maximum mean grain radius, related to the Mg-bearing species, ranges from  $\langle a \rangle = 0.12 \mu\text{m}$  to  $0.60 \mu\text{m}$  (Fig. 6.30). At lower  $\log(g)$  the mean radius shows no perceptible maximum for the growth of  $\text{Fe}[s]$ , because of the strong subsequent growth of  $\text{Al}_2\text{O}_3[s]$ . The stronger heating, due to the higher

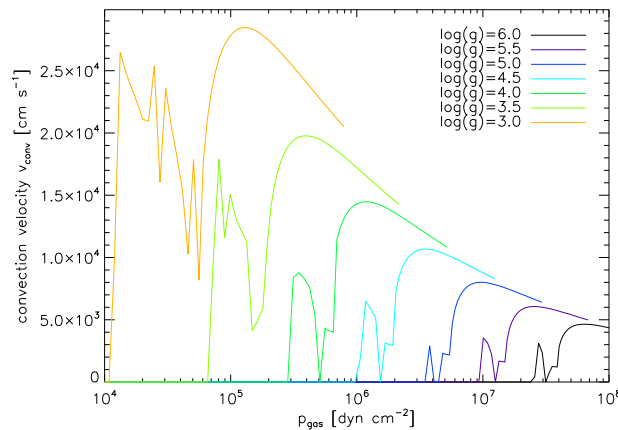
---

<sup>6</sup>logarithmic pressure scale

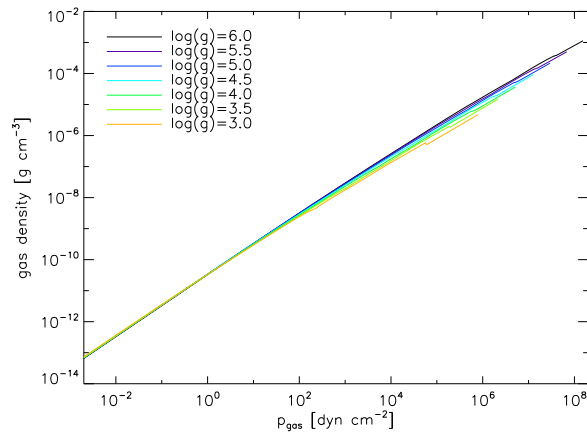
particle number densities at higher  $\log(g)$ , leads to higher local temperatures in the lower layers (Fig. 6.17). This weakens the growth of  $\text{Al}_2\text{O}_3[s]$ , because its critical conditions for evaporations are reached earlier. After  $\log(g) = 4.0$  the iron-dominated maximum in the mean grain radius is perceptible (Fig. 6.26). The maximum volume fraction of  $\text{Fe}[s]$  rises from 45% at  $\log(g) = 3.0$  to 75% at  $\log(g) = 6.0$  (Fig. 6.30). At  $\log(g) = 5.5$  the iron maximum of the mean grain radius also becomes the absolute maximum. The maximum of the  $\text{Al}_2\text{O}_3[s]$  volume fraction drops from 95% to almost 70%. Thus,  $\text{Al}_2\text{O}_3[s]$  becomes less dominant with rising gravity. Over the whole sequence, the maximum of the mean grain radius, where  $\text{Al}_2\text{O}_3[s]$  is dominant, remains roughly at  $\langle a \rangle \approx 0.6 \mu\text{m}$ , but it is likely going to vanish for even higher gravity. Similar to the effective temperature sequence, the maxima in the mean grain size are perceptible in the temperature structure (Fig. 6.17).



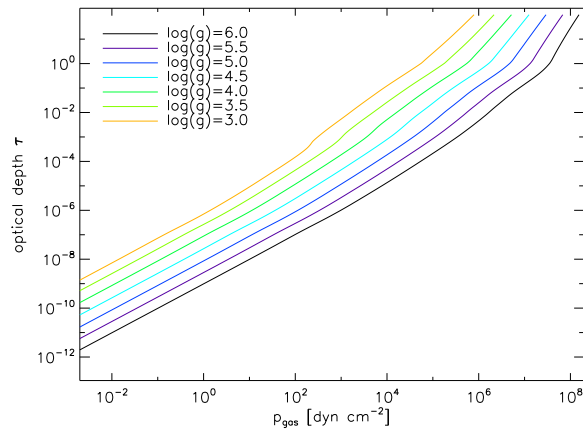
**Figure 6.17.:** Temperature  $T$



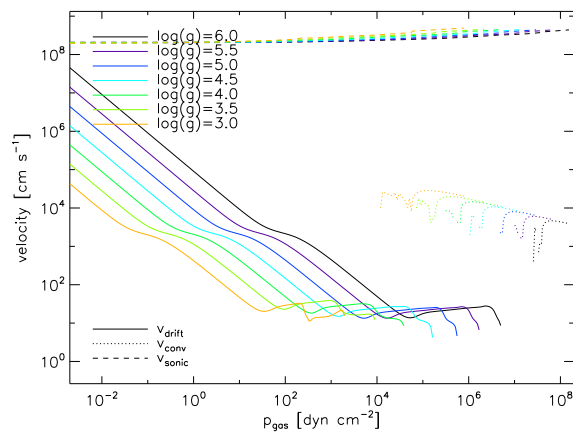
**Figure 6.18.:** Convection velocity  $v_{\text{conv}}$



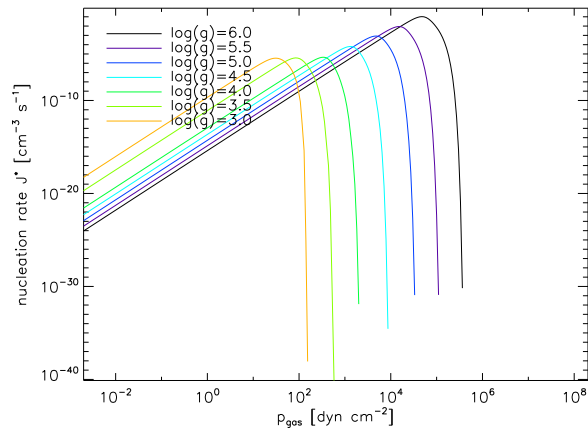
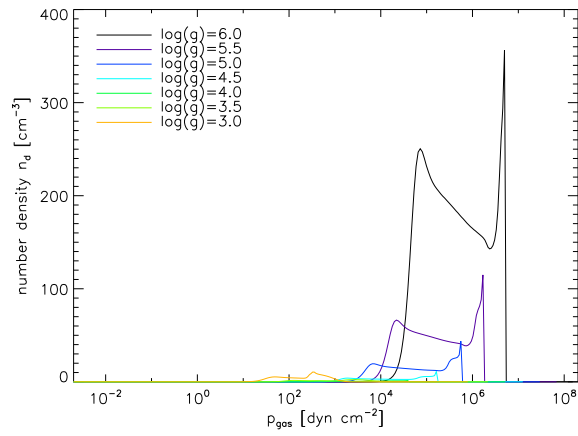
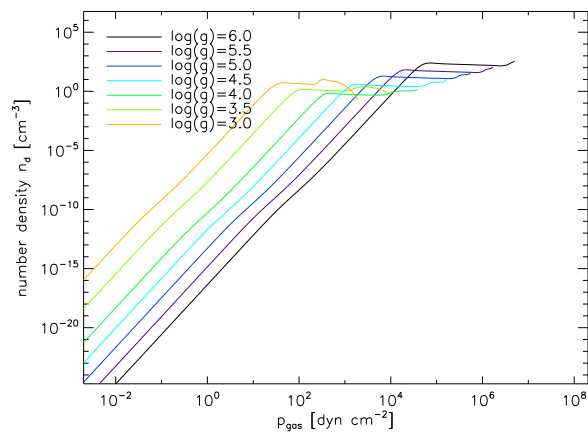
**Figure 6.19.:** Gas density  $\rho$



**Figure 6.20.:** Optical depth  $\tau$  at  $1.2 \mu\text{m}$



**Figure 6.21.:** Mean drift velocity  $v_{\text{drift}}$  (*solid*), sonic velocity  $v_s$  (*dashed*), convection velocity  $v_{\text{conv}}$  (*dotted*)

Figure 6.22.: Nucleation rate  $J^*$ Figure 6.23.: Number density of dust particles  $n_d$  (linear scale)Figure 6.24.: Number density of dust particles  $n_d$  (logarithmic scale)

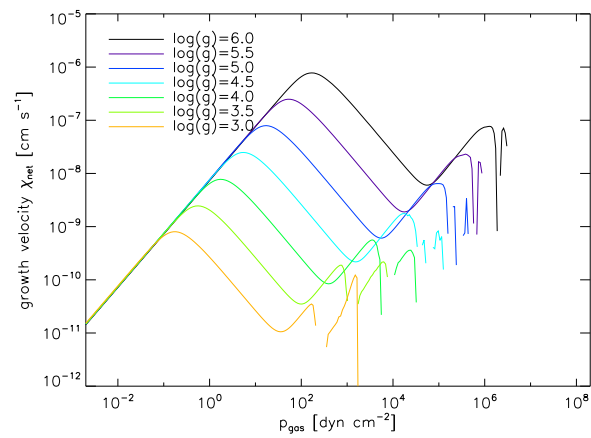


**Figure 6.25.:** Growth velocity  $\chi_{\text{net}}$

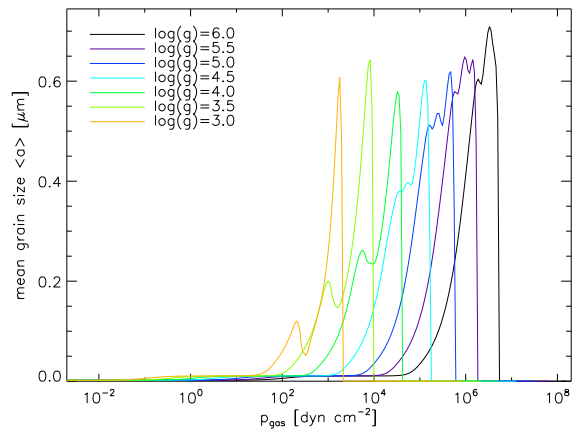


**Figure 6.26.:** Mean particle radius  $\langle a \rangle$  (linear scale)

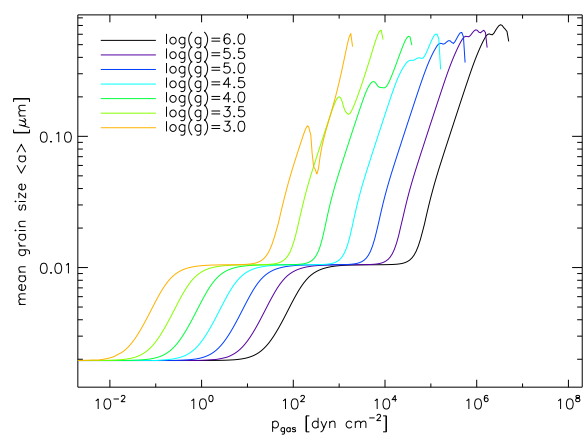


**Figure 6.27.:** Mean particle radius  $\langle a \rangle$  (logarithmic scale)

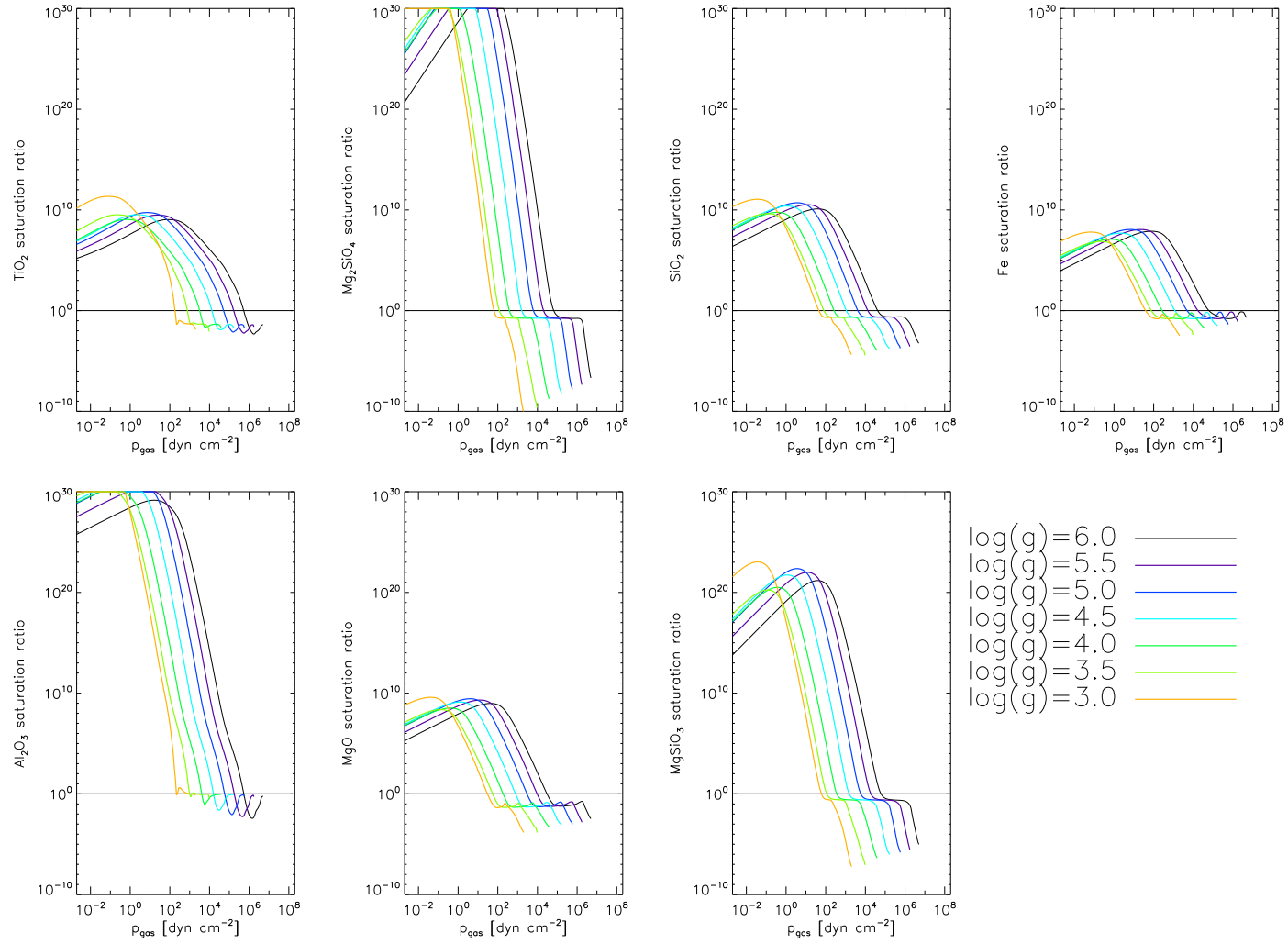


**Figure 6.28.:** Effective supersaturation rates  $S_{\text{eff}}^s$  of the seven dust species  $s$

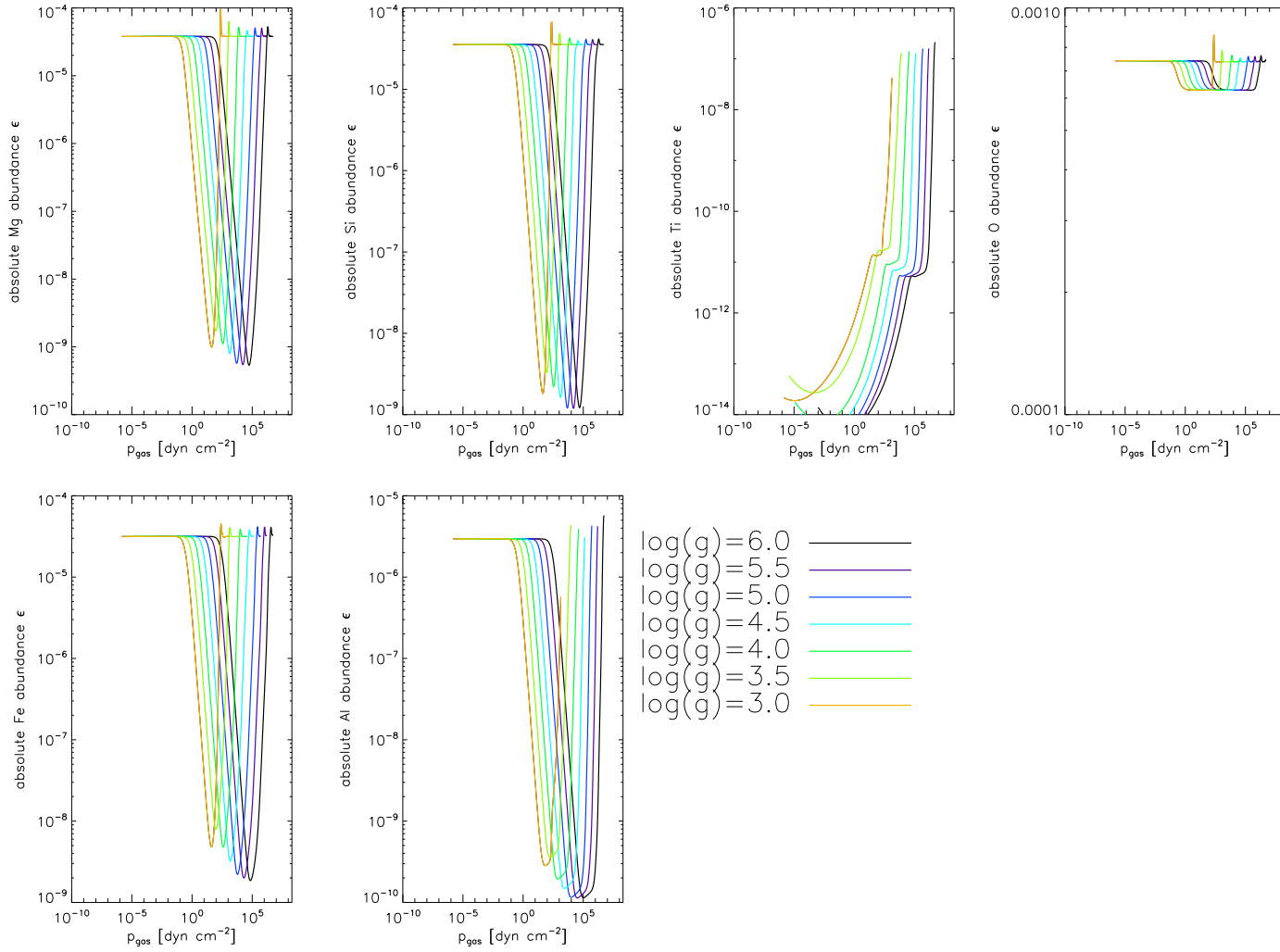


Figure 6.29.: Absolute gas phase abundances  $\epsilon_i$  of the six considered elements

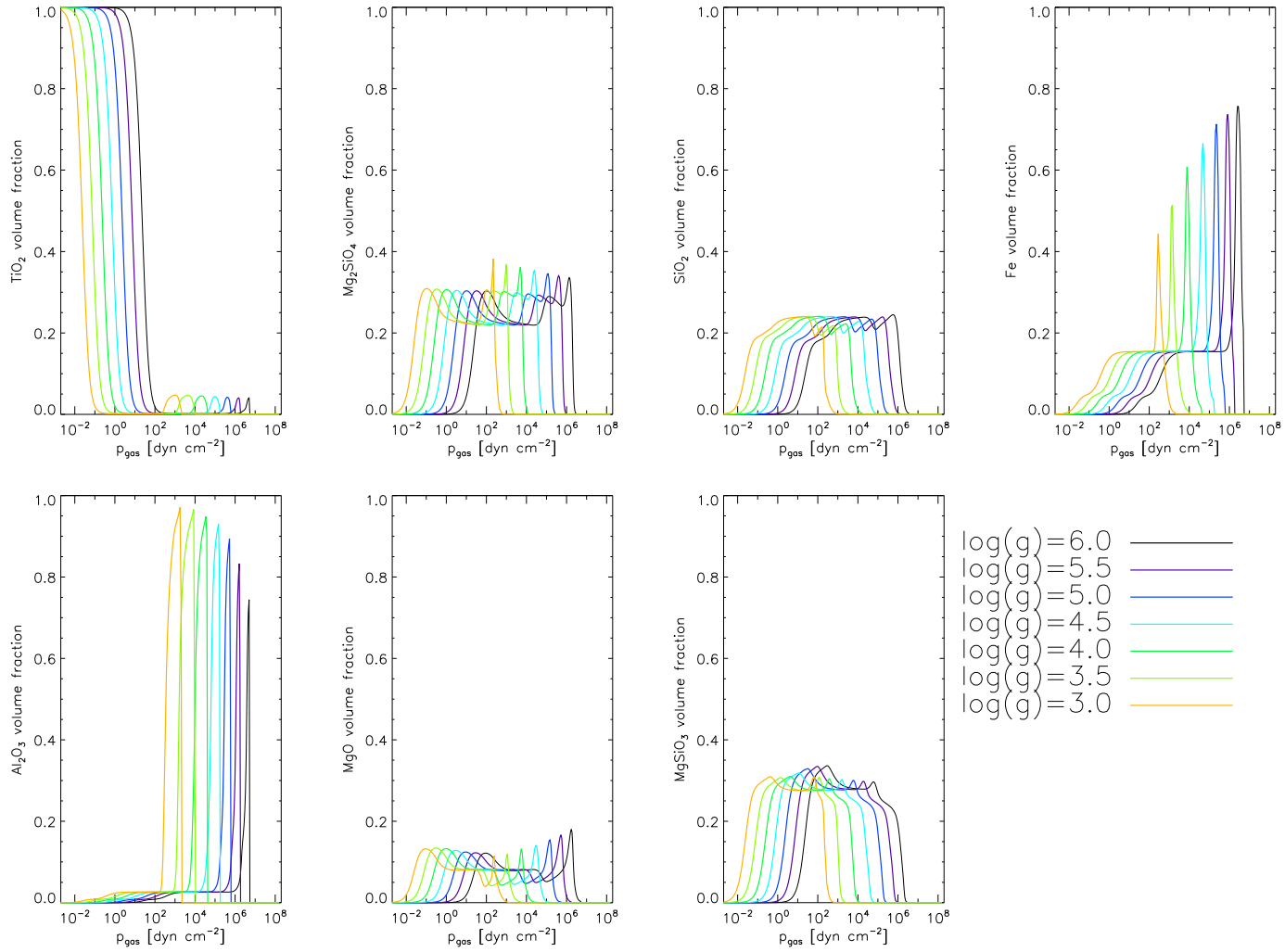


Figure 6.30.: Mean grain volume fractions  $V_s/V_{\text{tot}}$  of the seven considered dust species  $s$

## 6.4. Metallicity sequence

The third model sequence was done for a varied metallicity, ranging from  $[M/H] = -6.0$  to  $0.0$  in steps of  $\Delta[M/H] = 0.5$ . The sequence contains additional model for  $[M/H] = +0.3$ , which is a typical value for young stars. The effective temperature of all models is  $T_{\text{eff}} = 2000$  K. The assumed surface gravity has a value of  $\log(g) = 5.0$ .

Though the lower sequence metallicity boundary of  $[M/H] = -6.0$  is chosen extremely low and well beyond any observations, two noteworthy influences on the dust formation have been noticed in these the low- $[M/H]$  models:

- The lower dust cloud edge dips into the convection zone (Figs. 6.40 and 6.32).
- The outer layers feature a temperature inversion (Fig. 6.31), which can be explained by the formation of methane (Allard & Hauschildt (1995)). Consequently, the concentration of  $\text{H}_2\text{O}$ ,  $\text{TiO}$  and  $\text{VO}$  is higher, because less oxygen is bound by carbon. Thus, the molecular opacities are increased.

Especially the latter effect is of interest, because it provides an outlook to the simulation of dust in atmospheres of irradiated exo-planets, which typically feature a temperature inversion, but by completely different physical processes and much larger.

At lower metallicities, the dust particle number density becomes too small to cause a perceptible heating of the atmosphere. This can be seen in the optical depth, which is hardly affected by the metallicity, below values of  $[M/H] = -3.5$  (Fig. 6.34).

The convection zone is shifted inwards by nearly one order of pressure, between  $[M/H] = +0.3$  and  $-3.0$  (Fig. 6.32). The convection velocity decreases by more than a factor of 2. The temperature gradients, which determine the convection velocity are almost unaffected by lower metallicities. Thus, the convection zone remains stable below  $[M/H] = -3.0$ .

Compared to the models of Dehn (2007) the maximum number density of the dust particles is slightly increased for the metallicity sequence.

**1. Seed dominated region:** In the previous sequences, this region was characterized by a weak but steady inward rise of the nucleation rate and a negligible growth. This was due to the low gas density, the resulting low concentration of reactants and the high drift velocities, even though the supersaturation rates were high. A decrease in the metallicity causes a strong reduction of the concentration of reactants and reduces the supersaturation (Fig. 6.42). This is intensified by the emergence of the abovementioned temperature inversion (Fig. 6.31). Starting below  $[M/H] = -2.0$  the local temperature increases by almost 400 K. Under these conditions, the reactants become even more rare. As a result, the supersaturation of the dust species drops below unity, for metallicities lower than  $[M/H] = -3.0$ . Thus, no nucleation and consequently no grain growth take place at all at that height in the atmosphere.

At a certain depth, this temperature inversion range ends, which causes a steep rise of the supersaturation ratios. Thus, the nucleation and growth are initiated. The location of this upper boundary of the dust formation depends on the metallicity. For  $[M/H] = -3.0$  the supersaturation crosses unity at  $10^0$  dyn  $\text{cm}^{-2}$ . This descends to its maximum gas pressure at  $10^3$  dyn  $\text{cm}^{-2}$  for  $[M/H] = -5.0$  and ascends slowly for lower metallicities, due to a smoothing of the temperature step at the inversion edge.

The lower boundary of this range is defined by the onset of perceptible grain growth (Fig. 6.41). It is found at approximately  $10^0$  dyn  $\text{cm}^{-2}$  for solar metallicity. Down to  $[M/H] = -3.5$  the boundary

sinks constantly, which yields an increase of the gas pressure by 0.25 orders per  $\Delta[M/H] = 0.5$  step. At  $[M/H] = -4.0$  the transition region between the temperature inversion zone and the dust cloud has reached a depth at which the concentrations of reactants and the drift velocity have already reached values which support a strong growth. Thus, the range of negligible growth and weak, but perceptible, nucleation has effectively vanished here. The lower boundary of the temperature inversion zone becomes smoother for lower metallicities. Thus, this range reappears and becomes wider again. At  $[M/H] = -5.0$  the lower boundary reaches its maximum pressure of  $4 \cdot 10^3 \text{ dyn cm}^{-2}$ . Because of the smoother transition to the temperature inversion at lower metallicities, this boundary drifts upwards again.

**2. First growth region:** Down to a metallicity of  $[M/H] = -3.5$  the range of the first perceptible growth has a constant width of 2 orders of magnitude in pressure and is parallel shifted by 0.25 orders per  $\Delta[M/H] = 0.5$  (Fig. 6.41). Like for the other two model sequences, the saturation ratio of all dust species, except  $\text{TiO}_2[s]$ , peaks in the middle of the growth range (Fig. 6.42). The composition of the mean dust grain is stable over the model sequence for  $[M/H] > -4$  ( $\sim 35\%$   $\text{MgSiO}_3[s]$ ,  $\sim 30\%$   $\text{Mg}_2\text{SiO}_4[s]$ ,  $\sim 20\%$   $\text{SiO}_2[s]$ ,  $\sim 10\%$   $\text{MgO}[s]$ ,  $\sim 5\%$   $\text{TiO}_2[s]$ ,  $\text{Fe}[s]$  and  $\text{Al}_2\text{O}_3[s]$ ) (Fig. 6.44). For lower metallicities this is no longer true, because the temperature inversion zone reaches too deep. The saturation ratios of the species are still of the order of unity at the onset of growth. Hence, the growth is strongly influenced by the local temperature. The composition of the dust grains, which has been constant so far, is altered. The local temperature decreases at this range and thus the more thermally stable species start to condense earlier. Their volume fractions show peaks: The maximum volume fraction of 47% for  $\text{Fe}[s]$  and 8% for  $\text{Al}_2\text{O}_3[s]$  is reached for  $[M/H] = -5.0$ . For lower metallicities, the edge of the temperature inversion becomes smoother and thus the maxima vanish again.

The end of the increase of the supersaturation rates is caused by the emerging depletion of the considered elements (Figs. 6.42 and 6.43). For metallicities of  $[M/H] \geq -3.5$ , the growth becomes negligible after the pressure has risen by approximately two orders. For lower metallicities this is not valid. Here, the saturation ratios of the dust species are increasing fast with the pressure, even after the depletion of the considered elements has started. Thus, for these metallicities, the growth is much stronger at this range (Fig. 6.41). At its minimum at around  $[M/H] = -5.0$ , the width of the first growth region ranges over less than one order of pressure. Below  $[M/H] = -5.0$  the concentration of reactants becomes too low to keep up the strong growth, which is the reason for the observed widening of the range.

The maximum mean grain radius, which is reached after this range, is approximately  $0.01 \mu\text{m}$  for all models of the sequence (Fig. 6.41). All curves show a stable value or at least a bend at this radius, which marks the end of this range.

For  $[M/H] \geq -3.0$ , the number density of dust particles decreases with the metallicity (Fig. 6.38). Below  $[M/H] = -3.0$  the temperature inversion zone reaches very deep (Fig. 6.31). The temperatures at this zone are too high to allow seed formation. Below this zone the steep drop of temperature enables the nucleation, as well as the growth (Figs. 6.36 and 6.39). Because the gas density is already very high at this range (Fig. 6.33), the nucleation process is very efficient, while the growth by  $\text{TiO}[s]$  remains negligible until its supersaturation is perceptibly larger than unity (Fig. 6.42). The first growth region is located much deeper in these models (Fig. 6.41). Therefore, the higher local densities result in a lower drift velocity and thus a stronger accumulation of the dust particles (Fig. 6.38).

The first growth region is shifted inwards and the number density of dust particles becomes smaller

with decreasing metallicity (Fig. 6.38). Thus, at similar pressure, the models show much less heating due to dust opacity (Fig. 6.31). While the local temperature rises perceptibly over the growth range at solar metallicity ( $10^0 \dots 10^2 \text{ dyn cm}^{-2}$ ), the local temperature even drops for  $[M/H] = -6.0$  ( $2 \cdot 10^3 \dots 1 \cdot 10^5 \text{ dyn cm}^{-2}$ ) and the heating by dust is no longer observed.

**3. Fine particle region:** For solar metallicity, the region of fine particles ranges over two orders of pressure (Fig. 6.41). In the models for  $[M/H] \leq -3.0$  this region has completely vanished. Only the bends in the mean grain size curves remain.

The lower edge of the fine particle region is defined by the maximum of the nucleation rate and the minimum in the local gas phase element abundances (Figs. 6.36 and 6.43).

The composition of the dust grains is not affected by the metallicity at this range (Fig. 6.44).

**4-6. Cloud deck, rain edge and cloud base:** Below the minimum of the gas phase element abundances (Fig. 6.43), the growth velocity starts to re-increase in all models (Fig. 6.39). The drop of the drift velocity ends and it remains almost stable (Fig. 6.35).

At the higher layers, the supersaturation ratios at similar pressures drop with the metallicity. At the cloud deck, this behaviour is inverted. A lower metallicity yields a higher supersaturation ratio (Fig. 6.42). The reason for this are the vanishing opacities of the dust and the molecules at this range (Fig. 6.34). The atmosphere is not as much heated. Thus, the local temperature decreases with the metallicity (Fig. 6.31). The chemical equilibrium balances towards a stronger formation of the reactants. In addition, the gas density increases with decreasing metallicity (Fig. 6.33).

The dust particle number density decreases by almost two order between solar metallicity and  $[M/H] = -3.5$  (Figs. 6.37 and 6.38). In the model for  $[M/H] = -4.0$ , the number density is at its minimum. For lower metallicities, the increasing supersaturation rate of  $\text{TiO}_2[s]$  is able to outbalance the decreasing concentration of  $\text{TiO}_2$  (Figs. 6.42 and 6.33). This causes a re-increasing nucleation rate (Fig. 6.36). As a result, the dust particle number density is increasing as well (Fig. 6.38). At  $[M/H] = -6.0$  a renewed decrease of the nucleation rate and dust particle number density is observed.

The maximum depletion of Ti becomes weaker below  $[M/H] = -2.0$ , i.e. the local gas phase abundance of Ti is higher than for models with a higher metallicity (Fig. 6.43). A local maximum of the abundance is reached around  $[M/H] = -3.5$  at approximately  $3 \cdot 10^5 \text{ dyn cm}^{-2}$ . The resulting high concentration of TiO causes a strong molecular opacity at this location, which increases the local temperature (Fig. 6.31). This feature in the temperature structure drifts slightly inwards with further decreasing metallicity and becomes weaker, because of the lower abundances (Fig. 6.43). Its disappearance in models of lower metallicities yields a lower local optical depth (Fig. 6.34).

At this bump in the temperature structure for  $[M/H] \leq -3.5$  the supersaturation of all dust species has a local minimum (Fig. 6.42). Still,  $\text{TiO}_2[s]$  remains highly supersaturated. Thus, the nucleation rate increases again, below this minimum (Fig. 6.36). As a result, the local dust particle number density starts to rise again for  $[M/H] \leq -3.5$  (Fig. 6.38). The influence of the local minima in the supersaturation rates is not perceptible in the growth of the dust grains.

The first maximum of the mean grain size, which is related to the Mg-bearing dust species, is  $0.6 \mu\text{m}$  for solar metallicity and increases to almost  $1.8 \mu\text{m}$  for  $[M/H] = -3.5$  (Figs. 6.40 and 6.41). For lower metallicities this maximum drops again, with a value of  $0.06 \mu\text{m}$  for  $[M/H] = -6.0$ . The mean grain composition at this maximum is not affected by metallicities of  $[M/H] \geq -3.5$ . For lower metallicities, the Si-bearing dust species ( $\text{SiO}_2$ ,  $\text{MgSiO}_3$ ,  $\text{Mg}_2\text{SiO}_4$ ) become negligible at this range (Fig. 6.44). The composition settles at 70% MgO and 30% Fe for  $[M/H] \leq -5.0$ . The

reason for this is likely a shift of the chemical equilibrium at the low local temperatures of these models.

Models with  $[M/H] \leq -3.5$ , feature a local minimum in the mean grain size below  $10^6 \text{ dyn cm}^{-2}$  (Fig. 6.41). This is due to the fact, that nucleation still takes place at these pressures (Fig. 6.36), resulting in many small grains (Fig. 6.38), while the supersaturation rates of all dust species are already in a steep drop (Fig. 6.42). Hence, the growth is too weak to balance the mean grain size. This is also the cause for the emerging secondary minimum in the gas phase abundances of the considered elements.

Similar to the lower edge of the fine particle range, the mean grain radius starts to increase again after the nucleation rate has reached a maximum (Figs. 6.41 and 6.36). This is the case at approximately  $2 \cdot 10^6 \text{ dyn cm}^{-2}$ . Below, the rising gas density and the improving element replenishment, due to the proximity to the convection zone (Figs. 6.32, 6.35 and 6.41), increase the growth velocity, while the number of newly forming dust seeds becomes negligible (Fig. 6.36). The minimum in the mean grain size has led to a decreasing drift velocity (Fig. 6.35). As a result, the mean grain radius increases (Fig. 6.41), even though the supersaturation ratios of all dust species approach unity (Fig. 6.42).

As soon as the supersaturation rates of the species drop below unity, the growth ceases (Fig. 6.42).  $\text{MgO}[s]$  evaporates at an almost constant pressure value of  $4 \cdot 10^6 \text{ dyn cm}^{-2}$ , for  $[M/H] \leq -3.5$  (Fig. 6.44). The two maxima of the mean grain radius, for these models are thus both dominated by  $\text{MgO}[s]$  and  $\text{Fe}[s]$ .

$\text{Fe}[s]$  evaporates slightly deeper than the Mg-bearing species. This causes a maximum in the Fe volume fraction (Fig. 6.44). This maximum shifts inwards from  $[M/H] = +0.3$  to  $-3.5$ . For lower metallicities, this maximum remains at  $6 \cdot 10^6 \text{ dyn cm}^{-2}$ . This maximum is barely perceptible in the mean grain radius for solar metallicities, because of the much stronger  $\text{Al}_2\text{O}_3[s]$  maximum (Fig. 6.40). However, this has already changed for  $[M/H] = -1.0$ , where the second maximum in the mean grain radius is predominantly caused by  $\text{Fe}[s]$ . For  $[M/H] \leq -4.5$ , the maximum in the  $\text{Fe}[s]$  volume fraction decreases. In these models, the high volume fraction of almost 80% of  $\text{Fe}[s]$  is no longer due to the strong growth by  $\text{Fe}[s]$ , but the strong evaporation of  $\text{MgO}[s]$ . Because of this, there is no longer a perceptible maximum in the mean grain radius, which could be identified with  $\text{Fe}[s]$ .

The maximum in the mean grain size, which is dominated by  $\text{Al}_2\text{O}_3[s]$ , becomes less important with decreasing metallicity (Figs. 6.40 and (Fig. 6.44)). The maximum volume fraction of  $\text{Al}_2\text{O}_3[s]$  drops from above 90% for  $[M/H] = +0.3$  to 15% for  $[M/H] = -3.5$ . For lower metallicities, this maximum volume fraction remains at 15%. Below  $[M/H] = -1.0$  there is no longer an efficient growth of  $\text{Al}_2\text{O}_3[s]$ . The maximum volume fraction is much more due to the earlier evaporation of the other dust species.

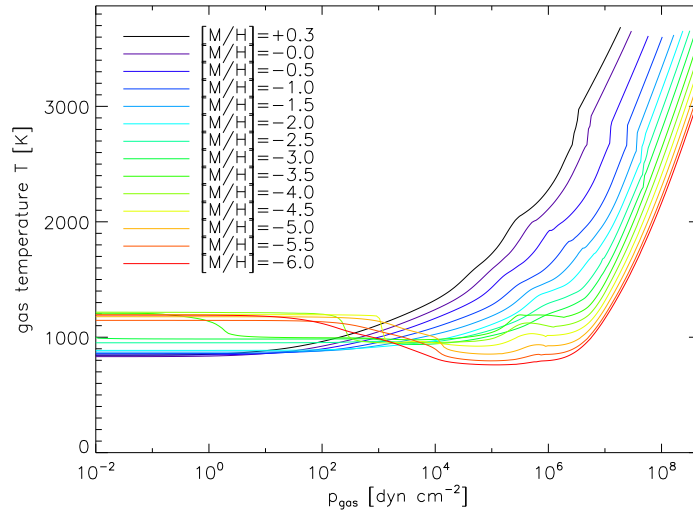
The accumulation of dust particles between the rain edge and the cloud base is only present in the models with  $[M/H] \geq -2.0$  (Fig. 6.37). For lower metallicities, the steep temperature gradient pushes all the supersaturation ratios almost instantly below unity (Fig. 6.42). The result is an extremely efficient evaporation and a fast drop of the dust particle number density.

One final noteworthy aspect remains for the description of the mean grain size of this sequence. Between  $[M/H] = -3.5$  and  $-4.0$ , iron is still supersaturated at the edge of the convection zone (Figs. 6.42 and 6.32). The dust cloud dips into the convection zone. Close to and within the convection zone, the element replenishment is most efficient. This is amplified by the high gas density (Fig. 6.33). The growth velocity of the dust particles rises to almost  $1 \mu\text{m s}^{-1}$  (Fig. 6.39). The result is another maximum in the mean grain size (Fig. 6.40). The maximum mean grain radius

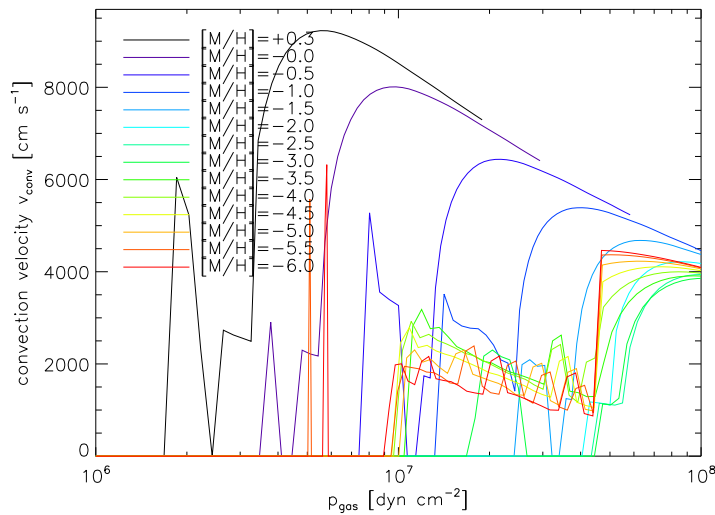
## 6. Model sequences

is  $26\mu\text{m}$  for  $[M/H] = -3.5$  and  $9\mu\text{m}$  for  $[M/H] = -4.0$ .

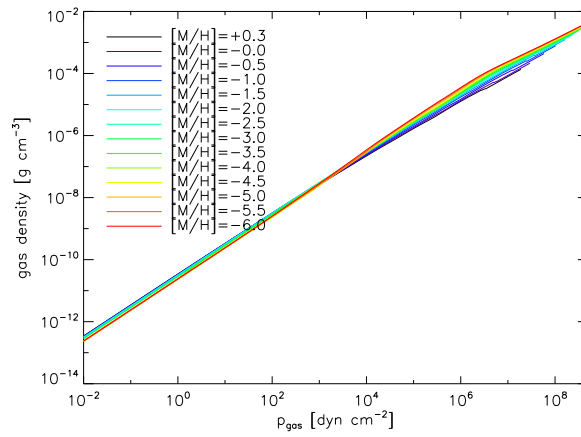
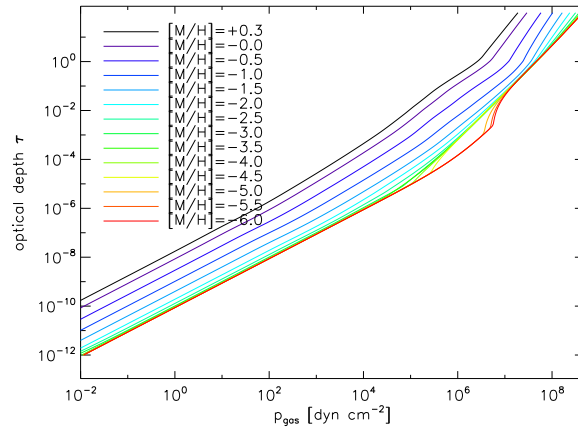
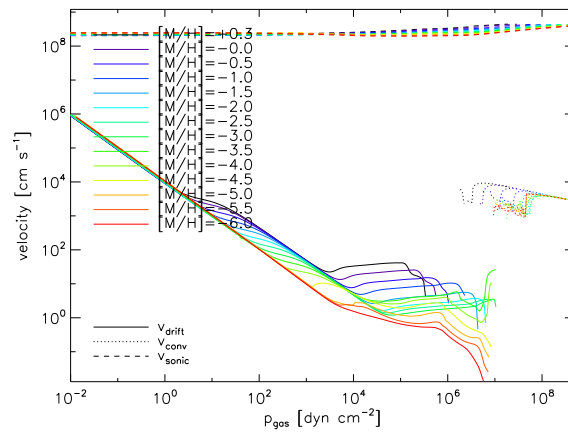
This region causes two problems concerning the model assumptions. The first is the large grain size, for which the free molecular flow may no longer be a suitable description (see Sec. 2.2). The second is the gas velocity, which can not be neglected, so close to or even within the convection zone. Fortunately, the number density of the particles is low at the cloud base, because of their high drift velocity and the low metallicity of the models. Thus, these particles are not dense enough to be a perceptible opacity source.



**Figure 6.31.:** Temperature  $T$



**Figure 6.32.:** Convection velocity  $v_{\text{conv}}$

Figure 6.33.: Gas density  $\rho$ Figure 6.34.: Optical depth  $\tau$  at  $1.2 \mu\text{m}$ Figure 6.35.: Mean drift velocity  $v_{\text{drift}}$  (solid), sonic velocity  $v_s$  (dashed), convection velocity  $v_{\text{conv}}$  (dotted)

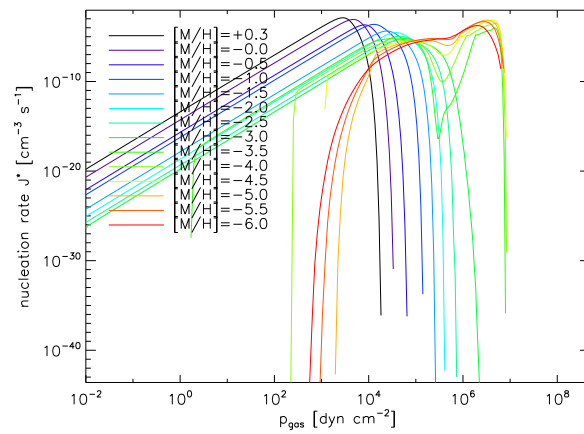


Figure 6.36.: Nucleation rate  $J^*$

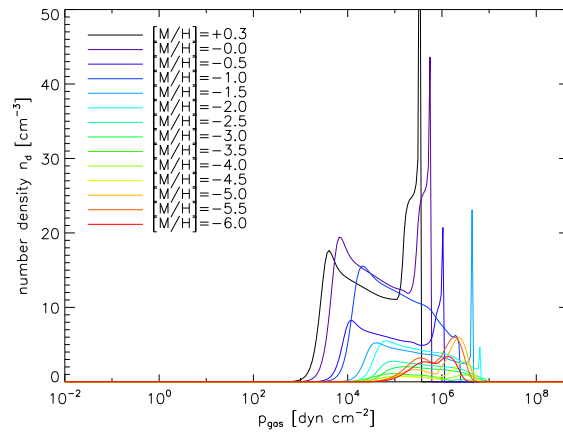


Figure 6.37.: Number density of dust particles  $n_d$  (linear scale)

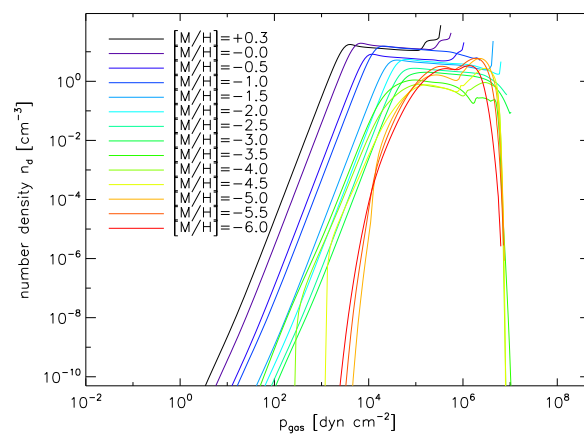


Figure 6.38.: Number density of dust particles  $n_d$  (logarithmic scale)

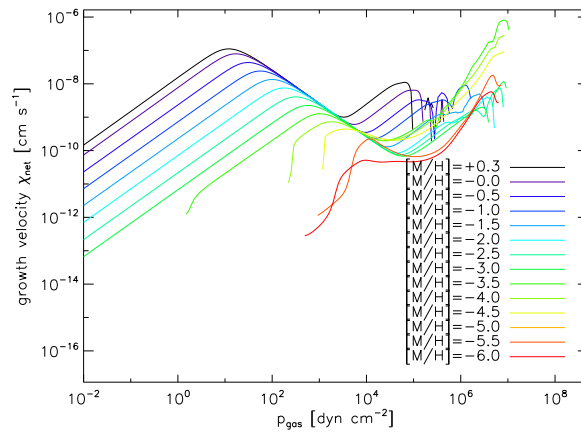


Figure 6.39.: Growth velocity  $\chi_{\text{net}}$

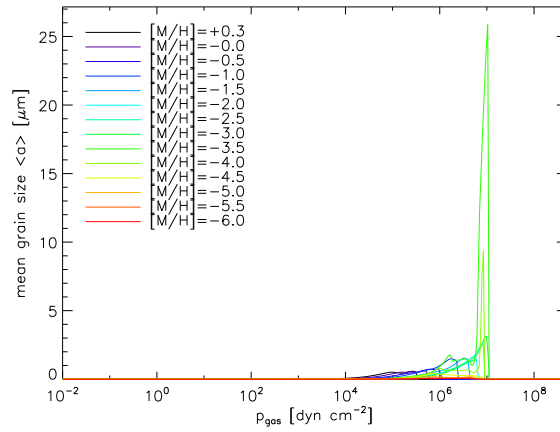


Figure 6.40.: Mean particle radius  $\langle a \rangle$  (linear scale)

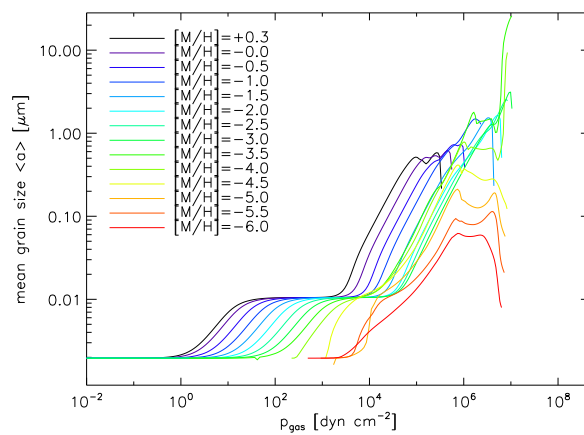


Figure 6.41.: Mean particle radius  $\langle a \rangle$  (logarithmic scale)

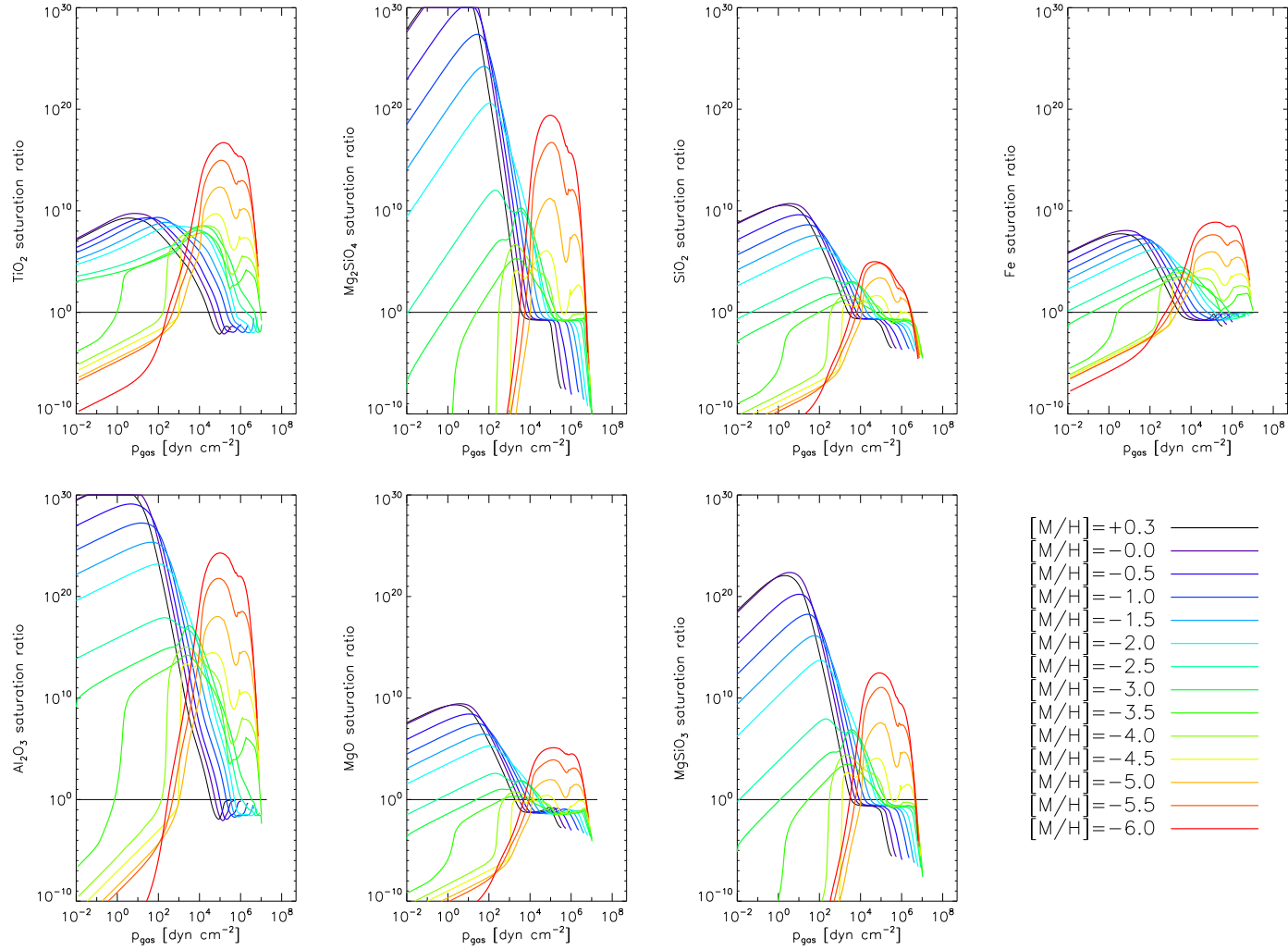
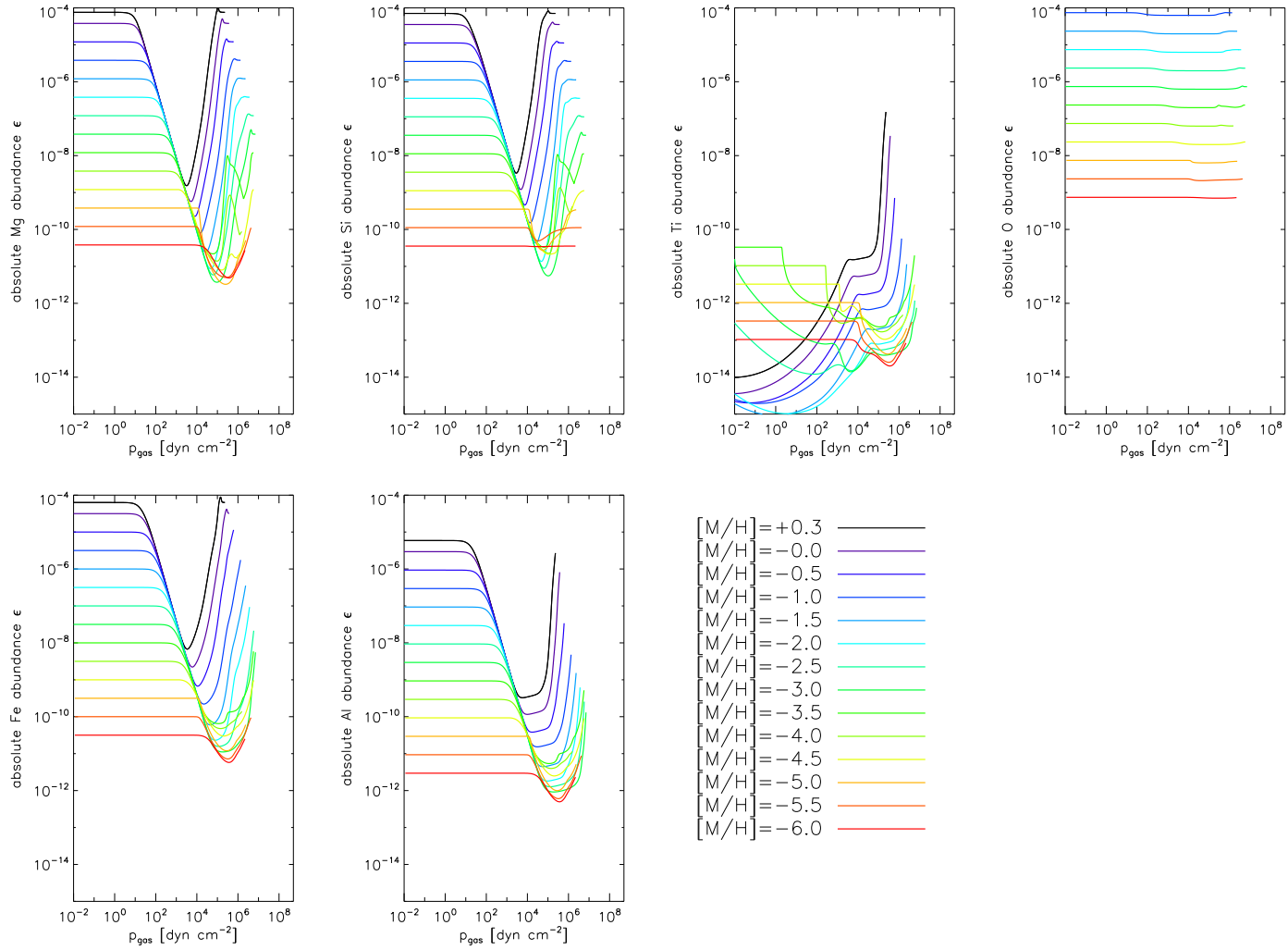
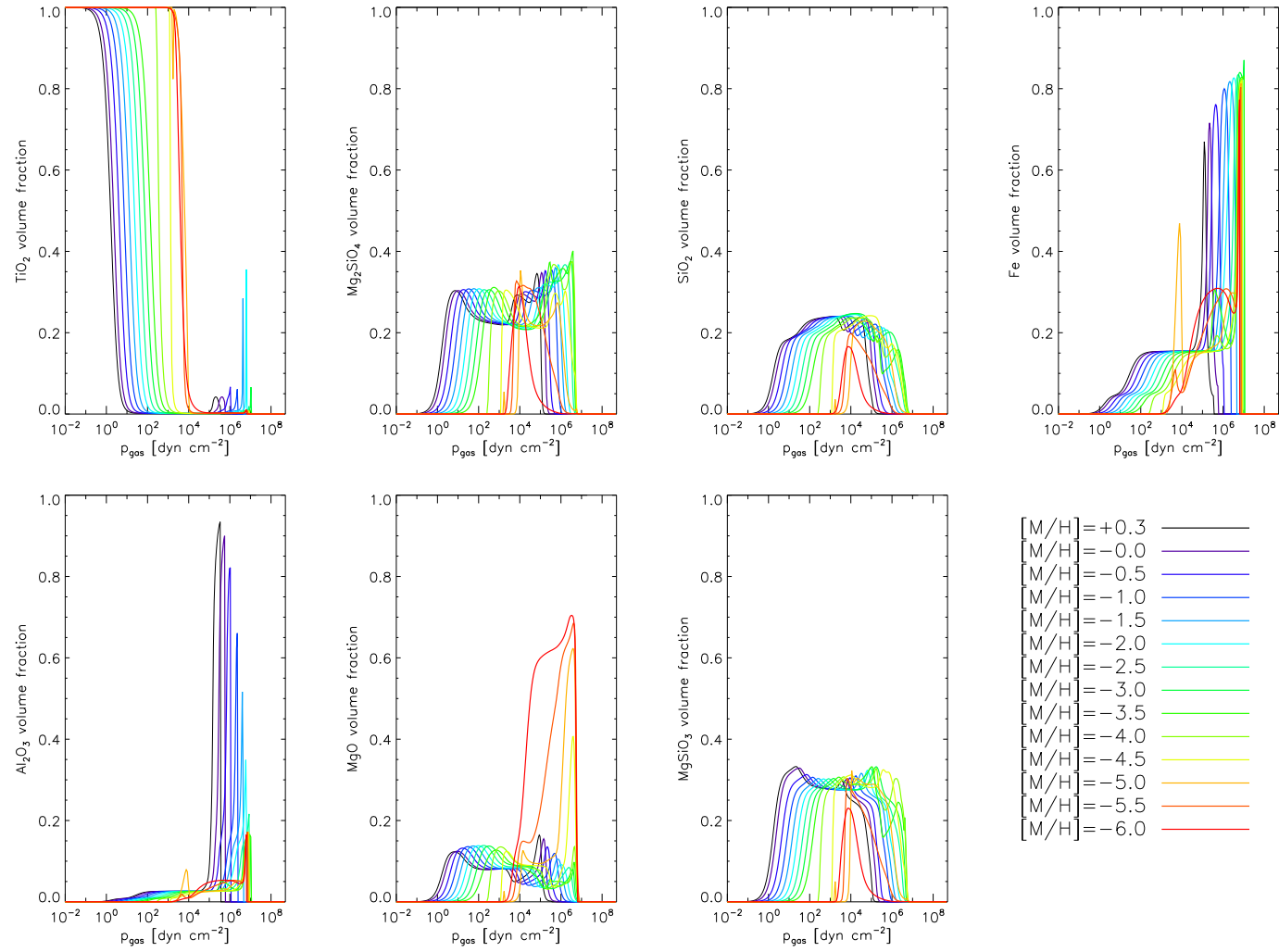


Figure 6.42.: Effective supersaturation rates  $S_{\text{eff}}^s$  of the seven dust species  $s$



**Figure 6.43.:** Absolute gas phase abundances  $\epsilon_i$  of the six considered elements



**Figure 6.44.:** Mean grain volume fractions  $V_s/V_{\text{tot}}$  of the seven considered dust species  $s$

## 6.5. Spectra

In order to give examples of the evolution of the spectra over the sequences, the wavelength range between  $0.5$  and  $2.5\mu\text{m}$  is shown in Figs. 6.45 - 6.47. As a compromise between clarity and details, not all spectra of the sequences are shown. Around  $1.4\mu\text{m}$  and  $1.9\mu\text{m}$  there are water bands in the spectra. Beyond  $2.3\mu\text{m}$  there is a CO band (Leggett et al. (2002)). The strong absorption lines between  $0.5$  and  $0.9\mu\text{m}$  correspond to atomic lines of alkali elements.

The dust cloud represents a strong continuum opacity at the considered wavelength. Lower atmosphere layers are blanked out. Thus, spectral features which originate from these layers become weaker. The element depletion caused by the dust formation weakens those features which are caused by the corresponding elements or the molecules which include them.

As anticipated, the spectra become more blue with increasing effective temperature (Fig. 6.45). The mentioned molecular bands become stronger, while the alkali lines become weaker.

An increased surface gravity yields stronger alkali lines (Fig. 6.46). Below  $0.9\mu\text{m}$  the flux increases over the sequence. The flux between  $0.9$  to  $1.7\mu\text{m}$  shows a maximum for  $\log(g) = 4.0$  which corresponds to the observed minimum in the dust particle number density. The flux beyond  $1.7\mu\text{m}$  decreases and the respective  $\text{H}_2\text{O}$  and CO bands become weaker over the sequence.

As expected, all absorption features weaken with decreasing metallicity (Fig. 6.47). The remaining shape of the spectra is caused by the temperature structure. Due to the decreased opacities, the observed flux originates from deeper and thus hotter layers of the atmosphere. Hence, the spectra become more blue.

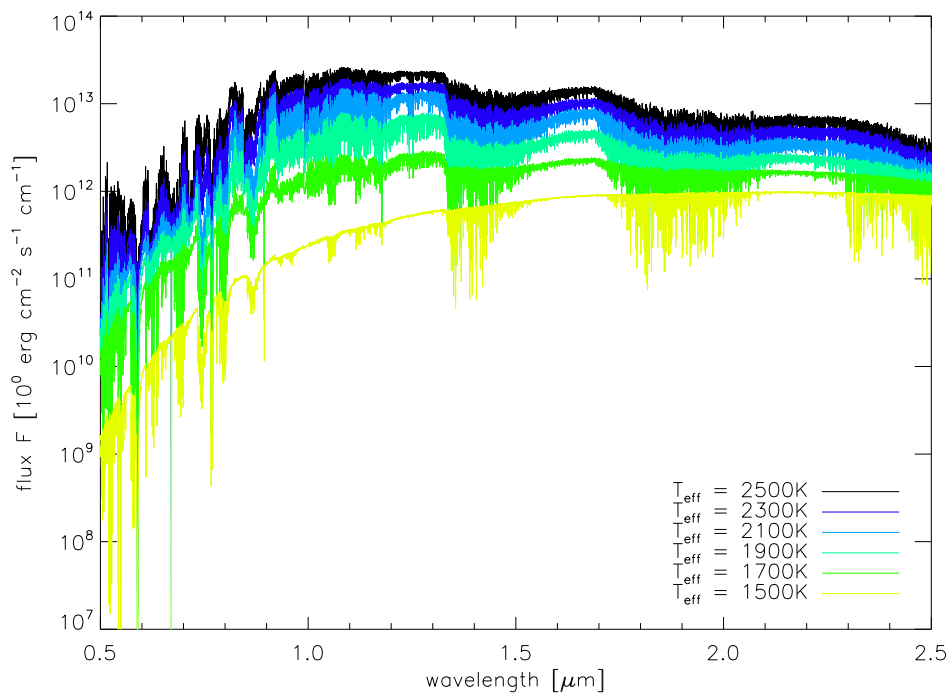


**Figure 6.45.:** Spectra of the temperature sequence

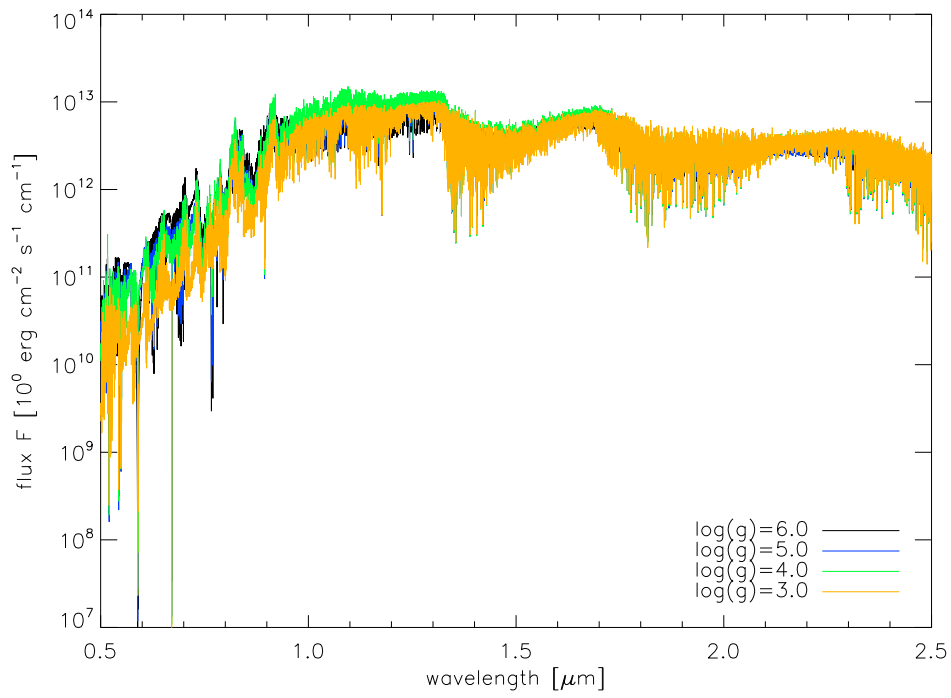


**Figure 6.46.:** Spectra of the gravity sequence

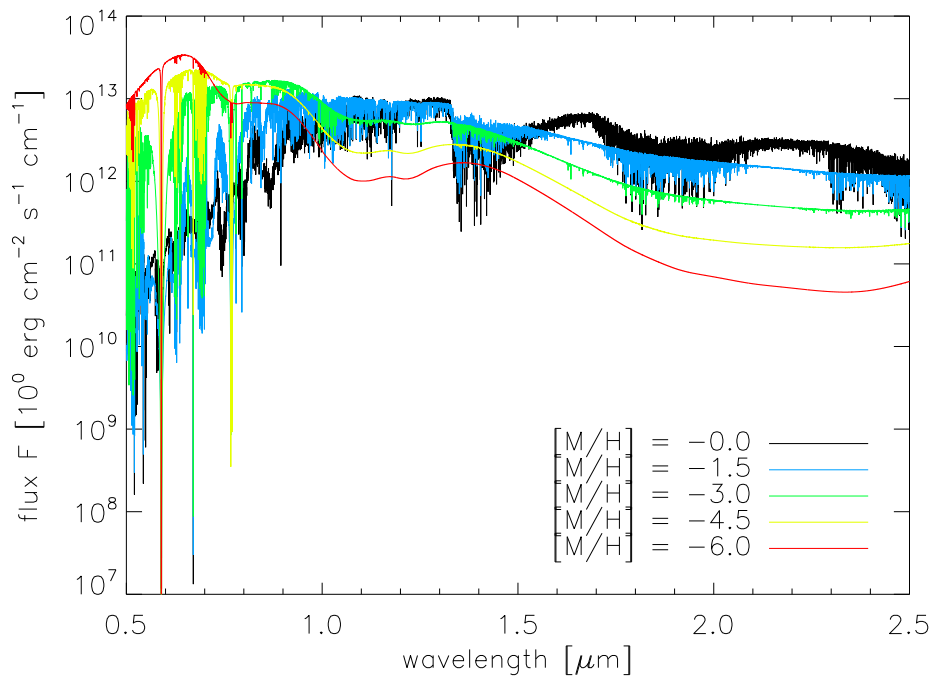


**Figure 6.47.:** Spectra of the metallicity sequence

## 6.6. Conclusions

Except for extremely low metallicities, there is a stable dust cloud structure which appears in all models irrespective of their model parameters. Only the location and width of the individual cloud ranges is affected.

Due to the strong supersaturation and the similarities in the atmosphere conditions over the sequences, the mean grain size remains unaltered in the cloud structure above the cloud deck. A reduction of the metallicity by  $\Delta[M/H] = 1.0$  or an increase of the surface gravity by  $\Delta \log(g) = 1.0$  relocates this range to a gas pressure which is 0.5 orders of magnitude higher. The effective temperature has a negligible influence on the mean grain size above the cloud.

The number density of dust particles at this range becomes lower with decreasing effective temperature, increasing surface gravity or decreasing metallicity. This is caused by the stronger depletion of Ti at the outer atmosphere for lower effective temperatures and the lower supersaturation of  $\text{TiO}_2[s]$  for higher surface gravity and lower metallicities.

For even lower metallicities ( $[M/H] \leq -3.5$ ) the mean grain size and the number density curves are no longer simply shifted to higher pressures, but are disrupted by the appearance of a temperature inversion zone.

The onset of efficient growth and the maximum of the number density mark the upper edge of the dust cloud. This edge is shifted to a lower pressure for a lower effective temperature, a lower surface gravity or a higher metallicity.

The deeper the dust cloud is located, the higher the maximum dust particle number density rises, because of the exponential increase of the nucleation rate. The result is a higher maximum number density for lower effective temperatures, higher surface gravities and higher metallicities.

The relative location of the maxima of the mean grain size, due to the growth and evaporation of the seven dust species, is also influenced by the gas pressure. If the dust cloud is located at higher pressures, the maxima are less well distinguishable on a logarithmic pressure scale. As the first maximum is shifted inwards, its value increases. This higher value leads to a stronger dust opacity, which is the cause of an increased temperature gradient. As a result, the subsequent maxima of the remaining dust species become less important and even start to vanish. Thus, the composition of dust grains is influenced by the the gas pressure at the dust cloud. The volume fraction of  $\text{Al}_2\text{O}_3[s]$  becomes weaker with increasing pressure at the cloud deck and thus with a lower effective temperature, higher surface gravity and lower metallicity. The contrary happens to the volume fraction of iron, which increases with a higher pressure at this cloud range.

The mentioned increase of the temperature gradient for higher gas pressures is amplified by high dust particle number densities. This becomes especially significant for low effective temperatures. Here, the thick dust cloud causes a bump in the temperature structure (backwarming) at approximately  $10^6 \text{ dyn cm}^{-2}$ , which represents a stable lower boundary of the dust cloud. As a result, the extension of the cloud decreases, because the upper boundary is shifted to higher pressures with decreasing effective temperature. This is compensated by the rising particle number density, which maintains the optical thickness of the cloud.

The maximum mean grain radius decreases slightly with decreasing effective temperature, decreasing surface gravity and increasing metallicity, excepting models for the extremely low metallicities. Neglecting models with  $[M/H] \leq -1.0$  the maximum mean grain size remains of the order of  $0.6 \mu\text{m}$ .

At extreme metallicities ( $[M/H] \leq -3.5$ ), the structure of the grain size distribution and the particle composition become totally different, because the dust cloud is enclosed within a minimum in

the temperature structure. In these models, nucleation takes place at the whole dust cloud, with a minimum at the location of the minimum Ti abundance. This maximum also causes a bump in the temperature structure. Around  $[M/H] = -3.5$  the dust cloud dips into the convection zone, which sparks a short, renewed growth.

At the evaporation edges of the dust species, the abundance of the considered elements is increased above the nominal value given by the metallicity. The mean grain size at the evaporation edges is less strongly dependent on the model parameters than the particle number density. Thus simplified, the enrichment of elements at the evaporation edges becomes stronger for higher dust particle number densities. Another influence is the width of the evaporation range. This enrichment of the considered elements intensifies the corresponding absorption lines.

## 7. Comparison with observations

Dehn (2007) contains a comparison between synthetic spectra, calculated with DRIFT-PHOENIX4, and a near-infrared observation of DENIS J0205-1159 by Reid et al. (2001).

DENIS J0205-1159 is a binary of identical dwarfs (Leggett et al. (2001)), which was discovered by Delfosse et al. (1997), who classified it as late L type. Most earlier estimates of the effective temperature of the dwarfs (e.g., Dahn et al. (2002)) yielded values around  $T_{\text{eff}} \approx 1600\text{K}$ . In contrast, the DRIFT spectra by Dehn (2007) and the DUSTY spectra by Leggett et al. (2001) produced a best fit for  $T_{\text{eff}} = 1800\text{K}$  and  $T_{\text{eff}} = 1900\text{K}$ , respectively.

In this chapter, the results for a repeated fit with the improved DRIFT-PHOENIX version are shown. A comparison between the two DRIFT versions for the best fit model parameters obtained by Dehn (2007) is shown in Fig. 7.1. The flux below  $1.3\mu\text{m}$  and around  $1.6\mu\text{m}$  is lower for the newer model, while it is slightly higher in the  $\text{H}_2\text{O}$  and  $\text{CO}$  bands.

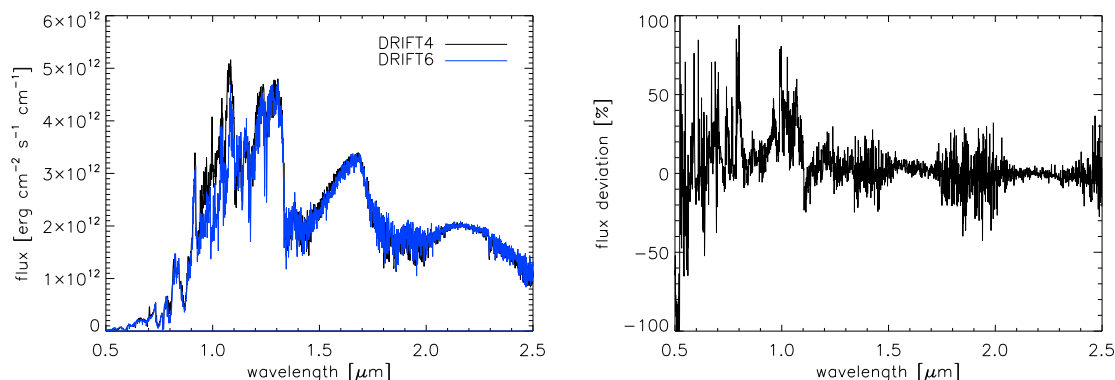


**Figure 7.1.:** Comparison between DRIFT4 and DRIFT6 spectra ( $T_{\text{eff}} = 1800\text{K}$ ,  $\log(g) = 5.0$ ,  $[M/H] = 0.0$ ); *left:* Both spectra, *right:* Relative flux change between the spectra

The result is a better fit, which can be seen by comparing Figs. 7.2 and 7.3. The improvement is especially large below  $1.3\mu\text{m}$ . However, the flux between the molecular bands remains too low. The shape of the DENIS J0205-1159 spectrum around  $1.6\mu\text{m}$  and  $2.2\mu\text{m}$  is still not fully reproduced in the synthetic spectra. This can be improved by variation of the model parameters. Fig. 7.4 shows a fit with a model of lower metallicity of  $[M/H] = -0.5$ . Though there is no perceptible improvement around  $2.2\mu\text{m}$ , the spectral shape around  $1.6\mu\text{m}$  is much better reproduced. Unfortunately, a consequence of the decreased metallicity is a higher flux below  $1.3\mu\text{m}$ . However, this could be undone by an improved treatment of alkali line profiles. As it was shown in Johnas (2007) and Johnas et al. (2008), this causes a lower flux at the considered range. Therefore, a combination of DRIFT and the improved line profiles will yield better results.

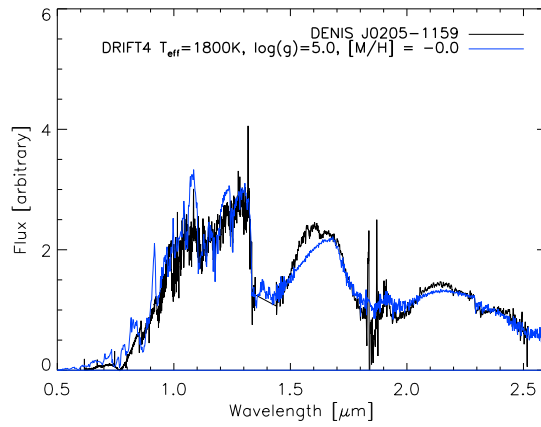


**Figure 7.2.:** Fit with a DRIFT4 model by Dehn (2007)

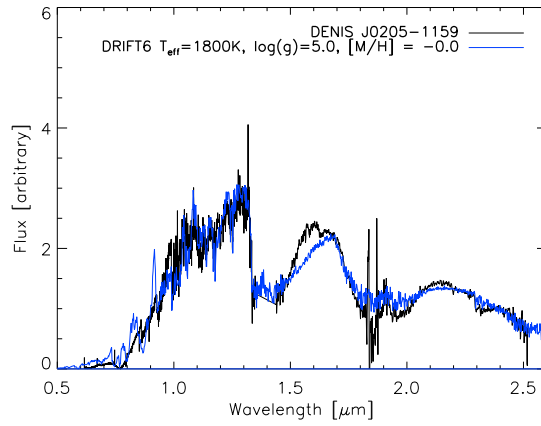


**Figure 7.3.:** New fit with a DRIFT6 model

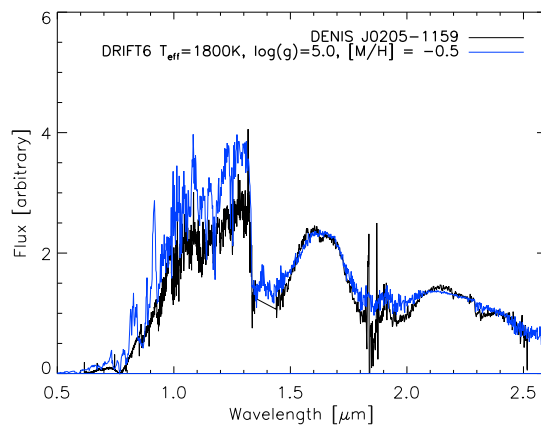


**Figure 7.4.:** New fit with a DRIFT6 model of lower metallicity

## 8. Summary and outlook

The goal of this work was to investigate the evolution of dust clouds in brown dwarf atmospheres with different effective temperatures, surface gravities and metallicities. In order to do so, several upgrades to the code had to be done. The latest version of DRIFT-PHOENIX runs much more stable than before and is slightly faster.

With this new version, one model sequence for each of the mentioned three parameters was calculated ( $T_{\text{eff}} = 1500 \dots 2500\text{K}$ ,  $\log(g) = 3.0 \dots 6.0$ ,  $[M/H] = -6.0 \dots +0.3$ ). The following observations were made: The dust cloud is located at a higher pressure for lower effective temperatures, higher surface gravities and lower metallicities. The maximum number density of the dust particles increases exponentially with increasing values of these three model parameters. The observed maximum number densities range between 0.2 and several hundred particles per cubic centimeter. The maximum grain radius is hardly influenced by the surface gravity ( $\langle a \rangle \approx 0.6\mu\text{m}$ ), but increases with the effective temperature ( $\langle a \rangle \approx 0.5 - 0.9\mu\text{m}$ ). The grain size increases for the lowest considered metallicities, reaches a maximum for  $[M/H] = -3.5$  and slowly decreases for higher metallicities.

At the outer range of the dust cloud, the mean composition of the dust grains is hardly influenced by any of the three model parameters, except for extremely low metallicities. However, this changes at the innermost range of the cloud. Here, higher effective temperatures, lower surface gravities and higher metallicities yield stronger maxima of the  $\text{Al}_2\text{O}_3$  volume fraction, while the volume fraction of Fe becomes weaker.

The backwarming caused by the dust cloud leads to the formation of a stable lower boundary for the lowest considered effective temperatures. At this boundary, the dust particle number density is increasing with decreasing effective temperature, while the mean grain radius is decreasing. Thus, this lower cloud boundary appears to be especially promising for future investigations.

For lower metallicities there is a temperature inversion zone at low pressures. It prohibits the formation of dust seeds. Therefore, the atmosphere is still undepleted at the edge of this zone, which is the cause for the very high supersaturation ratios and the resulting strong nucleation rates and strong growth. Thus, the dust cloud loses the structure, which has been observed in all other models. Though the lowest considered metallicity values appear to be exaggerated, these models give an impression of how a temperature inversion affects the dust cloud. This is of special interest, since more and more large exoplanets are detected, which are strongly irradiated by their host stars. In models for metallicities around  $[M/H] = -3.5$ , the dust cloud dips into the convection zone, which has a huge influence on the mean grain size. The resulting particles reach a mean radius of  $\langle a \rangle > 25\mu\text{m}$ . The reliability of these results will have to be investigated.

An additional part of this work was the repetition of the fit of DENIS J0205-1159 done by Dehn (2007). The recent DRIFT-PHOENIX version improves the fit, but a more proper treatment of the alkali line broadening (Johnas (2007)) is required, in order to gain better results below  $1\mu\text{m}$ .

The analysis of the model sequences of this work will have to be expanded to a whole model grid, in order to get a better understanding of the dust formation in brown dwarfs and to finally analyze

actual observations.

At the moment, the grain size distribution function  $f$  consists of only two sample grain sizes and their respective number densities. A more continuous treatment is likely going to stabilize the combined dust and atmosphere models and improve the results of spectral fits.

Convection, including the overshoot mechanism is a crucial point of the dust model. As it was already suggested by Dehn (2007), the applied treatment of the mixing should be verified. It is still not known whether the overshoot parameter  $\beta$ , which has an enormous influence on the dust, is a constant or depends on the local thermodynamic quantities.

The overshoot itself is only considered in DRIFT but it is so far neglected in PHOENIX. Therefore, the influence of the overshoot on the atmosphere structure should be investigated.

The granulation of the convection zone might also have an important influence on the dust formation, as it yields strongly varied thermodynamic gas properties above the convection zone edge. There is a host of possible approaches for this, ranging from simple statistics over time-dependent modelling to 3D simulations. However, convection is still not well understood and there are no direct observations to which the results could be compared.



## A. Kinetic model for dust formation

The problem of the nucleation and the subsequent growth and evaporation applies the dust moment method developed by Gail & Sedlmayr (1988), and Dominik et al. (1993). Woitke & Helling (2003), Helling & Woitke (2006) and Helling et al. (2008b) extended this method to treat the nucleation, growth and evaporation consistently coupled to gravitational settling and convective overshooting. Simultaneously, equations for element conservation had to be derived which also take into account all these effects.

The starting point for the derivation is the grain size distribution. The associated function  $f(V)[\text{cm}^{-6}]$  represents the number of dust grains within a grain volume interval inside a selected volume element. Thus, it is a function of the grain size and depends on the location in the atmosphere. The grain volume interval  $dV$  exchanges grains with adjacent volume intervals via surface reactions. For every surface reaction  $r$ , four terms are needed in order to describe the population of interval  $dV$  through growth  $R_{\uparrow}$  and evaporation  $R_{\downarrow}$  and the depopulation of  $dV$  through growth  $R^{\uparrow}$  and evaporation  $R_{\downarrow}$  (Fig. A.1).

In the case of subsonic free molecular flow around grains of the radius  $a$ , these functions are given by (Woitke & Helling (2003)):

$$R^{\uparrow} = \sum_r f(V)dV A_{\text{tot}}(V) n_r v_r^{\text{rel}} \alpha_r \quad (\text{A.1})$$

$$R_{\uparrow} = \sum_r f(V - \Delta V_r) dV A_{\text{tot}}(V - \Delta V_r) n_r v_r^{\text{rel}} \alpha_r \quad (\text{A.2})$$

$$R_{\downarrow} = \sum_r f(V + \Delta V_r) dV A_s(V + \Delta V_r) \beta_r(V + \Delta V_r) \quad (\text{A.3})$$

$$R_{\downarrow} = \sum_r f(V) dV A_s(V) \beta_r(V), \quad (\text{A.4})$$

where  $V$  denotes the dust grain volume,  $\Delta V_r$  the volume increment per surface reaction of type  $r$ ,  $A_{\text{tot}}$  the grain surface,  $A_s$  the total surface of all islands of solid species  $s$ ,  $n_r$  the concentration of the key educt of reaction  $r$ ,  $\alpha_r$  is the respective sticking coefficient and  $v_r^{\text{rel}}$  the relative velocity of the grain and the reactant. The number of absorbed key molecules is the maximum number of possible surface reactions and thus limits the reaction rate. The evaporation rate coefficients  $\beta_r$  are derived from a phase equilibrium reference state (see Helling & Woitke (2006)).

Additionally, the grain size distribution depends on the flow of dust particles into and out of the observed volume element. This follows from the transformation:

$$\frac{df(V)}{dt} = \frac{\partial f}{\partial t} + \frac{1}{r^2} \nabla \cdot (r^2 [\vec{v}_{\text{gas}} + \vec{v}_{\text{drift}}(V)] f(V)). \quad (\text{A.5})$$

It is possible to set up a conservation equation for the grain size distribution function:

$$\frac{\partial}{\partial t} (f(V) dV) + \nabla \cdot ([\vec{v}_{\text{gas}} + \vec{v}_{\text{drift}}(V)] f(V) dV) = (R_{\uparrow} + R_{\downarrow} - R^{\uparrow} - R_{\downarrow}) dV. \quad (\text{A.6})$$

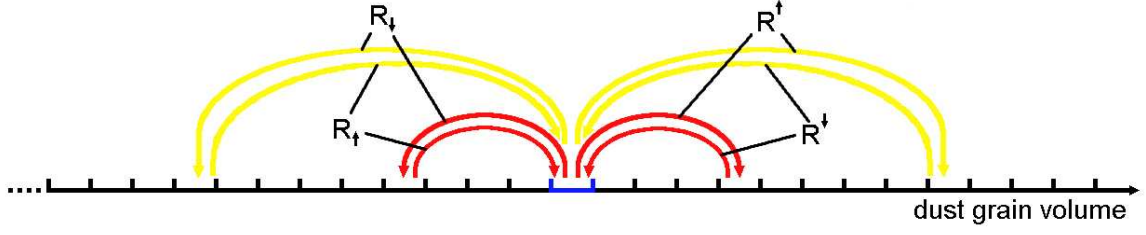


**Figure A.1.:** Corresponding to the grain size distribution function  $f$ , every grain volume interval is filled by a number of dust grains. The considered interval exchanges grains with other intervals, depending on the dust species. The total grain exchange is given by the functions  $R$ .

This equation needs to be solved for any possible grain size volume and any location, if the development of dust throughout the atmosphere and its effect on the spectrum is to be investigated. In order to avoid this time-consuming approach, several simplifications need to be applied, of which the first one is the use of mean dust properties. Therefore, Eq. A.6 is multiplied by  $V^{j/3}$  ( $j = 0, 1, 2, \dots$ ) and integrated over the grain volume. The lower integration limit is arbitrarily defined as 1000 times the volume of a  $\text{TiO}_2$ -monomer. The moments of the grain size distribution function  $L_j$  are introduced:

$$\rho L_j(x, t) = \int_{V_l}^{\infty} f(V, x, t) V^{j/3} dV \quad [\text{cm}^{j-3}] \quad j = 0, 1, 2, \dots \quad (\text{A.7})$$

Disregarding any conversion factors,  $V^{1/3}$  represents the dust grain radius for spherical particles,  $V^{2/3}$  the grain surface and so forth. Integration over the distribution function multiplied by these quantities yields the total values for the considered space volume element. For example, the zeroth moment  $L_0$  is simply the total number of dust particles, while the first moment  $L_1$  represents the total of all grain radii in  $dV$ . Thus, mean dust properties can be determined by regarding conversion factors and by dividing the other moments  $L_{j \neq 0}$  by the zeroth moment. The resulting mean properties are the number density  $n_d$

$$n_d = \rho L_0 \quad [\text{cm}^{-3}], \quad (\text{A.8})$$

the mean grain radius  $\langle a \rangle$

$$\langle a \rangle = \sqrt[3]{\frac{3}{4\pi} \frac{L_1}{L_0}} \quad [\text{cm}], \quad (\text{A.9})$$

the mean dust grain surface  $\langle A \rangle$

$$\langle A \rangle = \sqrt[3]{36\pi} \frac{L_2}{L_0} \quad [\text{cm}^2] \quad (\text{A.10})$$

and the mean dust particle volume  $\langle V \rangle$

$$\langle V \rangle = \frac{L_3}{L_0} \quad [\text{cm}^3]. \quad (\text{A.11})$$

Furthermore a characteristic growth speed of the mean grain radius

$$\chi_{\text{net}} = \sqrt[3]{36\pi} \sum_r \frac{\Delta V_r n_r v_r^{\text{rel}} \alpha_r}{\nu_r^{\text{key}}} \left( 1 - \frac{1}{S_r b_{\text{surf}}^s} \right) \quad [\text{cm} \cdot \text{s}^{-1}] \quad (\text{A.12})$$

and a characteristic gravitational acceleration

$$\xi = \left( \frac{3}{4\pi} \right)^{1/3} \frac{\sqrt{\pi}}{2} g \quad [\text{cm} \cdot \text{s}^{-2}] \quad (\text{A.13})$$

are defined. The summation in Eq. A.12 is over to all considered surface reactions  $r$ . The inverse surface fraction is defined by  $b_{\text{surf}}^s = A_{\text{tot}}/A_s \approx V_{\text{tot}}/V_s$ .<sup>1</sup> The stoichiometric coefficient of the key educt of the reaction  $r$  is denoted as  $\nu_r^{\text{key}}$ .  $S_r$  represents the supersaturation ratio of the key educt of surface reaction  $r$ . Utilizing Eqs. A.7, A.12 and A.13 and the nucleation rate  $J^* = J(V_l) = f(V_l) \frac{dV}{dt} |_{V=V_l}$  in Eq. (A.6) results in the dust moment equations:

$$\frac{\partial}{\partial t} (\rho L_j) + \nabla (v_{\text{gas}} \rho L_j) = V_l^{j/3} J^* + \frac{j}{3} \chi_{\text{net}} \rho L_{j-1} + \xi \nabla \left( \frac{\rho_d}{c_T} L_{j+1} \vec{e}_r \right). \quad (\text{A.14})$$

So far this system of differential equations only describes the mean dust properties, but the element depletion caused by the nucleation and the dust grain growth must also be considered. Therefore, the following conservation equation needs to be satisfied for every element  $i$  considered in the model:

$$\begin{aligned} \frac{\partial}{\partial t} (n_{<H>} \epsilon_i) + \nabla (v_{\text{gas}} n_{<H>} \epsilon_i) = \\ -\nu_{i,0} N_l J^* - \sqrt[3]{36\pi} \rho L_2 \sum_r \frac{\nu_{i,s} n_r v_r^{\text{rel}} \alpha_r}{\nu_r^{\text{key}}} \left( 1 - \frac{1}{S_r b_{\text{surf}}^s} \right) \end{aligned} \quad (\text{A.15})$$

The stoichiometric coefficients for homogeneous nucleation and for the growth of a dust species  $s$  are  $\nu_{i,0}$  and  $\nu_{i,s}$  respectively. The element abundances  $\epsilon_i$  are given relative to the local concentration of hydrogen  $n_{<H>}$ .

The model which is applied in DRIFT-PHOENIX is designed to describe a quasi-static atmosphere in plane-parallel geometry. These simplifications<sup>2</sup> are applied in the next step:

$$V_l^{j/3} J^* + \frac{j}{3} \chi_{\text{net}} \rho L_{j-1} + \xi \frac{d}{dz} \left( \frac{L_{j+1}}{c_T} \right) = 0 \quad (\text{A.16})$$

$$\nu_{i,0} N_l J^* + \sqrt[3]{36\pi} \rho L_2 \sum_r \nu_{i,r} n_r v_r^{\text{rel}} \alpha_r \left( 1 - \frac{1}{S_r b_{\text{surf}}^s} \right) = 0. \quad (\text{A.17})$$

This system of equations only has the trivial solution  $L_j = 0$  for  $S_r \leq 1$  (Woitke & Helling (2004)). This is the case because convective overshooting has not yet been included. The nucleation and growth processes consume elements permanently and thus decrease their supersaturation, until no more dust seeds are formed. All dust particles settle and the contained material vanishes from the upper atmosphere, resulting in a quasi-static state.

<sup>1</sup>The approximation  $A_{\text{tot}}/A_s \approx V_{\text{tot}}/V_s$  is only valid for a homogenous distribution of the solid islands in the dust grains.

<sup>2</sup> $\frac{\partial}{\partial t} = 0$  and  $\nabla = \frac{d}{dz}$

The convective overshoot leads to an additional term in the two equation sets (Eqs. A.16, A.17):

$$-\frac{d}{dz} \left( \frac{\rho_d}{c_T} L_{j+1} \right) = \frac{1}{\xi} \left( -\frac{\rho L_j}{\tau_{\text{mix}}} + V_l^{j/3} J^* + \frac{j}{3} \chi_{\text{net}} \rho L_{j-1} \right) \quad (\text{A.18})$$

$$\frac{n_{<H>}(\epsilon_i^0 - \epsilon_i)}{\tau_{\text{mix}}} = \nu_{i,0} N_l J^* + \sqrt[3]{36\pi} \rho L_2 \sum_r \nu_{i,r} n_r v_r^{\text{rel}} \alpha_r \left( 1 - \frac{1}{S_r b_{\text{surf}}^s} \right), \quad (\text{A.19})$$

with  $\epsilon_i^0$  being the initial model abundance of elements and  $\epsilon_i$  the actual abundance in the considered volume.

For calculations of dust opacities, it is important to keep track of the volume fractions of dust species within a grain. This can be done by replacing the third dust moment equation (Eq. A.18,  $j = 3$ ) with a set of similar equations for the individual dust species (Helling et al. (2008b)):

$$-\frac{d}{dz} \left( \frac{\rho_d}{c_T} L_4^s \right) = \frac{1}{\xi} \left( -\frac{\rho L_3^s}{\tau_{\text{mix}}} + V_l^s J^* + \chi_{\text{net}}^s \rho L_2 \right) \quad (\text{A.20})$$

It can be avoided to solve the original third dust moment equation, because of the following relations:

$$\sum_s L_3^s = L_3 \quad \sum_s L_4^s = L_4 \quad \sum_s \chi_{\text{net}}^s = \chi_{\text{net}} \quad \sum_s V_l^s = V_l. \quad (\text{A.21})$$

Before this system of equations (A.18-A.20) can be solved, one last problem needs to be addressed. For an arbitrary set of consecutive dust moment equations, there is always one more dust moment included than there are equations. In this model the moments  $L_1$ ,  $L_2$ ,  $L_3$  and  $L_4^s$  are determined. Thus, the closure condition  $L_0 = L_0(L_1, L_2, L_3, L_4^s)$  must be found.

Therefore, a new set of dust moments  $K_j = (3/4\pi)^{j/3} \rho L_j$  in the radius space is introduced and a corresponding grain size distribution function  $f(a)$  is found (Dominik et al. (1993)). As four dust moments are determined by the first three dust moment equations, it is possible to set up a function of four free coefficients for  $L_0$ . The definition featured in this model is a superposition of Dirac-functions (Helling et al. (2008b)):

$$f(a) = N_1 \delta(a - a_1) + N_2 \delta(a - a_2) \quad (\text{A.22})$$

The resulting dust moments are  $K_j = N_1 a_1^j + N_2 a_2^j$ . These definitions allow the determination of the two grain sizes  $a_1$ ,  $a_2$  and their respective number densities  $N_1$  and  $N_2$ . Now that a grain size distribution function is known, the zeroth dust moment is:

$$L_0 = N_1 + N_2 \quad (\text{A.23})$$

Finally the dust moments can be determined as solution of the final equation system (Eqs. A.18, A.19, A.20, A.23). For more details on the determination of the grain size distribution function  $f$  see Appendix A in Helling et al. (2008b).

## B. Implementation

This chapter is addressed to PHOENIX developers. The first sections describe the upgrades of the code, while the added or modified namelist parameters are listed in the last section. The results of the individual upgrades are summarized in Sec. 4.

### `static_weather6`

DRIFT-PHOENIX regularly suffered from convergence problems in the element conservation of `static_weather`. This usually resulted in an abort of the program in the equilibrium chemistry (error message: '\*\*\* keine Konvergenz in SMCHEM!'). To address this problem the dust routine was upgraded to version 6.

Most subroutines of the dust routine have not been altered between versions 4 and 6 (see Figs. B.1, B.2 and B.6).

The convergence problem of DRIFT-PHOENIX4 is related to the element conservation in `static_weather4`. Therefore, the respective subroutine, called `STATIC_EPS`, has been largely modified. Version 6 of the routine is streamlined compared to version 4 (compare Figs. B.3 and B.4 to Fig. B.5) and is much more reliable. The new subroutine `PULLBACK` replaces the older routines `FDJAC`, `FMIN`, `LNSRCH`, `LUBKSB`, `LUDCMP`, `NEWT` and `NUMJAC`. After a Newton-Raphson step has been determined, `PULLBACK` checks, whether this step improves the quality of the approximation. If this is the case, the step is accepted. Otherwise the stepsize is reduced until an improvement emerges.

The new `static_weather` version has an increased tolerance for the differential equation solver, speeding up the calculations by sacrificing quality. If required, this can be undone by decreasing the variable `tol` in the `static_weather` routine.

For clarity the global variables of `static_weather` are shifted to the new `drift_data` module. The structure of `static_weather` is shown in Figs. B.1-B.6. A list of the `static_weather6` subroutines is given in Tab. B.1.

Due to the important improvements, all previous versions of `static_weather` are obsolete. Therefore, they were removed from the new DRIFT-PHOENIX version. The namelist parameter `driftSWversion` has not been removed, but is of no relevance at present.

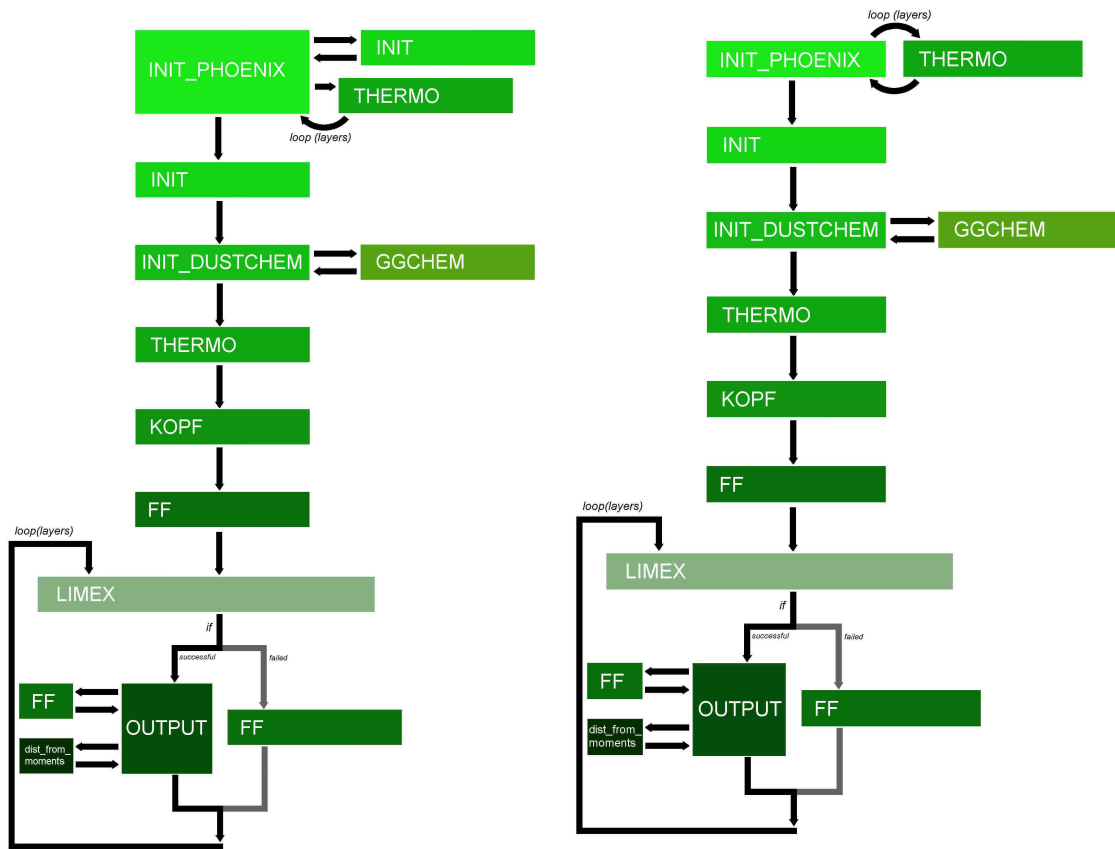


**Figure B.1.:** Flow charts for `static_weather4` (left) and `static_weather6` (right)

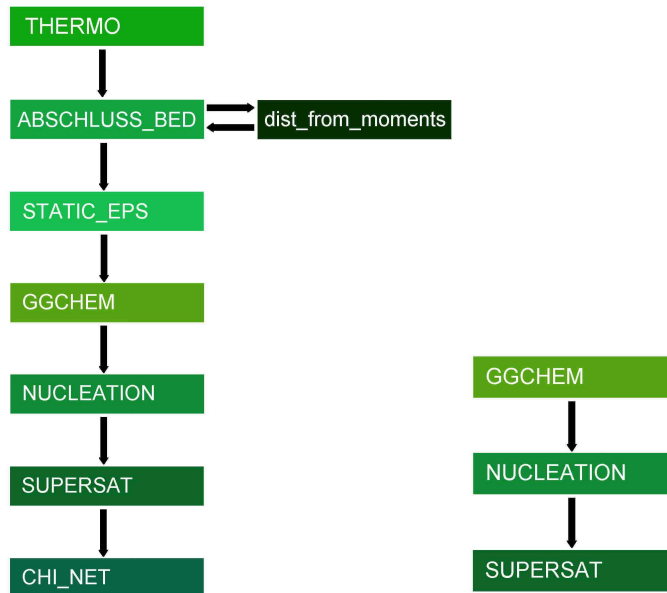


**Figure B.2.:** Flow charts for subroutines `FF` (left) and `ELFUNK` (right) for both versions

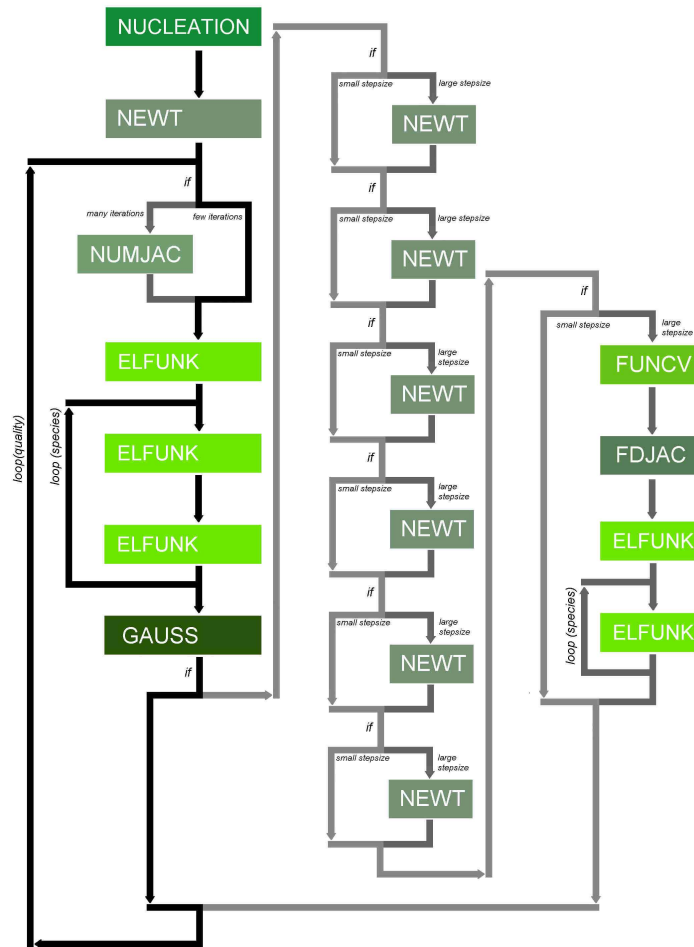


Figure B.3.: Flow chart for subroutine STATIC\_EPS (static\_weather4)

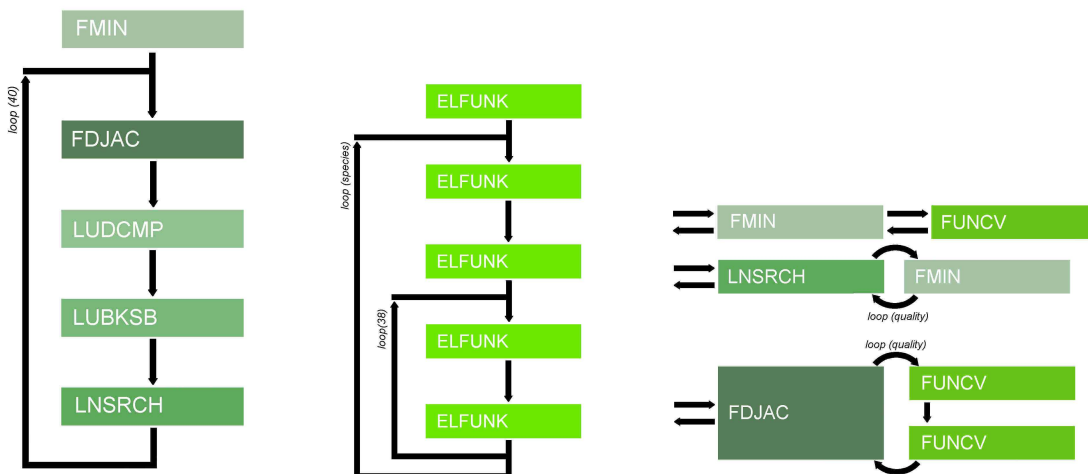
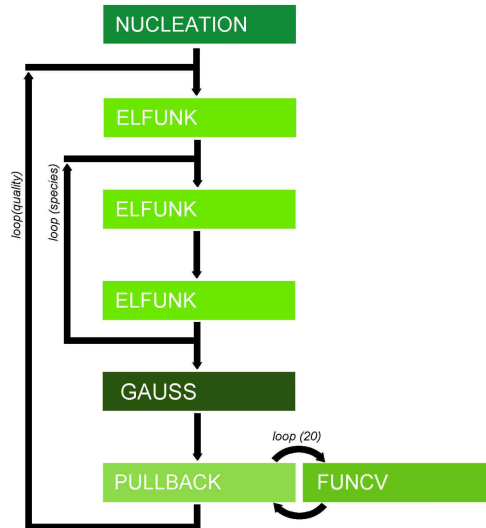
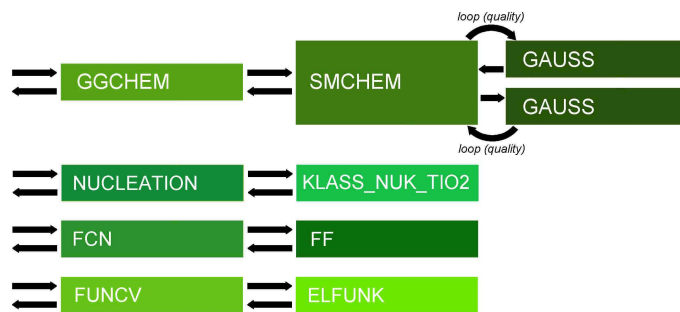


Figure B.4.: Flow charts for subroutines NEWT (left), NUMJAC (middle) and additional subroutines (right) (static\_weather4)



**Figure B.5.:** Flow charts for subroutine `STATIC_EPS` (`static_weather6`)



**Figure B.6.:** Flow charts for the remaining subroutines of both versions

subroutine	task
<code>static_weather</code>	main routine
<code>INIT_PHOENIX</code>	read the atmosphere structure and calculates the mixing time scale
<code>THERMO</code>	interpolation of atmosphere properties
<code>INIT</code>	initialization of solar element abundance values and element masses
<code>INIT_DUSTCHEM</code>	initialization of the dust chemistry
<code>GGCHEM</code>	wrapper function for <code>SMCHEM</code>
<code>SMCHEM</code>	calculation of the equilibrium chemistry
<code>GAUSS</code>	solves a given linear equation system
<code>KOPF</code>	open output files and write headers
<code>FF</code>	interpolation of the atmosphere structure, calculation of dust properties
<code>ABSCHLUSS_BED</code>	determination of a closure condition
<code>dist_from_moments</code>	determine a grain size distribution from the dust moments
<code>STATIC_EPS</code>	root finding for the element conservation
<code>ELFUNK</code>	determination of element consumption
<code>PULLBACK</code>	improvement of the Newton-Raphson stepsize for the element conservation
<code>FUNCV</code>	wrapper function for <code>ELFUNK</code>
<code>NUCLEATION</code>	wrapper function for <code>KLASS_NUK_TIO2</code>
<code>KLASS_NUK_TIO2</code>	calculation of the nucleation rate
<code>SUPERSAT</code>	determination of supersaturation ratios
<code>CHI_NET</code>	calculation of the growth velocity
<code>LIMEX</code>	solver for the differential equation system
<code>OUTPUT</code>	determine and write output
<code>FCN</code>	wrapper function for <code>FF</code>

**Table B.1.:** List of `static_weather6` subroutines

## ema3

The original effective medium function `ema` by Dehn (2007) did not verify the determined solution for the refractive index. As it was shown in Sec. 4.2, a verification is required. In order to approach this, the function `ema3` (by courtesy of P. Voitke) was included to replace `ema`. The function `ema` has not been erased from the code, but remains as alternative. `ema3` was assigned as the default function. Its structure is shown in Fig. B.7. The contained subroutines are listed in Tab. B.2.

For given volume fractions, `ema3` first determines all required initial guesses for the solution of Eq. 2.26. Then, `EMA_FUNC` is called, to determine the quality of the guess and to determine the right side of Eq. 2.26 for variations of the guess. These varied guesses are used to determine a Newton-Raphson step with the `GAUSS` routine. The stepsize is varied by `EMA_PULLBACK`, until the step improves the quality of the new guess. After 30 iterations, the physical validity of the result is checked. Correct solutions are passed to `readDrift`, while another initial guess is tried, if the determined solution is unphysical.

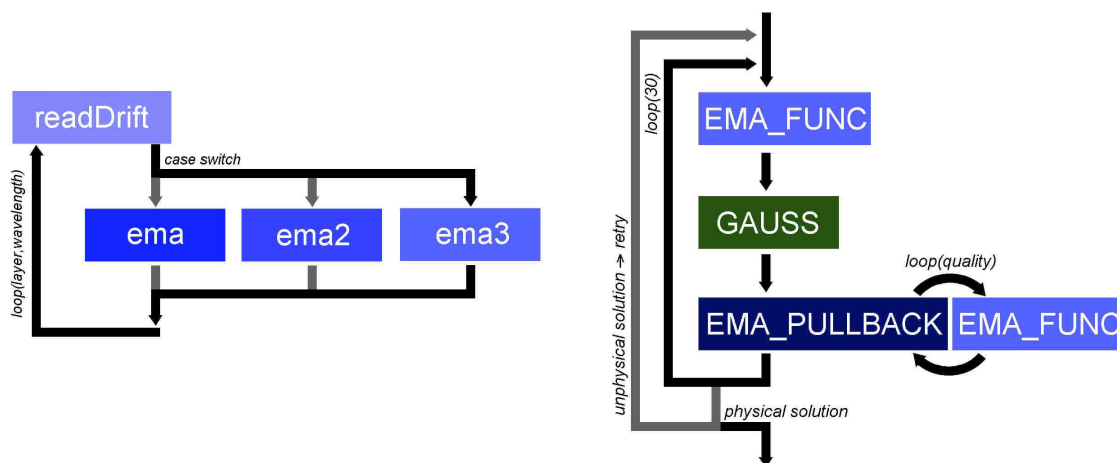


**Figure B.7.:** Flow charts for the `readDrift` (left) and `ema3` (right)

subroutine	task
<code>readDrift</code>	read <code>static_weather</code> output
<code>ema</code>	old effective medium function (Dehn)
<code>ema2</code>	effective medium function (alternate) (Dehn)
<code>ema3</code>	new effective medium function (Voitke)
<code>EMA_FUNC</code>	calculate right side of Eq. 2.26
<code>GAUSS</code>	solves a given linear equation system
<code>EMA_PULLBACK</code>	improve Newton-Raphson step

**Table B.2.:** List of `readDrift` and `ema3` subroutines

## MieApprox

The dust opacities, calculated by the routine `miex`, feature strong variations for small changes in the given mean grain size. In order to stabilize the results, the routine `MieApprox` was added (Fig. B.8). Instead of calling the Mie calculation routine `shexqnn2` directly from `miex` and only once for a given grain size, `MieApprox` is interposed. It generates a set of 11 logarithmically equidistant adjacent grain sizes per sample size before calling `shexqnn2` for this whole set. The resulting opacities are averaged.

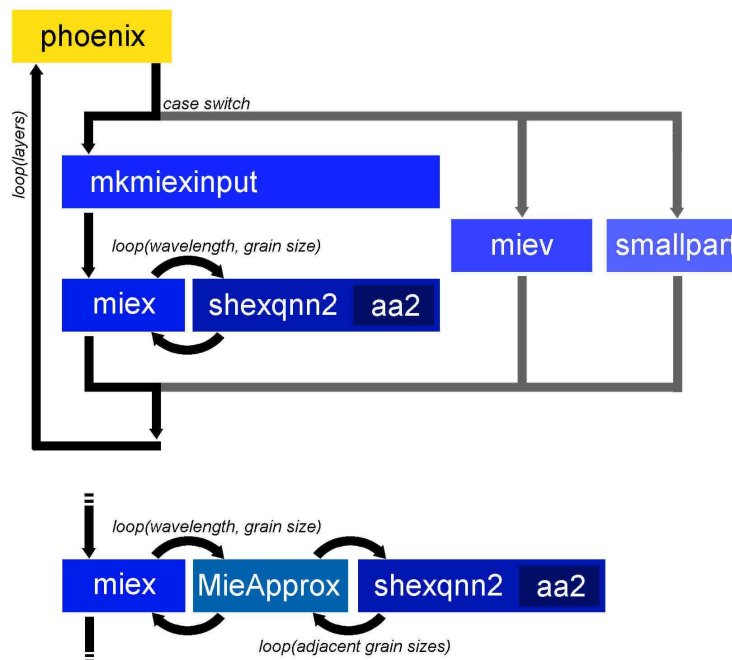


**Figure B.8.:** Flow chart of the original Mie calculations and the upgrade with `MieApprox`

subroutine	task
<code>mkmiexinput</code>	write input for one atmosphere layer
<code>miex</code>	main Mie routine (Wolf)
<code>MieApprox</code>	smoothing of <code>shexqnn2</code> results
<code>shexqnn2</code>	calculate scattering and absorption cross sections for given grain radius and refractive index
<code>aa2</code>	calculate the ratio of the derivate to the function for Bessel functions
<code>miev</code>	alternate Mie routine (Wiscombe)
<code>smallpart</code>	alternate Mie routine (small particle limit)

**Table B.3.:** List of Mie subroutines

---

## hydroSWloop

The loop, described in Sec. 4.4, is included directly into `phoenix.f`. It starts at the point, at which the altered abundances are read for the hydrostatics, and ends after `static_weather` was executed. The loop counter is reset at the beginning of every new temperature iteration step. Every temperature iteration, the loop is per default executed twice. If `DRIFT` is not used, the loop is also deactivated. The lines, related to the loop, can be found by looking for the string `SWloop`.

## driftCR

Since oscillations turned out to be a prevalent obstacle for the convergence of `DRIFT-PHOENIX` models, a tool to distinguish a slow convergence from oscillations was needed. The new routine `driftCR`, which is called between the `hydroSWloop` and the dust opacity calculations by `mieX`, produces the new output file `convergence.report`. For every iteration the most important atmosphere and dust properties for all considered atmospheric layers are written into this file. Consequently, all iteration of a model can be compared, the convergence behavior displayed and any oscillation easily identified. This output was required, in order to produce the plots, shown in Sec. 5.

## Namelist parameters

A list of namelist parameters, which are used for the `DRIFT` module is appended to Dehn (2007). As new versions for the dust routine and the effective medium function, as well as a new configuration of the Mie routine have been added, the respective parameters need to be updated. Two new parameters have been added for the `hydroSWloop`. A switch was added for the output routine `driftCR`.

variable	type	default value	description
<code>driftSWversion</code>	integer	7	7: <code>static_weather6</code>
<code>driftEMT</code>	integer	5	0-3: <code>ema</code> (see Dehn (2007)) 4: <code>ema2</code> (Dehn) 5: <code>ema3</code> (Woitke)
<code>driftMieType</code>	integer	3	0: <code>smallpart</code> 1: <code>MIEX</code> (Wolf) 2: <code>MIEV</code> (Wiscombe) 3: <code>MIEX + MieApprox</code>
<code>driftUseHydroSWloop</code>	logical	true	true: use <code>hydroSWloop</code>
<code>driftHydroSWloopmax</code>	integer	2	number of loop passes per temperature iteration
<code>driftReport</code>	logical	false	true: write <code>convergence.report</code> output file

**Table B.4.:** Parameters in the `PHOENIX` namelist.

# Index

- DRIFT-PHOENIX, 16
- DRIFT, 17
- PHOENIX, 17
- static\_weather, 16
  
- absolute abundance, 31
  
- backwarming, 9
  
- convection velocity  $v_{\text{conv}}$ , 8
- convective overshoot, 12
  
- drift velocity  $v_{\text{drift}}$ , 12
- dust moments  $L_j$ , 76
- dust particle number density  $n_d$ , 76
- dust seed, 10
- dust species, 9
  
- effective medium, 13
  
- flux, 6
  
- grain size distribution function  $f$ , 75
- growth velocity  $\chi_{\text{net}}$ , 77
  
- key species, 10
  
- layer flip, 29
- local thermodynamic equilibrium (LTE), 4
  
- mean grain size  $\langle a \rangle$ , 76
- metallicity, 5
  
- nucleation, 10
- nucleation rate  $J^*$ , 10
  
- opacity, 6, 15
- optical depth  $\tau$ , 6
- oscillation, 19
  
- Schwarzschild criterion, 8
  
- solid islands, 10
- subsonic free molecular flow, 9
- supersaturation ratio  $S_r$ , 11
- surface reaction, 10
  
- volume fraction  $\frac{V_s}{V_{\text{tot}}}$ , 13

# Bibliography

- Allard, F. and Hauschildt, P. H. (1995). *ApJ*, 445:433–450.
- Allard, F., Hauschildt, P. H., Alexander, D. R. and Starrfield, S. (1997). *ARA&A*, 35:137–177.
- Allard, F., Hauschildt, P. H., Alexander, D. R., Tamanai, A. and Schweitzer, A. (2001). *ApJ*, 556:357–372.
- Aspnes, D. E., Theeten, J. B. and Hottier, F. (1979). *Phys. Rev. B*, 20(8):3292–3302.
- Baron, E., Hauschildt, P. H., Allard, F., Lentz, E. J., Aufdenberg, J., Schweitzer, A. and Barman, T. (2003). In *Modelling of Stellar Atmospheres*, volume 210 of *IAU Symposium*, pages 19–+.
- Basri, G. (2000). *ARA&A*, 38:485–519.
- Becklin, E. E. and Zuckerman, B. (1988). *Nature*, 336:656–658.
- Béjar, V. J. S., Martín, E. L., Zapatero Osorio, M. R., Rebolo, R., Barrado y Navascués, D., Bailer-Jones, C. A. L., Mundt, R., Baraffe, I., Chabrier, C. and Allard, F. (2001). *ApJ*, 556:830–836.
- Biermann, L. (1932). *Zeitschrift für Astrophysik*, 5:117.
- Bosch, S., Ferre-Borrull, J., Leinfellner, N. and Canillas, A. (2000). *Surface Science*, 453:9–17(9).
- Bruggeman, D. A. G. (1935). *Annalen der Physik*, 24:636–664.
- Burgasser, A. J., Liebert, J., Kirkpatrick, J. D. and Gizis, J. E. (2002). *AJ*, 123:2744–2753.
- Cannon, C. J. (1973). *ApJ*, 185:621–630.
- Chabrier, G. and Baraffe, I. (2000). *ARA&A*, 38:337–377.
- Chabrier, G., Baraffe, I., Allard, F. and Hauschildt, P. H. (2005). *ArXiv e-prints*.
- Cooper, C. S., Sudarsky, D., Milsom, J. A., Lunine, J. I. and Burrows, A. (2003). *ApJ*, 586:1320–1337.
- Dahn, C. C., Harris, H. C., Vrba, F. J., Guetter, H. H., Canzian, B., Henden, A. A., Levine, S. E., Luginbuhl, C. B., Monet, A. K. B., Monet, D. G., Pier, J. R., Stone, R. C., Walker, R. L., Burgasser, A. J., Gizis, J. E., Kirkpatrick, J. D., Liebert, J. and Reid, I. N. (2002). *AJ*, 124:1170–1189.
- Debye, P. (1909). *Annalen der Physik*, 30:57–136.

- Dehn, M. (2007). Dissertation, Universität Hamburg.
- Delfosse, X., Tinney, C. G., Forveille, T., Epchtein, N., Bertin, E., Borsenberger, J., Copet, E., de Batz, B., Fouque, P., Kimeswenger, S., Le Bertre, T., Lacombe, F., Rouan, D. and Tiphene, D. (1997). *A&A*, 327:L25–L28.
- Dominik, C., Sedlmayr, E. and Gail, H.-P. (1993). *A&A*, 277:578–+.
- Ferguson, J. W., Alexander, D. R., Allard, F., Barman, T., Bodnarik, J. G., Hauschildt, P. H., Heffner-Wong, A. and Tamanai, A. (2005). *ApJ*, 623:585–596.
- Gail, H.-P., Keller, R. and Sedlmayr, E. (1984). *A&A*, 133:320–332.
- Gail, H.-P. and Sedlmayr, E. (1988). *A&A*, 206:153–168.
- Hauschildt, P. (1992). *Journal of Quantitative Spectroscopy and Radiative Transfer*, 47:433–453.
- Hauschildt, P. H., Barman, T., Baron, E. and Allard, F. (2003). In *Stellar Atmosphere Modeling*, volume 288 of *ASP Conference Series*, pages 227–+.
- Hauschildt, P. H. and Baron, E. (1999). *Journal of Computational and Applied Mathematics*, 109:41–63.
- Hauschildt, P. H. and Baron, E. (2006). *A&A*, 451:273–284.
- Hauschildt, P. H. and Baron, E. (2007). *PHOENIX version 15 (manual)*. <http://www.hs.uni-hamburg.de/EN/For/ThA/phoenix/Manual/Manual.pdf>.
- Hauschildt, P. H., Baron, E. and Allard, F. (1997). *ApJ*, 483:490–+.
- Hayashi, C. (1962). *Pub. A.S.J.*, 13:450–452.
- Hayashi, C. and Nakano, T. (1963). *Progress of Theoretical Physics*, 30:460–474.
- Helling, C. (2007). private communication.
- Helling, C., Ackerman, A., Allard, F., Dehn, M., Hauschildt, P., Homeier, D., Lodders, K., Marley, M., Rietmeijer, F., Tsuji, T. and Woitke, P. (2008a). *Comparison of cloud models for Brown Dwarfs*. (submitted).
- Helling, C. and Woitke, P. (2006). *A&A*, 455:325–338.
- Helling, C., Woitke, P. and Thi, W.-F. (2008b). *Dust in brown dwarfs. VI. Chemical composition and spectral appearance of quasi-static cloud layers*. (submitted).
- Johnas, C. M. S. (2007). Dissertation, Universität Hamburg.
- Johnas, C. M. S., Helling, C., Dehn, M., Woitke, P. and Hauschildt, P. H. (2008). *The Influence of Dust Formation Modelling on Na I and K I Line Profiles in Substellar Atmospheres*. (submitted).
- Kirkpatrick, J. D. (2005). *ARA&A*, 43:195–245.
- Kumar, S. S. (1963a). *ApJ*, 137:1126–+.

- Kumar, S. S. (1963b). *ApJ*, 137:1121–+.
- Leggett, S. K., Allard, F., Geballe, T. R., Hauschildt, P. H. and Schweitzer, A. (2001). *ApJ*, 548:908–918.
- Leggett, S. K., Golimowski, D. A., Fan, X., Geballe, T. R., Knapp, G. R., Brinkmann, J., Csabai, I., Gunn, J. E., Hawley, S. L., Henry, T. J., Hindsley, R., Ivezić, Ž., Lupton, R. H., Pier, J. R., Schneider, D. P., Smith, J. A., Strauss, M. A., Uomoto, A. and York, D. G. (2002). *ApJ*, 564:452–465.
- Ludwig, H.-G., Allard, F. and Hauschildt, P. H. (2002). *A&A*, 395:99–115.
- Mayor, M. and Queloz, D. (1995). *Nature*, 378:355–+.
- Mie, G. (1908). *Annalen der Physik*, 25:377.
- Mihalas, D. (1970). *Stellar Atmospheres*. San Francisco: Freeman, first edition.
- Mihalas, D. (1978). *Stellar Atmospheres*. San Francisco: Freeman, second edition.
- Nakajima, T., Oppenheimer, B. R., Kulkarni, S. R., Golimowski, D. A., Matthews, K. and Durrance, S. T. (1995). *Nature*, 378:463–+.
- Nolting, W. (2004). *Grundkurs Theoretische Physik 3: Elektrodynamik*. Springer, sixth edition.
- Prandtl, L. (1925). *Zeitschrift für angewandte Mathematik und Mechanik*, 5:136–139.
- Reid, I. N., Burgasser, A. J., Cruz, K. L., Kirkpatrick, J. D. and Gizis, J. E. (2001). *AJ*, 121:1710–1721.
- Rutten, R. J. (2003). *Radiative Transfer in Stellar Atmospheres*. Utrecht University lecture notes, eighth edition.
- Schneider, P. (2006). *Einführung in die Extragalaktische Astronomie und Kosmologie*. Springer, first edition.
- Tarter, J. C. (1975). Dissertation, AA(California Univ., Berkeley.).
- Tarter, J. C. (1976). In *Bulletin of the AAS*, volume 8 of *Bulletin of the AAS*.
- Unsöld, A. (1955). *Physik der Sternatmosphären, mit besonderer Berücksichtigung der Sonne*. Berlin: Springer, second edition.
- van de Hulst, H. C. (1957). *Light Scattering by Small Particles*. New York: Wiley, first edition.
- Whitworth, A. P. and Stamatellos, D. (2006). *A&A*, 458:817–829.
- Wiscombe, W. J. (1980). *Applied Optics*, 19:1505.
- Wiscombe, W. J. (1996). NCAR/TN-140+STR. Technical report, NCAR.
- Woitke, P. and Helling, C. (2003). *A&A*, 399:297–313.

Woitke, P. and Helling, C. (2004). *A&A*, 414:335–350.

Wolf, S. and Voshchinnikov, N. V. (2004). *Computer Physics Communications*, 162:113.



## Danksagung

Viele Personen haben auf die eine oder andere Weise ihren Teil zum Zustandekommen dieser Arbeit beigetragen. An dieser Stelle sei all diesen Menschen gedankt. Mein besonderer Dank gilt

Peter H. Hauschildt, für das spannende Thema, die unglaublich geduldige Beantwortung unzähliger Fragen und die angenehme Arbeitsatmosphäre in der Gruppe,

Christiane Helling und Peter Voitke, für die umfangreiche Hilfe beim Einstieg in das Thema, die angenehme Zusammenarbeit, die vielen hilfreichen Hinweise und Verbesserungen und die Eröffnung spannender Möglichkeiten für die Zukunft,

Matthias Dehn, für seine beeindruckende Vorarbeit, die gelegentlichen Ferndiagnosen, etwaige alte Datenschnipsel und nicht zu vergessen seinen Schreibtisch,

Christine M. S. Johnas, die mir bei allen erdenklichen Unklarheiten und Schwierigkeiten eine unschätzbare Hilfe war und deren Motivation hoffentlich langfristig auf mich abgefärbt hat,

Andreas Schweitzer, der trotz einer Flut von teils diffusen Fragen und einer Korrekturlesung dieser Arbeit sein Grinsen nicht verlernt hat,

den restlichen Mitgliedern meiner Arbeitsgruppe und allen aus meiner Haushälfte, da es niemandem von ihnen gelungen ist, meinen Fragen zu entgehen, und auch für die zahlreichen Diskussionen mit ihnen über Sinn und Unsinn der Welt,

sämtlichen weiteren Mitarbeitern an der Sternwarte, für die freundliche Aufnahme

und natürlich meiner Familie und Mella, ohne deren Fürsorge und Unterstützung ich es nicht bis hierher geschafft hätte.

“Alexander wept when he heard from Anaxarchos that there was an infinite number of worlds; and to his friends asking him if any accident had befallen him, he returned this answer: Do you not think it a matter worthy of lamentation that when there is such a vast multitude of them, we have not yet conquered one?”

Plutarch, *Περί ευθυμίας*